

BremHLR

Kompetenzzentrum für Höchstleistungsrechnen Bremen

Statusbericht 2019
des
Kompetenzzentrums
für
Höchstleistungsrechnen Bremen
–BremHLR–

Bremen, Juli 2020



Universität Bremen



JACOBS
UNIVERSITY



ALFRED-WEGENER-INSTITUT
HELMHOLTZ-ZENTRUM FÜR POLAR-
UND MEERESFORSCHUNG



Norddeutscher Verbund für Hoch- und Höchstleistungsrechnen

© 2003-2020 BremHLR – Kompetenzzentrum für Höchstleistungsrechnen Bremen

www.bremhllr.uni-bremen.de

Das Berichtsjahr 2019 in Stichpunkten

- Stabile Bremer Nutzung der Ressourcen des Norddeutschen Verbunds für Hoch- und Höchstleistungsrechnen (HLRN)
- Ende des HLRN-III Betriebs am Zuse-Institut Berlin
- Inbetriebnahme der zweiten Ausbaustufe des neuen Rechnersystems HLRN-IV in Berlin

Inhaltsverzeichnis

| | | |
|------|---|----|
| 1 | BremHLR: Aufgaben und organisatorische Struktur | 5 |
| 1.1 | Aufgaben..... | 5 |
| 1.2 | Struktur..... | 5 |
| 2 | Tätigkeitsprofil des BremHLR im Berichtszeitraum | 6 |
| 2.1 | Unterstützung der HLRN-Nutzung im Land Bremen | 6 |
| 3 | Statistische Angaben zu den Bremer Höchstleistungsprojekten..... | 6 |
| 4 | Veranstaltungen mit Beteiligung des BremHLR..... | 7 |
| 5 | Informationen zur Infrastruktur: Ausbau des HLRN-IV Systems zum Ende des Jahres 2019..... | 10 |
| 6 | Projektberichte | 11 |
| 6.1 | <i>hbc00027</i> : High-level calculations on defects and surfaces of semiconductors..... | 11 |
| 6.2 | <i>hbc00029</i> : Understanding the catalytic performance of rare-earth oxides: Toward a knowledge-driven design of catalysts from first-principles calculations..... | 15 |
| 6.3 | <i>hbc00030</i> : Dynamics of fluoride anions in all-silica and silico-germanate zeolites | 19 |
| 6.4 | <i>hbc00034</i> : Aminoacids-Functionalized Platinum Nanoparticles as Asymmetric Heterogeneous Catalysts | 24 |
| 6.5 | <i>hbc00039</i> : New insights into the crystal-chemistry, mechanical properties and thermal expansion of Kentrolite and Melanotektite | 28 |
| 6.6 | <i>hbi00033</i> : Flow transitions and regimes in core-annular pipe flow..... | 32 |
| 6.7 | <i>hbi00036</i> : Fluid Dynamics Investigation of the Effect of Stresses Exerted in the Premix Emulsification Process of o/w Protein Stabilised Emulsions..... | 35 |
| 6.8 | <i>hbi00037</i> : Molekulardynamische Untersuchung der Stressbeanspruchungen auf Proteine an der Phasengrenzfläche beim Premix-Membranemulgieren | 37 |
| 6.9 | <i>hbi00038</i> : Direct Numerical Simulation and Modeling of Turbulent Convection in Porous Media | 39 |
| 6.10 | <i>hbi00041</i> : Large-scale energy flux in turbulent pipe flow | 43 |
| 6.11 | <i>hbk00032</i> : Climate change and atmosphere / ocean interaction in the coupled FESOM/ECHAM model..... | 46 |
| 6.12 | <i>hbk00034</i> : Ice sheet - ice shelf - ocean interaction in the marginal seas of the Southern Ocean | 49 |
| 6.13 | <i>hbk00038</i> : Interaction between marine terminating glaciers and the ocean circulation in Northeast Greenland | 52 |
| 6.14 | <i>hbk00055</i> : Investigating the biogeochemistry of the high latitudes during the period of rapid change: modelling and satellite retrievals | 56 |

| | | |
|------|---|-----|
| 6.15 | <i>hbk00057</i> : Persistent ozone depletion in the tropical stratosphere: identifying possible reasons | 59 |
| 6.16 | <i>hbk00059</i> : Joint state-parameter estimation for the Last Glacial Maximum with CESM1.2.63 | |
| 6.17 | <i>hbk00061</i> : Combining ocean models and proxy data | 67 |
| 6.18 | <i>hbk00062</i> : Retrieval of stratospheric ozone profiles from OMPS observations in limb geometry and long term trends | 71 |
| 6.19 | <i>hbk00064</i> : Coupled ensemble data assimilation for Earth system models..... | 75 |
| 6.20 | <i>hbk00071</i> : Development of an Earth system model coupled with a sediment diagenesis model toward long-term paleoclimate simulations | 79 |
| 6.21 | <i>hbk00072</i> : Interannual variability of air-sea CO ₂ exchange: high-resolution ocean biogeochemical simulations | 83 |
| 6.22 | <i>hbk00076</i> : Simulation der letzten glazialen Termination mit einem gekoppelten Klima-Eisschild-Modell..... | 87 |
| 6.23 | <i>hbp00029</i> : Carrier dynamics and optical properties of transition metal dichalcogenides.... | 90 |
| 6.24 | <i>hbp0041</i> : Multi-messenger Signals from Compact Objects | 95 |
| 6.25 | <i>hbp00045</i> : Non-local manipulation of correlation effects in 2D Transition Metal Dichalcogenides..... | 99 |
| 6.26 | <i>hbp00046</i> : Modelling strongly correlated electrons in presence of nonlocal interactions. | 103 |
| 6.27 | <i>hbp00047</i> : Coulomb engineering of Mott insulators | 106 |
| 6.28 | <i>nak00001</i> : Seamless sea ice prediction with AWI Climate Model | 109 |

1 BremHLR: Aufgaben und organisatorische Struktur

1.1 Aufgaben

Das Land Bremen beteiligt sich am Norddeutschen Verbund für Hoch- und Höchstleistungsrechnen – HLRN – um an dem rasanten Fortschritt der Computer- und Softwaretechnologie Teil zu haben. Das Kompetenzzentrum für Höchstleistungsrechnen Bremen – BremHLR – unterstützt dazu Wissenschaftler im wissenschaftlichen Rechnen insbesondere im Land Bremen. Die Fachberater des BremHLR leisten Unterstützung für Projekte sowohl in der Konzeption, der Antragstellung als auch der Durchführung. Der Schwerpunkt der Unterstützung liegt hierbei auf Projekten auf dem HLRN-System. Seit 2005 wurde die Betreuung aber auch auf Rechenprojekte an den nationalen Höchstleistungsrechenzentren wie z. B. dem Jülich Supercomputing Centre (JSC) ausgeweitet.

Als Bestandteil im Kompetenznetzwerk des HLRN beteiligt sich BremHLR unter anderem an der fachspezifischen Nutzerberatung, der Pflege von Software-Paketen und der Veranstaltung überregionaler Nutzerworkshops. Die Geschäftsstelle des BremHLR ist an der Universität Bremen im Zentrum für Technomathematik angesiedelt.

Das BremHLR wurde am 1. Juli 2003 als Kooperation zwischen der Universität Bremen (UB), der Jacobs University Bremen (JUB) und dem Alfred-Wegener-Institut Helmholtz-Zentrum für Polar- und Meeresforschung (AWI) gegründet. Seit April 2008 ist auch die Hochschule Bremerhaven (HBHV) Kooperationspartner des BremHLR. Das Kompetenzzentrum wird von den beteiligten Kooperationspartnern sowie der Bremer Senatorin für Wissenschaft und Häfen (SWH) anteilig finanziell getragen. Seit Januar 2014 ist die JUB als ideelles Mitglied beitragsfrei gestellt. Zum Jahr 2019 konnte eine Weiterfinanzierung des BremHLR bis Ende 2021 sicherstellt werden.

1.2 Struktur

Dem Lenkungsausschuss des BremHLR als oberstes beschlussfassendes und steuerndes Gremium gehörten in der Berichtsperiode folgende Vertreter der kooperierenden Einrichtungen an. Im Einzelnen sind dies:

- Prof. Dr. Alfred Schmidt (UB/Zentrum für Technomathematik ZeTeM)
- Prof. Dr. Stephan Frickenhaus (AWI/Rechenzentrum, UB/FB3)
- Prof. Dr. Ulrich Kleinekathöfer (JUB)
- Prof. Dr. Henrik Lipskoch (HBHV)
- Dr. Jörg Hofmann (SWH)

Die fachspezifische Betreuung der Projekte am Norddeutschen Verbund für Hoch- und Höchstleistungsrechnen (HLRN) sowie von Projekten an anderen nationalen Höchstleistungsrechenzentren wird von den Fachberatern des BremHLR geleistet, die ebenfalls den Einrichtungen der Kooperationspartner angehören. Im Berichtszeitraum waren folgende Fachberater tätig:

- Dr. Lars Nerger (AWI/Rechenzentrum, UB/ZeTeM, Leiter Geschäftsstelle)
- Thorsten Coordes (UB/ZARM)
- Dr. Achim Geleßus (JUB/CLAMV)
- Dr. Natalja Rakowsky (AWI/Rechenzentrum)

Die Geschäftsstelle ist verantwortlich für die Organisation der Workshops (siehe Abschnitt Veranstaltungen) und die Unterstützung der Nutzer, insbesondere im Antragsverfahren. Das Sekretariat der Geschäftsstelle wird betreut von

- Julitta von Deetzen.

2 Tätigkeitsprofil des BremHLR im Berichtszeitraum

2.1 Unterstützung der HLRN-Nutzung im Land Bremen

Ein Schwerpunkt der Aktivitäten des BremHLR lag auch in diesem Berichtszeitraum in der Unterstützung der HLRN-Nutzung. Neben den Tätigkeiten von Prof. Dr. Stephan Frickenhaus als Mitglied der Technischen Kommission sowie Prof. Dr. Alfred Schmidt als Mitglied des Wissenschaftlichen Ausschusses bestand die Unterstützung des HLRN durch das BremHLR hauptsächlich in der Fachberatung für Bremer Projekte am HLRN von der Antragstellung bis zur Begleitung rechenintensiver Projekte während der gesamten Projektlaufzeit.

Eine wesentliche Aufgabe im Berichtsjahr war die weitere Unterstützung der Bremer Nutzer des HLRN bei der effizienten Nutzung des HLRN Hochleistungsrechnersystems. Des Weiteren haben die Fachberater des BremHLR Nutzer bei der Portierung ihrer Modelle auf das neue Rechnersystem HLRN-IV unterstützt. Am 19.12.2019 wurde die zweite Ausbaustufe des HLRN-IV in Berlin für Fachberater und erfahrene „Powernutzer“ geöffnet, um Anwendungen zu portieren und das System zu testen. Die Portierungsunterstützung wird auch im Jahr 2020 ein wichtiges Aufgabengebiet sein, da die Öffnung des Berliner HLRN-IV Systems für alle Nutzer erst im Jahr 2020 erfolgt.

3 Statistische Angaben zu den Bremer Höchstleistungsprojekten

Auch im Jahr 2019 wurde der HLRN intensiv durch Bremer Projekte genutzt. Im Zeitraum vom Januar bis September wurde auf den HLRN Systemen ein prozentualer Anteil von 9,3 % an der gesamten am HLRN abgenommenen Rechenleistung erreicht. Dieses liegt deutlich über dem investiven Anteil von etwa 3,5% des Landes Bremen am HLRN. Über die gesamte Laufzeit seit Einrichtung des HLRN-Verbunds wurde durch Bremer Projekte ein Anteil von 8,5% der verfügbaren Rechenzeit abgenommen.

Am 16.10. wurde in Berlin das HLRN-III System entgeltig abgeschaltet. Wegen des Umbaus des Rechnersystems in Berlin war ab Oktober 2019 nur eine deutlich eingeschränkte Rechenkapazität verfügbar. Daher wurde im Jahr 2019 insgesamt nur etwa 4.600.000 NPL¹ durch Bremer Projekte am HLRN abgenommen, was ca. 60% der Abnahme im Jahr 2018 entspricht. Abbildung 3.1 zeigt den monatlichen Verbrauch der Bremer Projekte am HLRN-III System. Von September 2018 bis Mitte Januar 2019 gelten die Verbrauchszahlen nur für den Berliner HLRN-Komplex, der bis zur Installation der zweiten Ausbaustufe des HLRN-IV noch weiter betrieben wurde, wobei dieses System besonders stark genutzt wurde. Für das vierte Quartal 2019 liegt nur ein Gesamtwert für das gesamte Quartal vor, da eine detaillierte Abfrage der genutzten Rechenkapazität nicht möglich war.

¹Norddeutsche Parallelrechner-Leistungseinheit: Auf dem Berliner HLRN-III Systemen entspricht die Nutzung eines Knotens über eine Stunde 2,4 NPL. Auf dem Göttinger HLRN-IV System entspricht die Nutzung eines Knotens über eine Stunde 6 NPL.

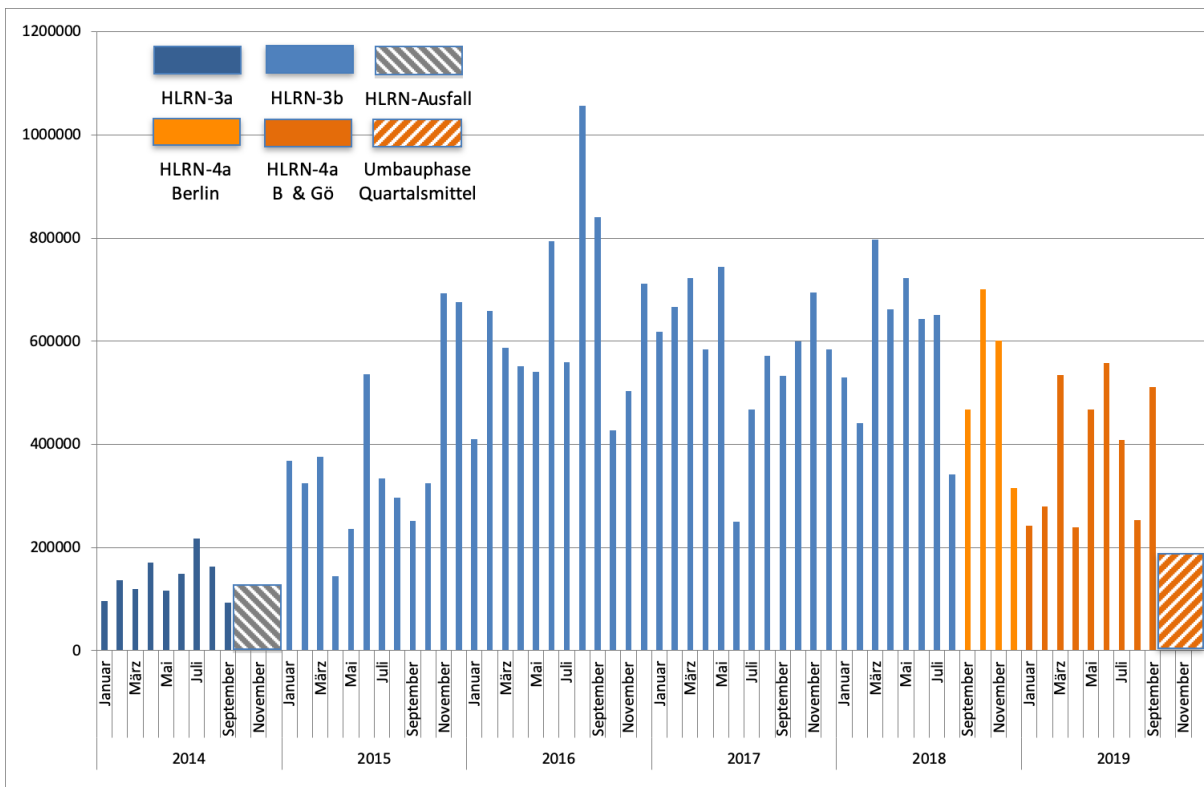


Abbildung 3.1: Monatliche Rechenzeitnutzung der Bremer HLRN-Großprojekte seit Januar 2014 auf den HLRN-III und HLRN-IV Systemen in der HLRN-Leistungseinheit NPL. Die Farben zeigen die Verfügbarkeit der unterschiedlichen Ausbaustufen des HLRN-Systems. Von Oktober bis Dezember 2014 waren die HLRN-Systeme nicht bzw. nur teilweise nutzbar. Im vierten Quartal 2019 wurden die NPL wegen der Umstellung auf HLRN-IV für das gesamte Quartal, statt monatlich erfasst. In dieser Zeit war weitgehend nur das HLRN-IV System in Göttingen verfügbar.

Eine Übersicht zu allen vom BremHLR betreuten Projekten gibt Tabelle 3.1. Im Jahr 2019 wurden vom BremHLR 39 Projekte am HLRN betreut. Die Projekte werden von über 100 akkreditierten Nutzern durchgeführt. 15 neue Projekte mit teilweise sehr großem Rechenzeitbedarf wurden im Jahr 2019 beantragt und vom Wissenschaftlichen Ausschuss des HLRN bewilligt. 8 Projekte wurden im Berichtsjahr beendet.

4 Veranstaltungen mit Beteiligung des BremHLR

35. HLRN-Fachberater-Workshop

Veranstalter: BremHLR

Datum: 1. – 2. April 2019

Ort: ZARM, Uni Bremen

Teilnehmerzahl: 23

Teilnehmende Institutionen: Atos, BremHLR (AWI, ZARM), GWDG/Uni Göttingen, IOW, TU Braunschweig, Uni Hamburg (RRZ, Sternwarte), Uni Kiel, Uni Oldenburg, Uni Rostock, ZIB, Landesvertreter Bremen (Verwaltungsrat, Wissenschaftlicher Ausschuss, Technische Kommission)

36. HLRN-Fachberater-Workshop

Veranstalter: ZIB

Datum: 24. – 25. Oktober 2019

Ort: ZIB

Teilnehmerzahl: 26

Teilnehmende Institutionen: Atos, BremHLR (AWI, ZARM), GWDG/Uni Göttingen, TU Braunschweig, TU Hamburg, Uni Hamburg, Uni Kiel, Uni Oldenburg, Uni Rostock, ZIB, Landesvertreterin Berlin im Verwaltungsrat

Tabelle 3.1: Übersicht der Bremer HPC-Projekte, die innerhalb des Berichtszeitraums vom BremHLR betreut wurden. Status: F = Fortsetzung, E = Erstantrag; kNPL: Kontingent in tausend NPL im Jahr 2019

| Kennung | Projektleiter | Institut | Laufzeit | kNPL | Status |
|----------------|--|-----------------|-----------------|-------------|---------------|
| hbc00027 | Prof. Dr. P. Deak | UB/BCCMS | I/18 – I/20 | 105 | F |
| hbc00028 | Dr. M. DellePiane | UB/BCCMS | I/18 – I/19 | 20 | E |
| hbc00029 | Dr. L. Moskaleva | UB/Chemie | I/18 – IV/20 | 200 | F |
| hbc00030 | Dr. M. Fischer | UB/Geo | II/18 – II/20 | 163 | F |
| hbc00031 | Prof. Dr. L. Mädler | UB/FB4 | III/18 – II/19 | 6 | E |
| hbc00034 | Dr. M. DellePiane | UB/BCCMS | I/19 – I/20 | 160 | E |
| hbc00039 | Dr. M. Mushed | UB/Chemie | II/19 – I/20 | 43 | E |
| hbi00026 | Dr.-Ing. R. Groll | UB/ZARM | II/15 – II/19 | 30 | F |
| hbi00033 | Prof. Dr. M. Avila | UB/ZARM | I/17 – I/20 | 196 | F |
| hbi00036 | Prof. Dr. U. Fritsching | UB/FB4 | II/17 – I/20 | 108 | F |
| hbi00037 | Prof. Dr. U. Fritsching | UB/FB4 | II/17 – I/20 | 154 | F |
| hbi00038 | Dr. Y. Jin | UB/ZARM | I/19 – I/20 | 120 | E |
| hbi00041 | Dr. D. Feldmann | UB/ZARM | III/19 – II/20 | 123 | E |
| hbi00042 | Prof. Dr. A. Baars | HS Bremen | IV/19 – III/20 | 50 | E |
| hbk00032 | Prof. Dr. T. Jung | AWI & UB | II/12 – II/20 | 649 | F |
| hbk00034 | Prof. Dr. T. Kanzow | AWI & UB | III/13 – III/20 | 850 | F |
| hbk00038 | Prof. Dr. T. Kanzow | AWI & UB | III/14 – II/20 | 300 | F |
| hbk00055 | Prof. Dr. A. Bracher | AWI & UB | III/16 – I/20 | 90 | F |
| hbk00057 | Dr. A. Rozanov | UB/IUP | I/17 – II/20 | 216 | F |
| hbk00059 | Prof. Dr. M. Schulz | UB/MARUM | III/17 – III/20 | 185 | F |
| hbk00061 | Prof. Dr. M. Schulz | UB/MARUM | IV/17 – II/19 | 80 | F |
| hbk00062 | Dr. A. Rozanov | UB/IUP | IV/17 – III/20 | 270 | F |
| hbk00064 | Prof. Dr. T. Jung | AWI & UB | I/18 – III/20 | 330 | F |
| hbk00067 | Prof. Dr. M. Schulz | UB/MARUM | I/18 – I/19 | 76 | E |
| hbk00070 | Prof. Dr. M. Schulz | UB/MARUM | III/18 – II/19 | 100 | E |
| hbk00071 | Prof. Dr. M. Schulz | UB/MARUM | I/19 – IV/20 | 100 | E |
| hbk00072 | Prof. Dr. D. Wolf-Gladrow | AWI & UB | I/19 – IV/20 | 632 | E |
| hbk00075 | Prof. Dr. D. Wolf-Gladrow | AWI & UB | IV/19 – III/20 | 50 | E |
| hbk00076 | Prof. Dr. M. Schulz | UB/MARUM | II/19 – I/20 | 100 | E |
| hbk00077 | Dr. K. Purkiani | UB/MARUM | II/19 – I/20 | 85 | E |
| hbp00029 | Dr. M. Lorke | UB/Physik | IV/15 – II/20 | 116 | F |
| hbp00041 | Prof. Dr. C. Lämmerzahl, Prof. Dr. S. Rosswog | UB/ZARM | I/17 – I/20 | 115 | F |
| hbp00045 | Prof. Dr. T. Wehling | UB/Physik | II/17 – II/19 | 98 | F |
| hbp00046 | Prof. Dr. T. Wehling | UB/Physik | IV/17 – IV/19 | 101 | F |
| hbp00047 | Prof. Dr. T. Wehling | UB/Physik | I/19 – IV/20 | 92 | E |
| hbp00048 | Dr. M. Lorke | UB/Physik | IV/19 – III/20 | 37 | E |
| hbp00049 | Prof. Dr. T. Wehling | UB/Physik | IV/19 – III/20 | 35 | E |
| hbp00050 | Prof. Dr. T. Wehling | UB/Physik | IV/19 – III/20 | 22 | E |
| nak00001 | Dr. H. Gößling | AWI | II/19 – I/20 | 274 | E |

5 Informationen zur Infrastruktur: Ausbau des HLRN-IV Systems zum Ende des Jahres 2019

Im September 2018 wurde an der Universität Göttingen die erste Ausbaustufe des neuen HLRN-IV Rechnersystems in Betrieb genommen. Der Standort in Göttingen hat den bisherigen Betreiberstandort an der Universität Hannover abgelöst. Am 11. Dezember 2019 ist das Göttinger System für alle Nutzer geöffnet wurden.

Die zweite Ausbaustufe des HLRN-IV wurde zunächst am ZIB in Berlin installiert. Während der ersten Ausbaustufe des HLRN-IV wurde das bisherige HLRN-III System am ZIB noch bis zum 16. Oktober 2019 weiter betrieben. Zu diesem Termin musste es dann abgeschaltet werden um das neue HLRN-IV System in Betrieb nehmen zu können. Wegen der notwendigen Abschaltung des HLRN-III Systems stand während des Umbaus im 4. Quartal 2019 nur das HLRN-IV System in Göttingen zur Verfügung. Am 19. Dezember 2019 wurde dann das neue HLRN-IV System in Berlin für Fachberater und Poweruser geöffnet.

Die HLRN-IV Systeme wurden von der Firma Atos geliefert. Die Systeme sind wie folgt konfiguriert:

Göttingen:

- 432 Dual-Socket Knoten mit einer standard Speicherausstattung von 192 GB
- 16 Dual-Socket Knoten mit einer großen Speicherausstattung von 768 GB
- Jeder Knoten ist ausgestattet mit
 - 2 Intel XEON Skylake Gold (6148) mit 2,4 GHz Taktung und jeweils 20 Prozessorkernen
 - 480 GB Solid-State Disk
- Netzwerk: Intel Omni-Path
- 8,1 PB paralleles Lustre Dateisystem ("WORK" zur Speicherung von Simulationsdaten) über Omni-Path Netzwerk
- 340 TB Heimat-Dateisystem

Berlin:

- 1112 Dual-Socket Knoten mit einer standard Speicherausstattung von 384 GB
- 32 Dual-Socket Knoten mit einer großen Speicherausstattung von 768 GB
- 2 Dual-Socket Knoten mit einer sehr großen Speicherausstattung von 1.5 TB
- Jeder Knoten ist ausgestattet mit
 - 2 Intel Cascade Lake Platinum (9242) mit jeweils 46 Prozessorkernen
 - 1 Intel Omni-Path Netzwerkadapter
- Netzwerk: Intel Omni-Path mit 14 TB/s Bisektions-Bandbreite
- 8,1 PB paralleles Lustre Dateisystem ("WORK" zur Speicherung von Simulationsdaten) über Omni-Path Netzwerk
- 340 TB Heimat-Dateisystem

Das Göttinger System wurde nach Emmy Nöther „Emmy“ benannt und das Berliner System nach Lise Meitner „Lise“. Das Berliner System wurde im November auf der Top500 Liste der weltweit schnellsten Supercomputer auf Platz 40 eingestuft. In Deutschland steht „Lise“ auf Platz fünf.

6 Projektberichte²

6.1 *hbc00027*: High-level calculations on defects and surfaces of semiconductors

| | |
|--------------------|-------------------------------------|
| HLRNProject ID: | hbc00027 |
| Run time: | I/2019 – I/2020 |
| Project Leader: | Prof. Dr. Peter Deák |
| ProjectScientists: | Dr. Bálint Aradi, Dr. Michael Lorke |
| Affiliation: | University Bremen, BCCMS |

Overview

The functionality of semiconductors is closely connected to their defects, which control the electronic and optical behavior of the bulk material and the chemical behavior of the surface. While the standard local (LDA) and semi-local (GGA) approximations of density functional theory (DFT) have played an important role in understanding the properties of defects in traditional semiconductors, they often fail completely in wide band gap materials. In recent years, screened hybrid exchange functionals (mixing non-local and semi-local exchange), like HSE, have emerged as a possible replacement. The present project deals with the application and possible extension of HSE-type functionals for defects and surfaces of wide band gap semiconductors.

We have found earlier that semi-empirical, material-specific tuning of the two parameters of HSE (i.e., the fraction of non-local exchange, α , and the inverse screening length, μ) can lead to a good approximation of the exact functional, and allows the calculation of defect levels in the gap with an accuracy of ~ 0.1 eV. While the optimized parameters work well for all defects within the given host, the transferability of the parameters to other materials is very limited. Therefore, in the past project year, we have developed a new exchange functional with only one tunable parameter, which is transferable upon substitution of the cation or anion. In other words, this functional is applicable for the accurate calculation of defects in semiconductor alloys, which have great importance for photovoltaics.

Since the interest in layered semiconductors has increased in recent years enormously, our other goal was to test the performance of optimized HSE functionals for defects of the bulk compound and for monolayers, choosing GaSe and hexagonal BN (hBN) as examples. The former is mostly used in non-linear optics and for generation and detection of electromagnetic waves, but in monolayer form it can also exhibit exotic properties like giant piezoelectricity or tunable magnetism. The latter is often applied in layered heterostructures as a dielectric to encapsulate transition metal dichalcogenides or graphene. Additionally, in recent years, ultraviolet (UV) lasers, as well as ultra-bright single-photon emitters have been realized, highlighting the possibility to use hBN in quantum information technology and nano-photonics.

² Für den Inhalt der Projektberichte sind ausschließlich die genannten Projektleiter bzw. die Projektbearbeiter verantwortlich.

Results

In order to mimic the exact density functional, the total energy must show a piecewise linear behaviour as a function of the occupation numbers. This translates to the simultaneous reproduction of the quasiparticle gap (E_g) and the fulfilment of the generalized Koopman's theorem (gKT), i.e., the equality of the Kohn-Sham one-electron energy of the defect level with the ionization energy [1]. Table I shows the optimal values of the only parameter (Z) in our new functional for 14 semiconductors, with E_g between 0.4 eV and 14.2 eV. The remarkable point is that in related compounds, e.g. GaAs, InAs, GaN, or CuGaS₂, CuInS₂, or ZnSe, ZnS, CdS, or Si, SiC and diamond, the Z parameter does not change. In other words, the same functional can be applied after substitution of either the cation or the anion and, therefore, the method can be applied for alloys of any composition ratio. At the same time, this functional also satisfies the gKT, as shown in Table II for a few example cases. It was shown earlier that the restoration of the proper piecewise linearity of the total energy, as a function of the occupation numbers, ensures that the calculated energy data (charge transition levels, photoluminescence band) and localization of defect states (EPR parameters) are highly accurate, allowing reliable identification of defects. Therefore, we expect the new functional to perform well in semiconductor alloys. We have implemented and tested it in the generally used electronic structure package VASP. A preliminary description of our method has been uploaded to arXiv [2], and our paper about it is under submission.

Table I. Fundamental 0K single-particle gap of various semiconductors in comparison to the high level first-principle many-body theory (GW_0) in eV.

| | Z | Calc. E_g | reference | Semiconductor | $\Delta\text{KS(HOMO)} - \Delta\text{SCF}$ | $\Delta\text{SCF} - \Delta\text{KS(LUMO)}$ |
|--------------------------------|------|-------------|-----------|--------------------------------|--|--|
| | | | | GaAs | 0.02 | 0.03 |
| Ga ₂ O ₃ | 0.72 | 5.1 | 5.0 | GaN | -0.04 | -0.04 |
| GaAs | 0.72 | 1.6 | 1.6 | Ga ₂ O ₃ | -0.03 | -0.04 |
| GaN | 0.72 | 3.6 | 3.6 | Diamond | -0.05 | 0.05 |
| InAs | 0.72 | 0.4 | 0.4 | | | |
| CuGaS ₂ | 0.65 | 2.6 | 2.6 | | | |
| CuInS ₂ | 0.65 | 1.5 | 1.5 | | | |
| ZnSe | 0.62 | 2.8 | 2.7 | | | |
| ZnS | 0.62 | 3.8 | 3.7 | | | |
| CdS | 0.62 | 2.4 | 2.4 | | | |
| LiF | 0.62 | 14.2 | 14.2 | | | |
| Si | 0.53 | 1.1 | 1.3 | | | |
| SiC (3C) | 0.53 | 2.7 | 2.7 | | | |
| Diamond | 0.53 | 5.8 | 5.8 | | | |
| SiO ₂ | 0.53 | 10.1 | 10.2 | | | |

Table II. Fulfillment of the gKT with the new functional. $\Delta\text{KS(HOMO)}$ and $\Delta\text{KS(LUMO)}$ give the Kohn-Sham energy of the of the highest occupied level for the neutral, and of the lowest unoccupied one for the +1 charge state of the vacancy, respectively. ΔSCF is the self-consistent ionization energy (all in eV). The gKT is satisfied if the difference $\Delta\text{KS} - \Delta\text{SCF}$ is zero.

The success of the new functional has its origin in the improved description of electronic screening in the calculation of the exchange interaction. In traditional bulk semiconductors the screening is homogeneous, but this is not necessarily the case in layered materials, where the individual layers are held together by Van-der-Waals forces. We have found, however, that the electron distribution in GaSe and hBN are sufficiently homogeneous to use an effective screening constant. This has allowed us to optimize HSE parameters (for the reproduction of the gap and fulfilment of the gKT) in both systems [3]. The homogeneity definitely disappears in the case of single monolayers though, due to the jump in the dielectric constant at the interface with vacuum. In case of the relatively thick GaSe monolayer ($\sim 5\text{\AA}$), retuning the

parameters is possible, but not in the atomically thin hBN monolayer. While in the latter no accurate defect calculations are possible, using different parameter sets in bulk and monolayer GaSe, we have been able to interpret the experimentally observed difference in the electrical activity caused by intrinsic defects in the bulk and in the monolayer (see Fig.1) [4].

Outlook

The presence of an interface (e.g., with vacuum) influences the screening also inside the layer. This has a serious effect on the accuracy of defect calculations on semiconductor surfaces as well, since such surfaces are usually simulated by a layer (slab) of finite thickness. We have shown that in semiconductors with low electronic dielectric constant (e.g., oxides) the accuracy of defect results with same functional is always different for defects in the bulk (middle of a thick slab) from that on the surface [3]. Improvement can only be expected if the inhomogeneity of the screening across the interface is taken into account. Our next project aims at developing such a functional and applying it to semiconducting monolayers and their heterostructures, as well as to investigate the effect of substrate defects on the properties of monolayers deposited onto the surface.

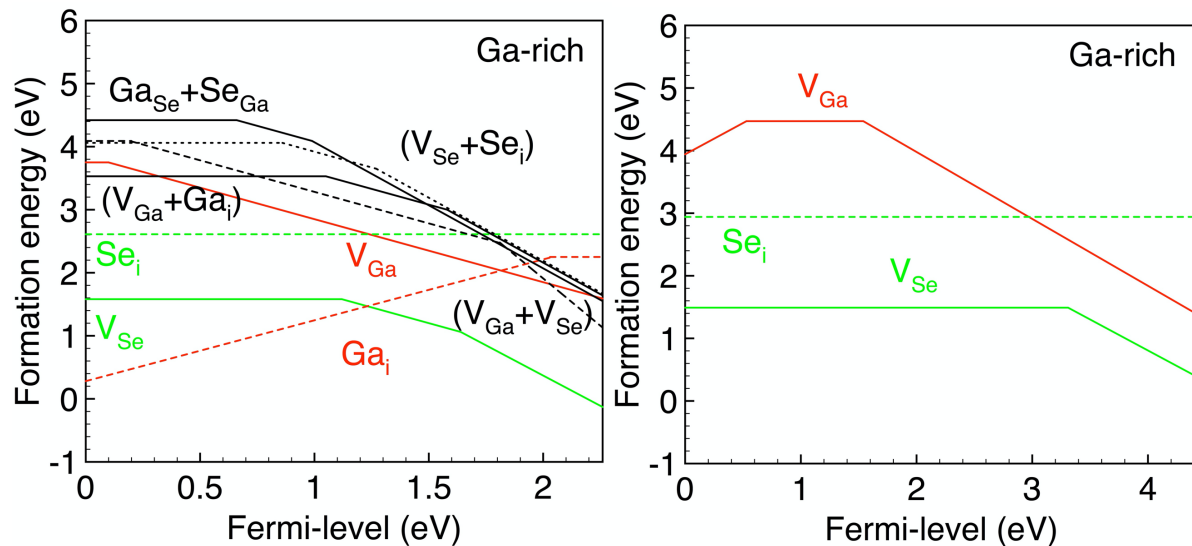


Figure 1: Formation energies of the most important intrinsic defects in bulk and monolayer GaSe, under Ga-rich growth conditions, as the function of the Fermi-level position w.r. to the valence band edge. The break points of the curves indicate the change in the charge state of the defect. As can be seen, these points occur at very different Fermi-level positions. Also, the absence of interlayer Ga interstitials means that while bulk GaSe is a self-compensating semi-insulating material, the bulk is intrinsically *p*-type.

Finally we note that the limited access and long turn-around times during the switch from System III to IV, which lasted almost half a year, has put serious constraint on our research. Despite of the help by the HLRN support staff, we have not been able to achieve all our goals in time. Since the reconstruction is still ongoing, the meticulous planning, required by the scientific committee in new project applications, will be quite difficult.

Publications

1. P. Deák, M. Lorke, B. Aradi, and T. Frauenheim, *Optimized hybrid functionals for defect calculations in semiconductors*, J. Appl. Phys. **126**, 130901 (2019). **Invited “Perspectives” article.**
2. M. Lorke, P. Deák, and T. Frauenheim, *Asymptotically correct screened exchange potential for semiconductors: A Koopman’s compliant approach*, arXiv:1907.0840v2 [cond-mat-mtrl-sci] 2019, <https://arxiv.org/abs/1907.08404>.
3. P. Deák, E. Khorasani, M. Lorke, M. Farzalipour-Tabriz, B. Aradi, and T. Frauenheim,

Defect calculations with hybrid functionals in layered compounds and in slab models, Phys. Rev. B **100**, 235304 (2019).

4. P. Deák, M. M. Han, M. Lorke, M. Farzalipour Tabriz, and Thomas Frauenheim, *Intrinsic defects of GaSe*, J. Phys. Condens. Mater. *accepted*

Presentations

1. P. Deák: *Optimized hybrid functionals for defect calculations*, 1st Sino-German Symposium on “Defect Engineering in SiC Device Manufacturing”, **invited talk**, Nov. 10-14, 2019, Beijing

6.2 *hbc00029*: Understanding the catalytic performance of rare-earth oxides: Toward a knowledge-driven design of catalysts from first-principles calculations

| | |
|--------------------|--|
| HLRNProject ID: | hbc00029 |
| Run time: | I/2019 – IV/2019 |
| Project Leader: | Dr. Lyudmila Moskaleva |
| ProjectScientists: | Shikun Li; Yong Li |
| Affiliation: | Universität Bremen, Institut für Angewandte und Physikalische Chemie, Leobener Str. UFT, 28359, Bremen |

Overview

Rare earth oxides are attracting increasing interest as a relatively unexplored group of materials with potential applications in heterogeneous catalysis and electrocatalysis; therefore, a credible and universal computational approach is needed for modeling their reactivity. In this work, we evaluated the performance of PBE+U in describing electronic structure and adsorption properties of the CeO₂(111) and Nd₂O₃(0001) surfaces. The HSE06 method reproduces rather well the lattice parameters and selected energetic properties with respect to the experimental values. PBE+U method is performing satisfactorily only if the U parameter is selected from appropriate range of values.

Results

Degree of electron localization of CeO₂(111) and Nd₂O₃(0001) surfaces under PBE+U and HSE calculations

On a defect-free CeO₂(111) surface, the average net ionic charge of the surface Ce ions at the PBE+U level increases with increasing parameter U from +2.29e (U=0 eV) to +2.47e (U=8 eV), reflecting higher degree of 4f electron localization at higher U. Our PBE+U results agree very well with the values found by Castleton et al.[1] for defect-free bulk CeO₂ at the LDA+U level. The hybrid functional HSE06 predicts the charge on Ce of +2.51e. The calculated net ionic charges are quite different from nominal +4e, suggesting that the Ce-O bonding is to some extent covalent.

Next we examined the charges on Ce ions for the the CeO₂(111) surface with O vacancies. The net ionic charge of Ce near the defect site, Fig. 1(A), light blue curve, was taken as the average value of the two surface Ce ions holding the excess electrons near oxygen vacancy. It decreases with increasing U consistent with stronger localization of Ce4f electrons on the Ce ions near the defect site. At the same time, the net ionic charge of Ce ions far from the defect, Fig. 1(A), yellow curve, is increasing with the parameter U. The difference between the net ionic charges of the Ce ions far from the O vacancy and near the O vacancy becomes larger with the increasing parameter U, which further indicates that 4f electrons become more localized for U values 4-7 eV, consistent with the results of Castleton et al.[1] It is worth noting that large U values (U=7-8 eV) are required to properly describe the localization of Ce4f electrons, whereas smaller U values (U=1-3 eV) are more suitable to reproduce properly the lattice parameters and reaction energies.

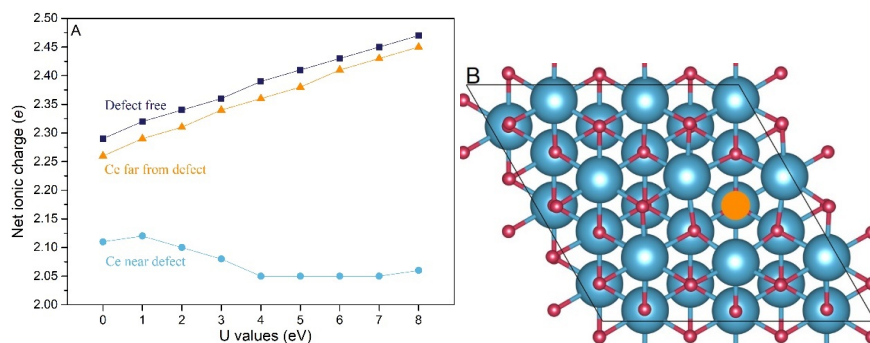


Figure 1: (A) Net Ce ionic charges on CeO₂(111) surface as a function of the parameter U, including Ce ions on the defect-free surface, Ce ions near the oxygen vacancy site, Ce ions far from the oxygen vacancy site. (B) Top view of CeO₂(111) surface with one surface oxygen vacancy highlighted in orange color. Ce atoms are shown in light green, O atoms in dark red.

Surface reactivity of CeO₂(111) and Nd₂O₃(0001) surfaces under PBE+U and HSE calculations

The workfunction (WF) slowly changes from 6.40 eV (U=1 eV) to 6.23 eV (U=8 eV), and is thus almost independent from the parameter U for the CeO₂(111) surface, differently from the Nd₂O₃(0001) and Ce₂O₃(0001) surfaces, for which the WF increases with U, see Fig. 2(D). This different behavior of the two cerium oxide surfaces is rather expected since the Ce4f states of the CeO₂(111) surface are mainly unoccupied and tetravalent Ce cannot be further oxidized, while Ce₂O₃(0001) surface whose Ce4f states are partially occupied could relatively easily release one electron, leading to the calculated WF, which depends on the parameter U, Fig. 2(A,C). The higher the U value, the higher the degree of 4f localization, hence resulting in a higher value of WF. Similarly, the dependence of the WF of the Nd₂O₃(0001) surface on the parameter U originates from the partially occupied and partially empty Nd4f bands, Fig. 2(B). The deviation of the PBE+U for work function from the HSE06 result is up to 1.2 eV for the CeO₂(111) surface, indicating that the description of the process of electron emission from the surface by PBE+U is not satisfactory. PBE+U could be tuned choosing appropriate U for the Nd₂O₃(0001) and Ce₂O₃(0001) surfaces. U values ranging within 5-8 eV resulted in the work function values close to the HSE06 result for the Nd₂O₃(0001) surface, while U=5 eV gave the best agreement with the results of the hybrid functional for the Ce₂O₃(0001) surface. This range of U is substantially higher than the optimal U range determined based on the structural parameters and the reaction energies.

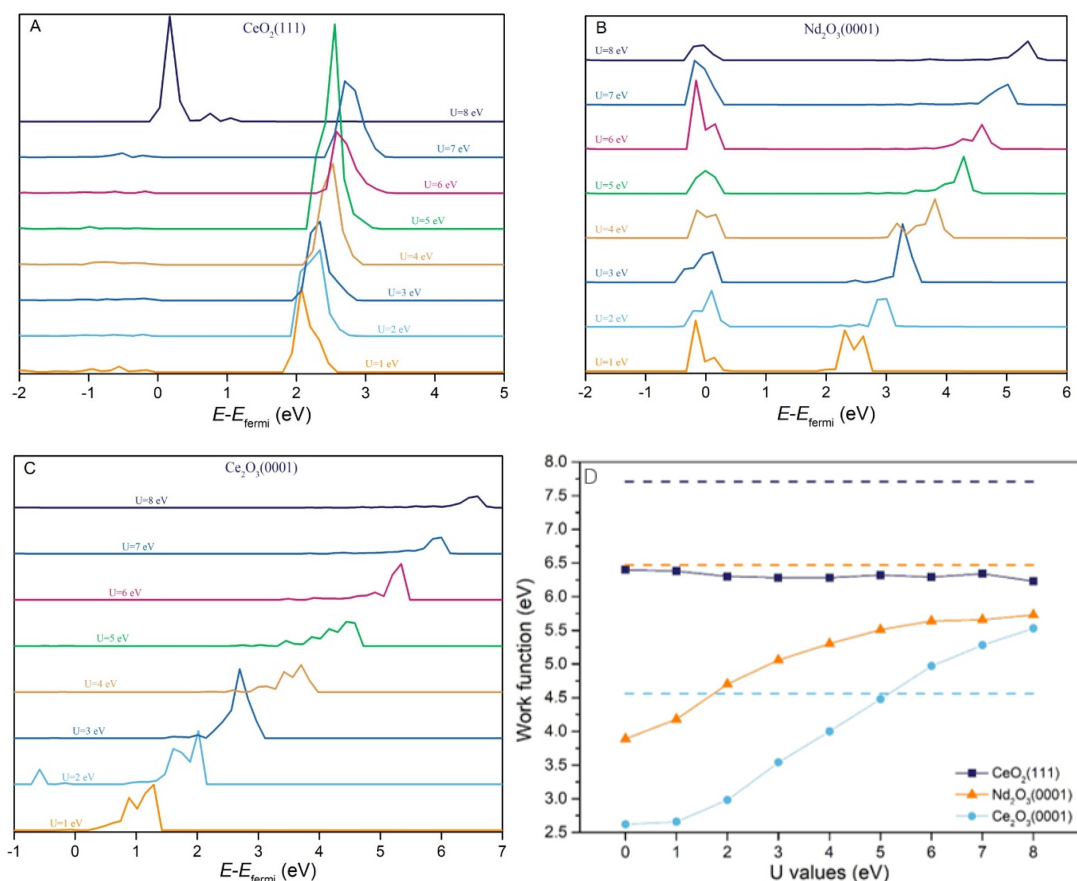


Figure 2: The partial density of states (pDOS) of Ce(4f) or Nd(4f) state of (A) CeO₂(111), (B) Nd₂O₃(0001) and (C) Ce₂O₃(0001) surfaces calculated by PBE+U under U = 1-8 eV. (D) Work function for the CeO₂(111) surface (dark blue, square), Nd₂O₃(0001) surface (orange, triangle) and Ce₂O₃(0001) surface (light blue, circle) as a function of the U parameter. The horizontal dotted lines separately represent the HSE06 results of the corresponding colors.

Adsorption properties of CeO₂(111) and Nd₂O₃(0001) surfaces under PBE+U and HSE calculations

The CH₃ radical and NH₃ molecule both adsorb on top of the surface cerium atoms owing to Lewis acidity of the CeO₂(111) surface. The PBE+U adsorption energies of both species are almost independent of U, which is similar to the work function. A similar observation was reported in ref. [2], where the adsorption energy of formaldehyde on CeO₂(111) was also found independent of the parameter U. Owing to the insufficient experimental data on the adsorption energy of CH₃ and NH₃ on ceria, we studied the adsorption of H₂O molecule to assess the performance of HSE06. The experimental desorption energy of H₂O is estimated to be ~0.9 eV at low coverage, while the calculated result by HSE06 is 0.3 or 0.49 eV depending on the adsorption geometry of water on the (2x2) CeO₂(111) surface without including the dispersion correction. [3]. Our calculations resulted in the adsorption energy of water up to -1.45 eV on the (3x3) CeO₂(111) surface with the HSE06 functional, while PBE functional predicted adsorption energy of -0.8 eV in a better agreement with experiment after considering the dispersion.

Different from the adsorption on the CeO₂(111) surface, there is a positive linear relationship between the CH₃ or NH₃ adsorption energy on the Nd₂O₃(0001) surface and the parameter U, Fig. 3. CH₃ adsorption turns out to be stronger than NH₃ adsorption on the Nd₂O₃(0001) surface by about 0.5 eV through the whole range of U values from 1 to 8 eV, while the adsorption

energies in both cases significantly depend on U and change from -1.25 to -0.6 eV and from -0.75 to 0 eV for CH_3 and NH_3 , respectively.

While we find that adsorption energies calculated by PBE(+ U) for the CH_3 or NH_3 adsorption on $\text{CeO}_2(111)$ deviate from the HSE06 values by up to 0.5 eV, it is possible that the hybrid functional shows systematic overbinding. This could be concluded from comparing the H_2O adsorption energy on the $\text{CeO}_2(111)$ surface to the experimental value. In that case, PBE functional performs better than the HSE06 hybrid functional, see above. Therefore, PBE functional could be reasonably applied in the surface adsorption energy calculations, but the inclusion of a Hubbard correction $U=3$ eV in combination with the PBE functional is suggested as a compromise solution to obtain a reasonable electron localization and adsorption energy of NH_3 and CH_3 .

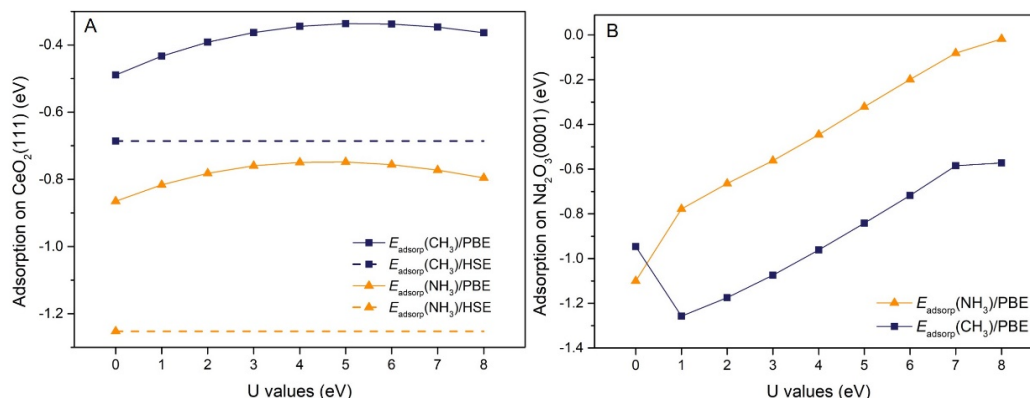


Figure 3: Adsorption energy of CH_3 (dark blue, square) and NH_3 (orange, triangle) on (A) $\text{CeO}_2(111)$ surface and (B) $\text{Nd}_2\text{O}_3(0001)$ surface as a function of U and the corresponding HSE06 results shown by the horizontal dotted lines.

Outlook

The relationship between the acidity-basicity property and oxidative coupling of methane (OCM) reactivity of REOs has been previously studied by experimental and theoretical methods. Early studies performed experimental characterizations to examine the acidity-basicity properties of REOs. At present, with the development of theoretical methods, the acidity-basicity of REOs can be systematically examined at the microscopic level. In the next phase of the project, we will select the $\text{La}_2\text{O}_3(0001)$ surface as a model surface to investigate the acidity-basicity property of an irreducible oxide surface. We doped this surface with several alkali, alkali-earth, transition metals and lanthanide atoms to study the influence of dopant on the acidity-basicity and surface adsorption properties.

Presentations

1. Shikun Li, Yong Li, Marcus Bäumer, Lyudmila Moskaleva. Theoretical study on the structures and thermodynamics of A-type rare earth sesquioxides by HSE and PBE+ U methods. BIG DATA SUMMER-A summer school of the BiGmax Network, Platja d'Aro, Spain, September 9 - 13, 2019, poster.

References

- [1] C. Castleton, J. Kullgren, K. Hermansson, J. Chem. Phys. 127(24) (2007) 244704.
- [2] M. Capdevila-Cortada, Z. Łodziana, N. López, ACS Catal. 6(12) (2016) 8370-8379.
- [3] D. Fernández-Torre, K. Kośmider, J. Carrasco, M.V. Ganduglia-Pirovano, R. Pérez, J. Phys. Chem. C 116(25) (2012) 13584-13593.

6.3 *hbc00030*: Dynamics of fluoride anions in all-silica and silico-germanate zeolites

| | |
|--------------------|--|
| HLRNProject ID: | hbc00030 |
| Run time: | II/2018 – II/2020 |
| Project Leader: | Dr. Michael Fischer |
| ProjectScientists: | Dr. Michael Fischer, Prof. Dr. Reinhard X. Fischer (<i>research group leader</i>), Linus Freymann (<i>student assistant</i>) |
| Affiliation: | Crystallography Group, Department of Geosciences, University of Bremen, Klagenfurter Straße 2-4, 28359 Bremen |

Overview

In this project, *ab-initio* molecular dynamics calculations are used to study the dynamic behaviour of fluoride anions confined to small cages in zeolite structures. One part of the calculations addressed the local environment and dynamics of fluoride anions in double four-ring cages in AST-typezeolites with different compositions. A second part dealt with the influence of the organic cation on the fluoride dynamics in MFI-type Silicalite-1. Ongoing work aims to compare the fluoride dynamics in a variety of zeolite frameworks.

Scientific background

Zeolites are a class of inorganic porous materials with important applications in ion exchange, gas and liquid separation, and catalysis.[1] Zeolite structures consist of a three-dimensional framework of tetrahedrally coordinated atoms connected by oxygen atoms. A rich variety of zeolite structures has been reported: To date, more than 240 distinct framework types have been recognised by the International Zeolite Association, who assigns three-letter framework type codes like “AST” or “MFI” to each framework. Prototypical zeolites, such as zeolite minerals, possess a negatively charged aluminosilicate framework whose charge is balanced by extra-framework cations. However, the development of sophisticated synthesis routes has led to the discovery of zeolite-like materials having a neutral framework, among them all-silica zeolites (composition SiO_2), germanates (GeO_2), silico-germanates ($\text{Si}_x\text{Ge}_{1-x}\text{O}_2$), aluminophosphates (AlPO_4), and gallophosphates (GaPO_4).

The synthesis in the presence of fluoride anions (“fluoride route”) is a particularly successful strategy to obtain neutral-framework zeotypes with very open frameworks and low defect concentrations. Various zeolites and zeotypes with unprecedented framework topologies can be synthesised via this route.[2,3] In the as-synthesised zeolites, the fluoride anions occupy well-defined positions in the crystal structure, balancing the charge of the cationic organic structure directing agents (OSDAs) that are used to promote the formation of a particular framework. Broadly, two different fluoride environments can be distinguished in this context: In zeolites having double four-ring (*d4r*) cages, the fluoride anions occupy the centre of this cage (**Fig. 1**). In structures without *d4r* units, fluoride anions also tend to occupy small cages. However, rather than being located at the cage centre, they are covalently bonded to a single silicon atom, forming trigonal-bipyramidal SiO_4F^- units. Frequently, the fluoride anions are disordered over two or more positions, as shown for several systems in **Fig. 1**.

In this project, the dynamics of fluoride anions confined to small cages in zeolite structures are studied using *ab-initio* molecular dynamics (AIMD) calculations, which cover a timescale of

several picoseconds. These investigations are carried out in the context of the project “*Beyond tetrahedral coordination in zeolite-type materials - A computational approach*” (project no. 389577027, Fi1800/5-1), funded by the Deutsche Forschungsgemeinschaft (DFG - German Research Foundation) since May 2018.

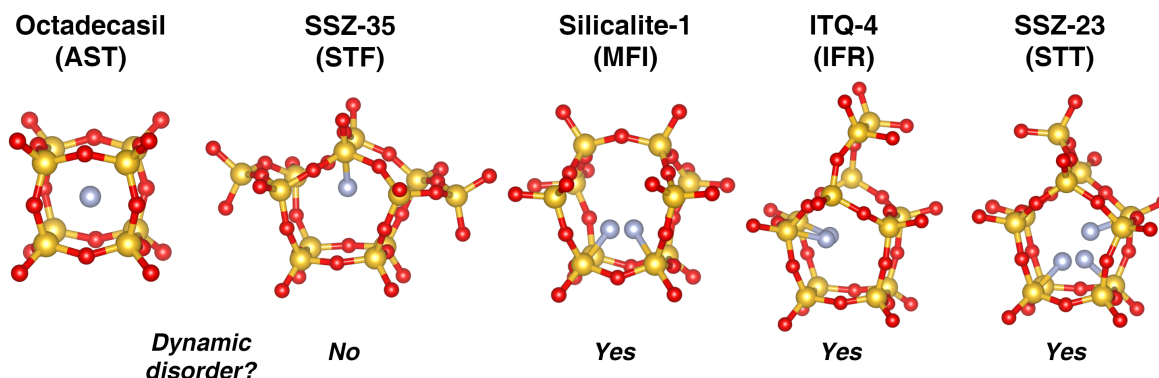


Figure 1: Fluoride environments in different zeolites studied in this project. For systems with SiO_4F^- units, the presence/absence of dynamic disorder of fluoride is indicated.

Results

1) AST-type systems: The AST framework is a prototypical zeolite with $d4r$ building units that is synthetically accessible across the range of germanosilicate compositions.[4] During the first period of this project, the local environment and dynamic behaviour of fluoride anions in AST-type silicogermanates was investigated using a combination of structure optimisations and AIMD calculations.[P1] Subsequent work covered a broader range of framework compositions, including AlPO_4 -AST (labelled AIPO-16 in the literature [5]) and the hypothetical GaPO_4 -AST. A particular focus of this study was a detailed analysis of the fluoride environment in average structures obtained from AIMD simulations at different temperatures (-123 °C, 25 °C, 300 °C). Representative results for 25 °C are shown in **Fig. 2**: It is clearly visible that the fluoride anions reside at the cage centre in SiO_2 - and GeO_2 -AST. This is also reflected in the Si-F/Ge-F radial distribution functions (RDFs), which show a single broad maximum centered at the Si-F/Ge-F equilibrium distances of 2.6/2.8 Å.

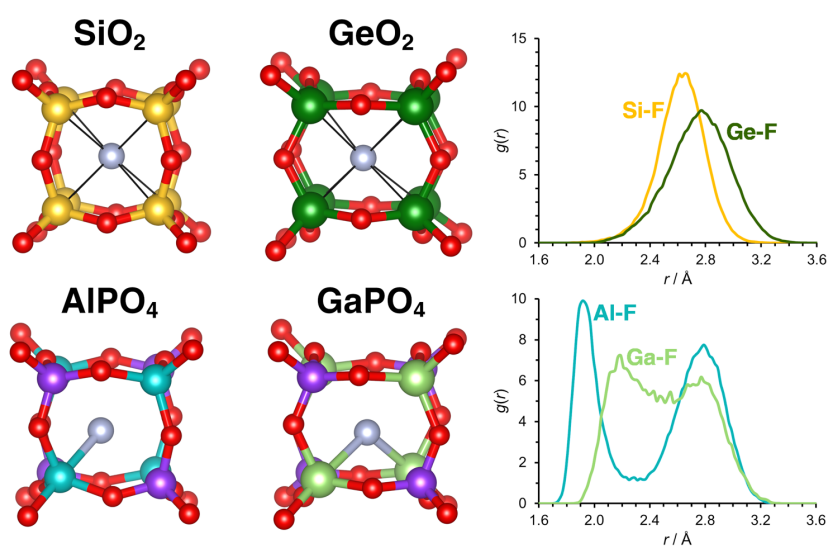


Figure 2: **Left:** Representative fluoride environments of AST-type systems from average structures extracted from the AIMD simulations ($T = 25\text{ °C}$). **Right:** Corresponding radial distribution functions for element pairs Si-F/Ge-F/Al-F/Ga-F.

Different observations are made in the AIMD average structures of AlPO_4 - and GaPO_4 -AST: Here, the fluoride anions are displaced from the cage center, typically forming a single Al-F bond in the aluminophosphate system, and locating at similar distance to two Ga atoms in the gallophosphate (**Fig. 2**). This behaviour is also reflected in the Al-F/Ga-F RDFs, which show two maxima corresponding to shorter and longer contacts to the Al/Ga atoms at the corners of the cage. The RDFs also indicate that there is a dynamic exchange between different fluoride positions on the picosecond timescale. This fast exchange could explain why the equilibrium fluoride position found in diffraction experiments is typically close to the cage center in aluminophosphate and gallophosphates with $d4r$ cages.[5,6]

2) Silicalite-1: MFI-type zeolites like ZSM-5 and Silicalite-1 are of considerable relevance for applications, primarily in catalysis (e.g., xylene isomerisation) and separation. For the case of as-synthesised Silicalite-1, it has been shown that the fluoride disorder is of a dynamic nature at room temperature, i.e., the anions move back and forth between adjacent positions on a timescale that is accessible with nuclear magnetic resonance (NMR) experiments. Upon cooling to cryogenic temperatures, characteristic changes in the NMR spectra show that the dynamic motion is frozen out.[7] Moreover, the extent of the dynamic disorder at room temperature depends on the OSDA: If tetrapropylammonium (TPA^+), the most typical OSDA in the synthesis of Silicalite-1, is replaced by methyltributylammonium (MTBA^+), the dynamic disorder at room temperature disappears.[8] Since NMR experiments can only give indirect insights into the local structure, DFT-based AIMD simulations were performed for Silicalite-1 models incorporating fluoride anions and different symmetric and asymmetric OSDAs (here, the term “symmetric” refers to OSDAs having four chains of equal length: tetramethyl/ethyl/propyl/butyl-ammonium). While calculations for room temperature delivered only a few dynamic “events” during which a fluoride anion moves from one Si atom to an neighbouring one, an increase of the simulation temperature to 100 °C resulted in a more substantial number of events. The left-hand side of **Fig. 3** reports the number of dynamic events observed in MFI-type systems containing different OSDAs. For systems with symmetric OSDAs, a certain decrease of the number of events with increasing length of the OSDA alkyl chains is visible, indicating a link between OSDA and fluoride dynamics.

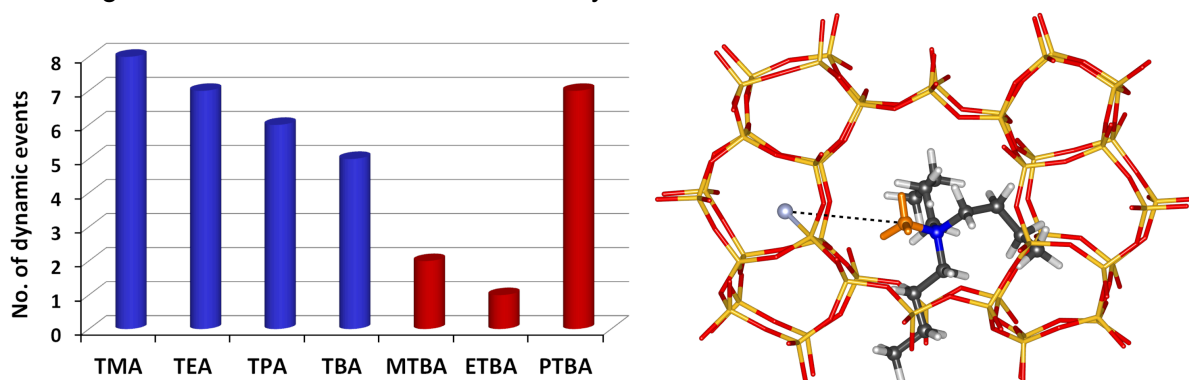


Figure 3: **Left:** Number of fluoride dynamic events occurring during a simulation time of 22.5 ps in Silicalite-1 models containing different OSDAs ($T = 100\text{ °C}$). Symmetric OSDAs: blue columns, asymmetric OSDAs: red columns. **Right:** Environment of the OSDA in MFI_(MTBA,F). The positively polarized methyl chain (orange) points towards the fluoride anion (light blue).

A much more prominent change occurs, however, for systems containing OSDAs having one short (methyl or ethyl) chain and three butyl chains (OSDA = MTBA, ETBA): Here, the number of dynamic events is drastically reduced, in qualitative agreement with the disappearance of dynamic disorder in MFI_(MTBA,F) observed experimentally.[8] In addition to reproducing experimental observations, the AIMD simulations also helped to rationalize the relationships between fluoride disorder and the molecular structure of the OSDA: In the asymmetric OSDAs

having a methyl or ethyl chain, the short chain is positively polarized. This short chain points towards the fluoride anion (**Fig. 3**), enhancing electrostatic interactions. The stronger interactions cause an increase of the energetic penalty for a displacement of the fluoride anion from its equilibrium position, thus suppressing dynamic disorder. The results of this study have recently been published in *The Journal of Physical Chemistry C*.**[P2]**

3) Other all-silica zeolites: In an ongoing part of the project, further AIMD simulations are employed to compare the fluoride dynamics of different all-silica zeolites. So far, the three systems ITQ-4 (IFR topology), SSZ-35 (STF), and SSZ-23 (STT) have been studied (**Fig. 1**). The calculations for 100 °C predict 4/3 dynamic events for ITQ-4/SSZ-23, but only a single event for SSZ-35. As for Silicalite-1, these results agree qualitatively with the experimentally observed differences in dynamic behavior.**[7]** The results are now being analysed in more detail in order to elucidate the structural origins for these differences.

Outlook

Another continuation of the project, starting in summer 2020, is envisaged. The calculations planned for this third phase of the project will address the following additional aspects:

- (1) Recent experimental work on MFI-type zeolites has shown that the replacement of an ammonium-based OSDA by a phosphonium-based compound leads to a decrease of fluoride dynamic disorder.**[9]** Further calculations will investigate the effect of phosphonium and arsonium cations on dynamic disorder.
- (2) Calculations for other all-silica zeolites will include additional systems, especially EU-1 (EUO topology) and nonasil (NON)

Altogether, these calculations will further our understanding of the interplay of local structure (i.e., the surrounding part of the framework) and interactions with the organic cations that determines the dynamic behavior of fluoride. Ultimately, these findings should help to clarify the structure-directing role that fluoride anions play during zeolite synthesis.

Project-related publications

- P1** M. Fischer, *Local Environment and Dynamic Behavior of Fluoride Anions in Silico-germanate Zeolites: A Computational Study of the AST Framework*, *J. Phys. Chem. C* **123**, 1852–1865, (2019)
- P2** M. Fischer, *Influence of Organic Structure-Directing Agents on Fluoride Dynamics in As-Synthesized Silicalite-1*, *J. Phys. Chem. C* **124**, 5690–5701, (2020)

Project-related presentations

- P3** M. Fischer, *First-principles calculations elucidate the dynamic behaviour of fluoride anions in all-silica and silicogermanate zeolites*, poster presentation at the 31st German Zeolite Meeting (DZT31), Dresden, March 2019
- P4** M. Fischer, *First-principles calculations elucidate the dynamics of extra-framework species in zeolites*, oral presentation at GeoMünster 2019, Münster, September 2019

References

- [1] A. F. Masters, T. Maschmeyer, *Microporous Mesoporous Mater.* **142**, 423–438 (2011)
- [2] M. A. Cambor, L. A. Villaescusa, *Top. Catal.* **9**, 59–76 (1999)
- [3] P. Caullet, J. Paillaud, A. Simon-Masseronet et al., *Comptes Rendus Chim.* **8**, 245–266 (2005)
- [4] Y. Wang, J. Song, H. Gies, *Solid State Sci.* **5**, 1421–1433 (2003)
- [5] C. Schott-Darie, J. Patarin, P. Y. Le Goff et al. *Microporous Mater.* **3**, 123-132 (1994)

- [6] M. Estermann, L. B. McCusker, C. Baerlocher et al. *Nature* **352**, 320–323 (1991)
- [7] H. Koller, A. Wölker, L. A. Villaescusa et al., *J. Am. Chem. Soc.* **121**, 3368–3376 (1999)
- [8] S. L. Brace, P. Wormald, R. J. Darton, *Phys. Chem. Chem. Phys.* **17**, 11950–11953 (2015)
- [9] J. Martinez-Ortigosa, J. Simancas, J. A. Vidal-Moya et al., *J. Phys. Chem. C* **123**, 22324–22334 (2019)

6.4 **hbc00034: Aminoacids-Functionalized Platinum Nanoparticles as Asymmetric Heterogeneous Catalysts**

| | |
|--------------------|---|
| HLRNProject ID: | hbc00034 |
| Run time: | I/2019 – I/2020 |
| Project Leader: | Dr. Massimo Delle Piane |
| ProjectScientists: | Dr. Sebastian Kunz ¹ , Prof. Lucio Colombi Ciacchi ² , Mr. Filippo Balzaretti ² , Mr. André Wark ² |
| Affiliation: | ¹ Institute for Applied and Physical Chemistry (IAPC), Faculty of Chemistry, University of Bremen ² Bremen Centre for Computational Materials Science (BCCMS) and Hybrid Materials Interfaces (HMI) group, Faculty of Production Engineering, University of Bremen |

Overview

Since the discovery of the fatal effect of one of thalidomide enantiomers on embryos the demand of chiral chemical products and drugs has continuously increased. Today more than 80% of all drugs are brought to market as enantiopure compounds. However, the majority is still produced by synthesis of the corresponding racemate (1:1 mixture of the two stereoisomers) followed by separation of the two enantiomers. This leads to a considerable waste of resources and emphasizes the need for stereoselective preferably catalytic synthetic routes in order to operate at low temperatures with high reaction rates.

In homogenous catalysis, stereoselectivity can be achieved by metal atoms, whose catalytic properties are fine-tunable by coordinating ligands. A huge pool of chiral ligands and homogeneous catalysts with high stereoselectivities has been developed over the last 50 years. However, the difficulties of catalyst recycling and establishing continuous processes often limit the applicability of metalorganic homogeneous catalysts for industrial processes. For this reason, the development of novel efficient stereoselective heterogeneous catalysts represents a very desirable but rather challenging goal. This sets the targets for the design of an asymmetric catalyst that is heterogeneous, highly active, stereoselective and takes advantage of a simple preparation.

We have recently proposed a new approach, following the basic idea of modifiers (i.e. covering the surface with an organic molecule) by taking advantage of tightly binding ligands that functionalize the particle surface. It is based on functionalizing platinum (Pt) nanoparticles with the aminoacid L-proline (PRO). The obtained stereoselectivity represents so far the best catalytic system in the context of asymmetric heterogeneous catalysis. This demonstrated that it is possible to achieve an asymmetric molecular control that depends merely on ligand-reactant interactions like in homogeneous catalysis.

Understanding the ligand-reactant interaction is then a key challenge on the way to design highly stereoselective catalysts (Fig. 1): a ligand-reactant interaction model for the hydrogenation of β -keto esters over PRO-functionalized Pt-NPs was proposed. This model predicts the final stereochemistry of the reaction, based on the energy difference between competing interaction configurations between the reactant and the ligand, with different prochiralities.

The PRO model suggested that α -amino acids in general should be well suited as ligands for stereoselective hydrogenation of β -keto esters due to distinctive intermolecular interactions.

This hypothesis has been very recently tested, by experimentally studying the influence of the structure of 8 different α -amino acid ligands on the stereoselectivity of functionalized Pt NPs for the same hydrogenation reaction and for different reactants.

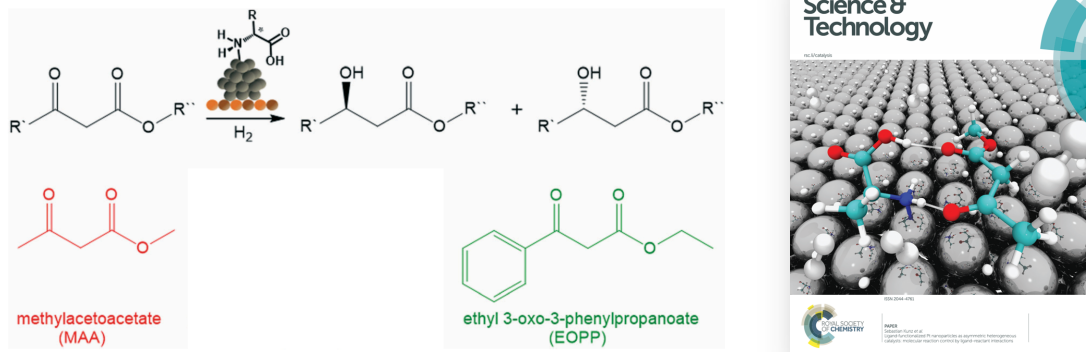


Figure 1: Left: Catalytic hydrogenation reaction (top) and the two different β -keto esters explored as reactants for the hydrogenation over ligand-functionalized Pt-NPs. Right: Cover of *Catal. Sci. Technol.* highlighting the modeling performed by us on the system.

The aim of this project was to use quantum mechanical simulations of the experimental system to verify and further refine this introduced interaction model, by testing several amino acid-reactant pairs, looking for confirmation of the experimentally measured dependency with respect to the chemical nature of the involved molecules.

Results

During the course of the project, we have extended the quantum mechanical investigation of the experimental system. We have tested all the 8 amino acids (L-alanine, L-(+)-2-aminobutyric acid, L-valine, L-*tert*-leucine, L-phenylglycine, 4-fluoro-L-2-phenylglycine, *O*-*tert*-butyl-L-serine, L-threonine) used as a ligand in our previous experimental investigation by sampling the configurational landscape of the interaction between the bound amino acids and two β -keto esters, namely methylacetoacetate (MAA) and ethyl-3-oxo-3-phenylpropanoate (EOPP). The choice of these two reactants is driven by the desire to investigate the effect of the side chains on the stereoselectivity.

The first step was to study the functionalization process of Pt nanoparticles with amino acids. The results of this task were not only required for the subsequent simulations, but they possess a scientific significance on their own. Indeed, we computed functionalization energies and determined the covalent polar nature of the newly formed N-Pt bond (whose character was still under debate), providing new insights that can guide the synthesis of these catalysts (Fig. 2).

The extremely complex configurational landscape of the interaction between the amino acids and the reactants was sampled both static and dynamically. The large number of configurations (Figure 3) to test (with multiple reactant conformations and 4 chemical groups, 2 in the amino acid and 2 in the reactant, equally available for the interaction), connected to the independency from each other, characterized the whole project as “high throughput”, possible only on the computational resources provided by HLRN.

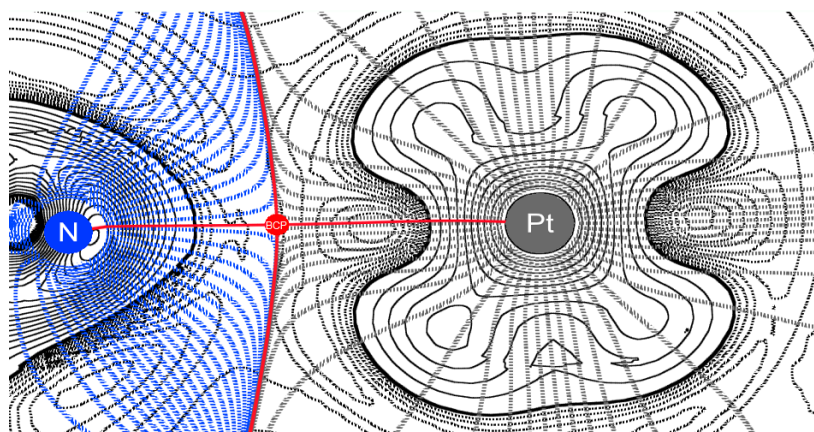


Figure 2: Plot of the electron density and the Laplacian of the Pt-N bond. Blue dot: nitrogen atom; blue dashed line: electron density of the nitrogen atom; grey dot: platinum atom; grey dashed lines: electron density of the platinum atom; red dot: bond critical point; black dashed lines: positive Laplacian; bold solid black line: Laplacian with a value of 0; solid black lines: negative Laplacian; red line between the nitrogen atom, the BCP and the platinum atom: molecular graph; red line, only intersecting the BCP: zero-flux surface.

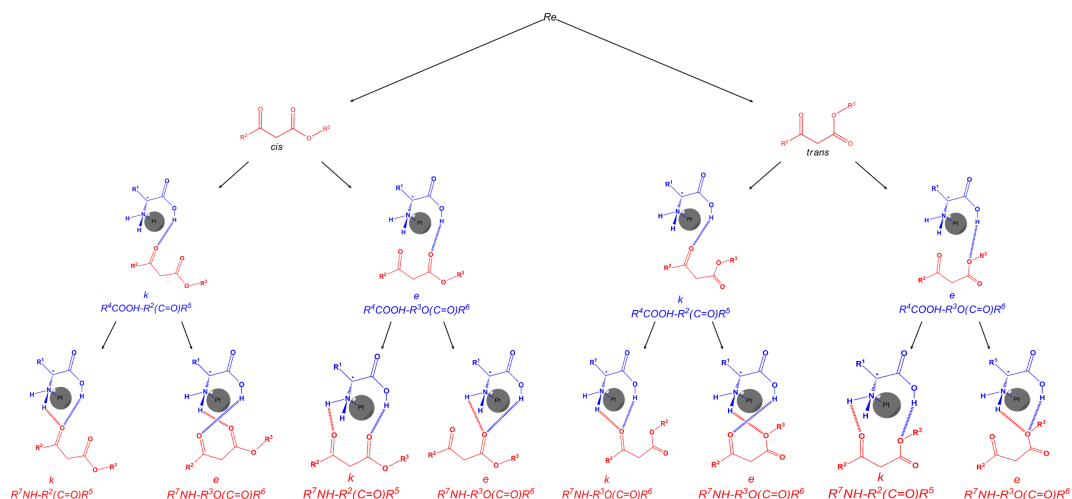


Figure 3: Classification of all possible interaction configurations between an amino acid bound to a Pt surface (blue) and a β -keto ester (red). Only configurations with Re pro-chirality are shown. An equal number of orientations can be devised for Si pro-chirality, reaching the total of 16 different possible configurations to be investigated.

We then used the accuracy of DFT to separate the different contributions to the interaction energy, particularly by verifying whether the stereoselectivity of the system is dominated by hydrogen bonding or by vdW attraction. We were able to confirm that the increase in stereoselectivity with the number of carbon atoms in the side chains of the ligands is due to the increased attractive dispersion interactions with the reactant, in just one of the two possible orientations, resulting in a favoured enantiomer as a product.

Due to the reaction happening in high hydrogen pressure, the Pt surface will quickly become covered with hydrogen atoms, resulting from the dissociation of H_2 . We are now studying the effect of surface hydrogenation on the results, revealing if the stereoselectivity is dependent on the reaction conditions. This part of the project is still ongoing at the moment of writing this report.

Outlook

The result of this study will not only afford new insights into ligand-functionalized NP catalysts, but the results will also more generally help the development of a novel approach to control the selectivity of reactions in heterogeneous catalysis by applying molecular principles from homogeneous catalysis to metal surfaces. This can open up yet unexplored possibilities for manipulating reactions on catalytic surfaces to control selectivity.

Publications

1. Sulce, A.; Backenkoehler, J.; Schrader, I.; Delle Piane, M.; Mueller, C.; Wark, A.; Colombi Ciacchi, L.; Azov, V.; Kunz, S. *Catal. Sci. Technol.* **2018**. doi:10.1039/C8CY01836G

6.5 *hbc00039*: New insights into the crystal-chemistry, mechanical properties and thermal expansion of Kentrolite and Melanotektite

| | |
|--------------------|--|
| HLRNProject ID: | hbc00039 |
| Run time: | II/2019 – IV/2019 |
| Project Leader: | Dr. M. Mangir Murshed |
| ProjectScientists: | Mathias Gogolin |
| Affiliation: | University of Bremen, Institute of Inorganic Chemistry and Crystallography |

Overview

Within the scope of this project, the thermal behavior and crystal chemistry for synthetic analogues of the two naturally occurring minerals Kentrolite ($\text{Pb}_2\text{Mn}_2\text{Si}_2\text{O}_9$) and Melanotektite ($\text{Pb}_2\text{Fe}_2\text{Si}_2\text{O}_9$), along with the structurally related β - PbAlBO_4 were investigated. Via the substitution of the Pb, Fe/Mn and Si-sites, several isostructural derivatives can be hypothesized, based on $\text{Pb}_2\text{Fe}_2\text{Si}_2\text{O}_9$. Of these hypothetical compounds, twelve candidates were chosen for test synthesis based on the results of the computational study. Lattice dynamic computations helped explain the negative linear thermal expansion behavior, which is already experimentally established in the α - and β - PbAlBO_4 compounds. Lattice dynamic calculations were also performed on $\text{Pb}_2\text{In}_2\text{Si}_2\text{O}_9$, suggesting a dynamic instability and a possible phase transition at low temperatures.

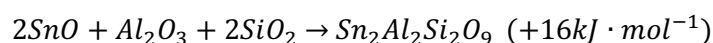
Results

A test group of 72 hypothetical compounds was proposed, based on crystal-chemical arguments (Table 1). Of them, twelve compositions are found to be energetically favorable versus their binary educts at standard conditions (Table 2).

Table 1: Hypothetical compounds to be screened by DFT-simulations.

| Composition | M(II) | M(III) | M(IV) | T(IV) |
|--|-----------------|---------------------|--------|--------|
| $\text{Bi}_2\text{M(II)}_2\text{T}_2\text{O}_9$ | Mn, Mg, Ca, Co, | - | - | Si, Ge |
| | Zn, Cu, Ni | | | |
| $\text{Sb}_2\text{M(II)}_2\text{T}_2\text{O}_9$ | Mn, Mg, Ca, Co, | - | - | Si, Ge |
| | Zn, Cu, Ni | | | |
| $\text{Sn}_2\text{M(III)}_2\text{T}_2\text{O}_9$ | - | Cr, Fe, Mn, Sc, In, | - | Si, Ge |
| | | Ga, Al, Y | | |
| $\text{Sn}_2\text{M(II)M(IV)T}_2\text{O}_9$ | Mn, Mg, Ca, Co, | - | Ti, Sn | Si, Ge |
| | Zn, Cu, Ni | | | |

The reaction-enthalpies were computed based on reactants of binary oxides, for instance:



Out of the screened compounds, the bismuth- and antimony-containing ones appear to be most promising. In the $\text{Sn}_2\text{M}_2\text{T}_2\text{O}_9$ -oxides, all the germanium-containing compounds, except for $\text{Sn}_2\text{Y}_2\text{Ge}_2\text{O}_9$, but none of the silicon-containing compounds are found to be energetically stable. Thus, the tin-based oxides energetically favor germanium over silicon on the tetrahedral site.

Table 2: Enthalpy ranges for select oxides.

| Composition | $\Delta H_r^0 / \text{kJ} \cdot \text{mol}^{-1}$ | | | | | | |
|--|--|------------|-----------|------------|------------|------------|-----|
| | Ca | Mg | Al | Ga | In | Sc | Y |
| $\text{Bi}_2\text{M}_2\text{Si}_2\text{O}_9$ (M=Ca,Mg) | -45 | -48 | | | | | |
| $\text{Bi}_2\text{M}_2\text{Ga}_2\text{O}_9$ (M=Ca,Mg) | -77 | -65 | | | | | |
| $\text{Sb}_2\text{M}_2\text{Si}_2\text{O}_9$ (M=Ca,Mg) | -41 | -40 | | | | | |
| $\text{Sb}_2\text{M}_2\text{Ge}_2\text{O}_9$ (M=Ca,Mg) | -69 | -56 | | | | | |
| $\text{Sn}_2\text{M}_2\text{Si}_2\text{O}_9$ (M=Al,Ga,In,Sc,Y) | | | +16 | +16 | +27 | +21 | +58 |
| $\text{Sn}_2\text{M}_2\text{Ga}_2\text{O}_9$ (M=Al,Ga,In,Sc,Y) | | | -6 | -13 | -13 | -15 | +14 |

Throughout the calculation period, the d-block elements, other than Sc and Y, posed challenges in terms of computational stability, and were not considered further.

Thermal expansion in $\beta\text{-PbAlO}_4$

The thermal behavior of α - and $\beta\text{-PbAlBO}_4$ was previously followed by in-situ x-ray diffraction experiments. In these experiments both compounds showed axial negative thermal expansion. Computational resources granted through the HLRN "Vorbereitungskennung" were used to elucidate the microscopic origin of this behavior for the α -polymorph. As part of the project (hbc00039), a similar expansion mechanism was confirmed for the β -polymorph of this composition. These results further substantiate the role of the lone-pair induced topology of these compounds in their mechanical and thermal behavior (Figure 1).

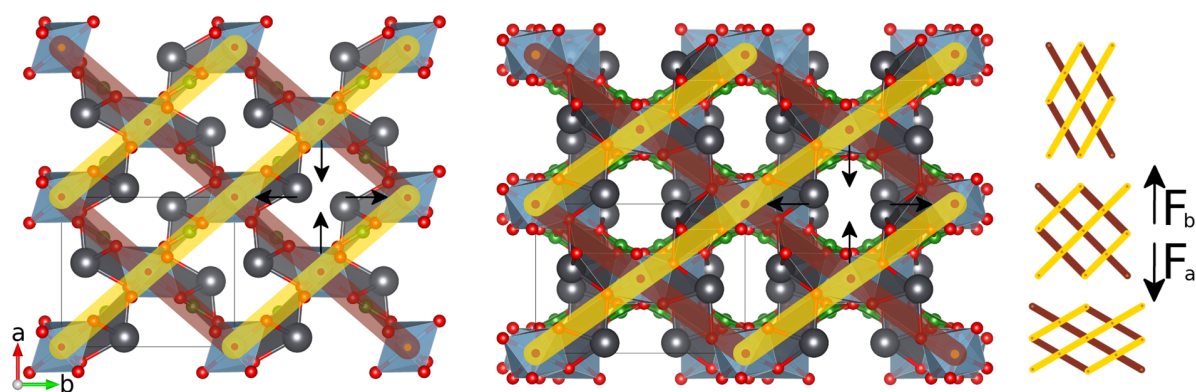


Figure 1: Schematic mechanism for the mechanical behavior of α - (left) and $\beta\text{-PbAlBO}_4$ (right)

Further details on this investigation can be found in our recent publication about the thermal behavior of α - and $\beta\text{-PbAlBO}_4$ [1].

Thermal expansion anomalies in the Kentrolite-family

The Kentrolite family of compounds was selected for further research on anomalous thermal expansion behavior, due to its structural similarity to β -PbAlBO₄. Originally, Pb₂Fe₂Si₂O₉ was selected as the representative for these materials but convergence issues related to the d-electrons made it necessary to switch to Pb₂In₂Si₂O₉. The lattice-dynamics simulations for the indium-containing member showed imaginary (negative) vibrational frequencies, suggesting the dynamic instability of the compound in the given space group (*Pna2*₁) at low temperature. This agrees with the anomalies in the lattice thermal expansion behavior at ~67 K and 153 K (Figure 2), indicating possible phase transitions at these points.

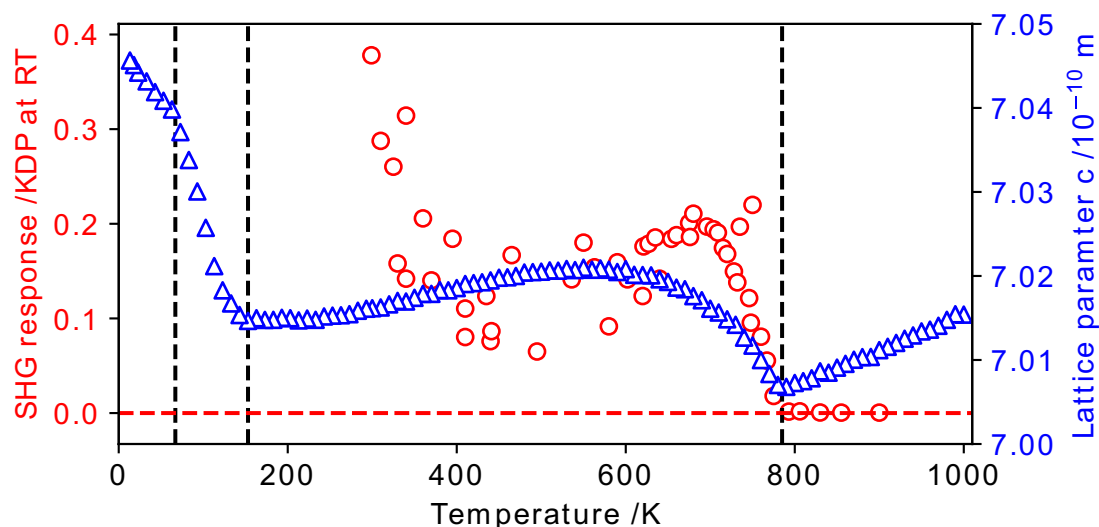


Figure 2: The c lattice parameter and second harmonic generation signal as a function of temperature.

The sharp drop of the second harmonic generation (SHG) signal and the discontinuous behavior in the lattice thermal expansion at ~780 K confirmed the displacive phase transition from non-centrosymmetric (*Pna2*₁) into centrosymmetric (*Pbcn*) space group. Using lattice dynamics simulations, performed on the HLRN facilities, the positive thermal expansion trend after 780 K could be computationally reproduced. The full evaluation of the computational results, to better understand the behavior, is still ongoing.

Outlook

Screening of novel compounds

While the instability of the tin-silicon compounds (Table 2) matches our previous experimental evidence on Sn₂M₂Si₂O₉ (M = Al, Ga, Fe, Cr), further experiments are required to confirm the existence of the bismuth-, antimony- and tin-germanium compounds.

Thermal properties of the Kentrolite-compounds

The thermal expansion mechanism in the Kentrolite family appears to be more diverse than in their structural relatives (PbAlBO₄). In particular, the indium-containing member is found to be more complex than previously expected (Figure 2). Both the computational results, as well as the thermal expansion behavior suggest dynamic instability of the structure in the room-temperature space group (*Pna2*₁). A proposal for low-temperature synchrotron single crystal diffraction has been submitted to the European Synchrotron Radiation Facility (ESRF), in order to investigate possible phase-transitions at low temperatures.

Material property predictions

All computations on the elastic properties and lattice dynamics for $\text{Pb}_2\text{Al}_2\text{Si}_2\text{O}_9$ and $\text{Pb}_2\text{In}_2\text{Si}_2\text{O}_9$ were successfully completed within this project. The full evaluation of this data and construction of models for the thermal behavior of these compounds are currently underway. Likewise, the full evaluation of the computational bandgaps will follow in the future.

Publications

[1] M. Gogolin, M.M. Murshed, M. Ende, R. Miletich, T.M. Gesing, J. Mater. Sci. 55 (2020) 177–190.

Poster-presentations

- 2019 Conference of the German crystallographic society "Comparative study on the axial negative thermal expansion of linear α - and zig-zag chain backboned β - PbAlBO_4 ."
- 2019 Springtime-symposium of the German chemical society "Negative compressibility driven thermophysical properties of α - and β - PbAlBO_4 "
- 2019 European Crystallographic Meeting "The microscopic origin of axial negative thermal expansion and negative linear compressibility in α - and β - PbAlBO_4 "

6.6 *hbi00033*: Flow transitions and regimes in core-annular pipe flow

HLRNProject ID: hbi00033
 Run time: I/2016 – II/2020
 Project Leader: Prof. Dr. Marc Avila
 Project Scientists: C. Plana, Dr. B. Song
 Affiliation: Center of Applied Space Technology and Microgravity (ZARM) Universität Bremen

Overview

Core-annular pipe flow (CAF) has applications in transporting highly viscous fluids, such as crude oil in pipelines, as well as in microfluidic flows. However, the perfect core-annular flow is in general linearly unstable and can exhibit multiple flow configurations, such as bamboo waves, slug flow, bubble flow, and oil in water dispersion, as a function of the operating conditions. The core annular flow has been investigated widely, mainly in experiments, and some rather crude phase-diagram was given in terms of dimensional parameters, such as the nominal water flow rate and oil flow rate. For generality, the phase-diagram in terms of non-dimensional control parameters (e.g., Reynolds number) is highly desired for applications to different experimental setups and flow conditions, and for in-depth theoretical investigation on the bifurcation leading to different flow patterns. This project aims to probe the phase-diagram of Core-annular pipe flow using direct numerical simulation (DNS) of the Navier-Stokes equations together with the Cahn-Hilliard equation that allows to naturally capture the interface in the binary fluid system.

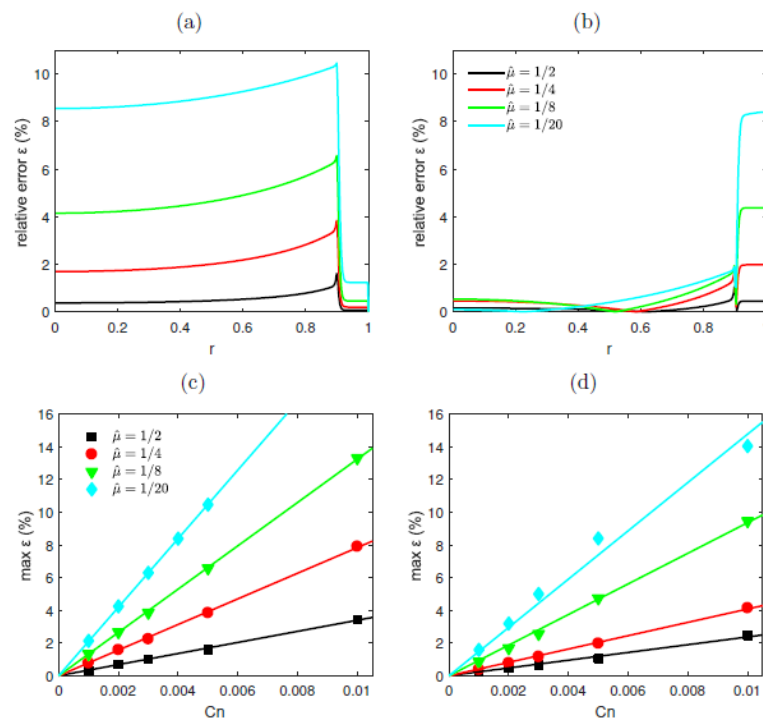


Figure 1: Convergence study of phase-field CAF to analytical solution. a) relative error of pressure-driven flow. b) relative error of volume flux-driven flow. c) convergence of pressure-driven flow. d) convergence of volume flux-driven flow.

Results

Last year we saw the publication of our paper on the simulation of CAF using the phase-field method [1]. The paper demonstrates the ability of the phase-field method to accurately deal with non-Cartesian geometry, strong advection, unsteady fluctuations and large viscosity contrast. It focuses on quantitative results, with a good agreement with literature.

During the first phase of 2019 we focused in the implementation and optimization of a hybrid MPI-OMP parallelization of our code for the solution of the combined Cahn-Hilliard-Navier-Stokes system in pipe flow. This allows us to increase the computational speed and the grid resolution. Right now we are able to achieve resolutions on the order of $3 \cdot 10^8$ DOF, needed when the flow becomes turbulent at larger values of Re .

In the second phase, we continued our study of the transition to turbulence of core-annular flow at moderate Re . We used a mixture of kerosene and water for this problem, since it is widely used in the literature and presents a moderate viscosity and density ratios ($\hat{\rho} = 0.79, \hat{\mu} = 1.6$). Starting with laminar CAF, we perturbed the flow and let it evolve. We studied the linear instabilities and transition regions in the regimes ($Re = 3000-6000$). We already managed to reach saturated conditions at lower Reynolds number (see fig. [2] and [3]), observing the breaking of the laminar CAF configuration.

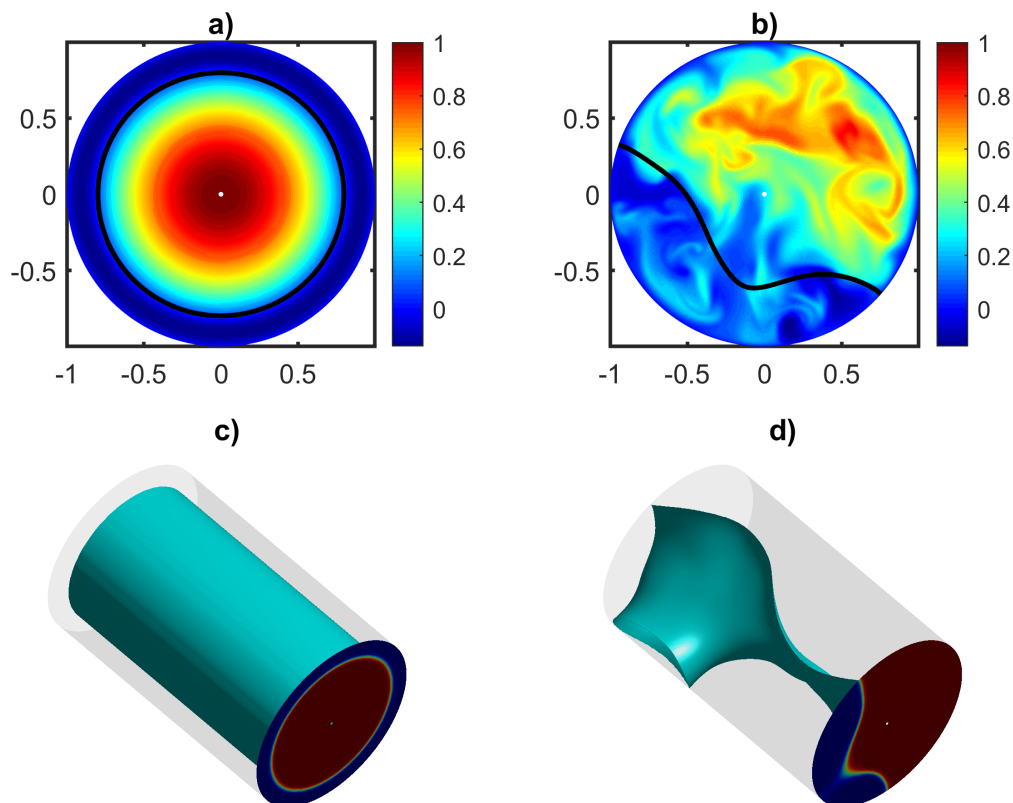


Figure 2: Transition to turbulence in water/kerosene CAF at $Re = 3000$. a, b): Axial velocity with interface as black line. c, d) 3D isosurface of the interface.

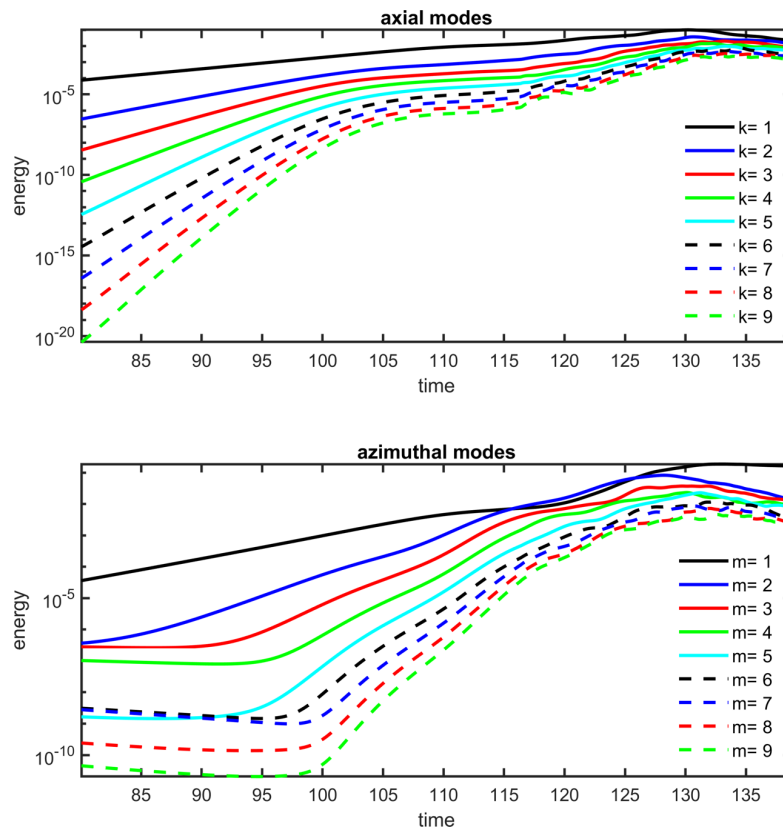


Figure 3: Energy saturation of larger axial and azimuthal scales at $Re = 3000$.

Outlook

We are currently focusing on the study of the transition to turbulence of CAF at increased Re ($Re = 9000-12000$). Additionally, we expect to run simulations with reduced interface thickness in order to increase the accuracy

Publications

1. B. Song, C. Plana, J.M. Lopez, M. Avila, Phase-field simulation of core-annular pipe flow, *International Journal of Multiphase Flow*. 117 (2019) 14-24

Presentations

2. C. Plana, B. Song, M. Avila, 17th ETC, Università di Torino, September 3, 2019
3. C. Plana, B. Song, M. Avila, 9th EPFDC, TU-Ilmenau, July 16, 2019

6.7 *hbi00036*: Fluid Dynamics Investigation of the Effect of Stresses Exerted in the Premix Emulsification Process of o/w Protein Stabilised Emulsions

| | |
|---------------------|--|
| HLRN Project ID: | hbi00036 |
| Run time: | II/2019 – I/2020 |
| Project Leader: | Prof. Dr.-Ing. habil. Fritsching |
| Project Scientists: | A. Kyrloglou, M.Sc. |
| Affiliation: | University Bremen, Particles and Process Engineering, FB4 FG01 |

Overview

Emulsification in its nature is a dynamic and highly transient environment of fluid motion in extremely confined spaces. As such the shear stress exerted between the fluids and the membrane walls as well as between the fluids themselves at their interface can rise to significant orders of magnitude. With this in mind, it is important to note that a lot of relevant to the industry fluids, such as polymer or protein solutions, have been observed to exhibit non-Newtonian behaviour when under stress. Ergo, understanding the non-Newtonian fluid behaviour, i.e. the adapting of a fluid's viscosity based on the exerted on it stress, is a critical factor in obtaining the required product emulsion.

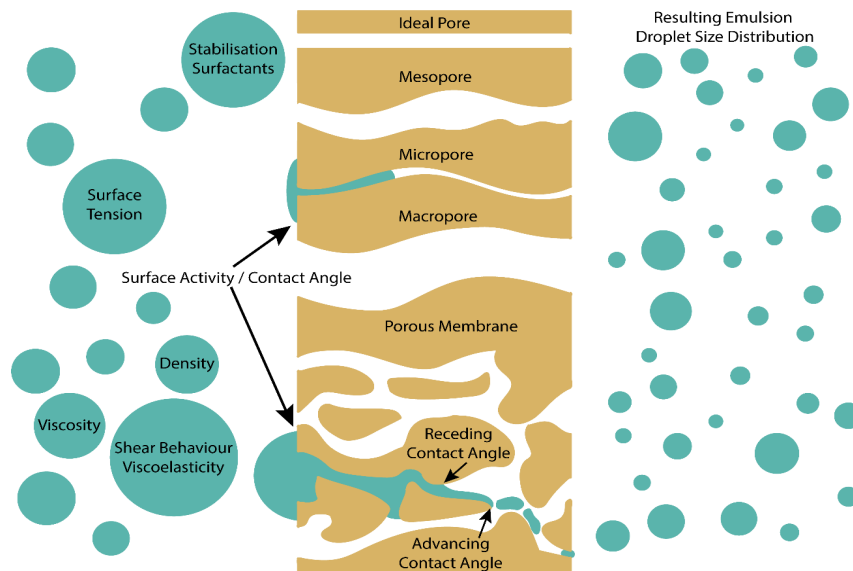


Figure 1: Parameters around membrane emulsification.

Results

The work undertaken so far has mainly involved fluid flow around sphere packings. Random generated packings of various porosities as well as sphere sizes were generated. Until now single-phase flow simulations have been carried out to test and evaluate the fitness of the generated geometries for emulsification simulations. This mainly involved making sure the wall side streams were reduced to a minimum to ensure the fluid flow goes through the packing and not around it. An exemplary simulation of one such packing as well as a 3D render of the equivalent packing can be seen in Figure 2. The long term aim for the HLRN Project is to run

single as well as multiple droplet simulations through such packings and study the transport and break-up mechanisms in this high stress environment.

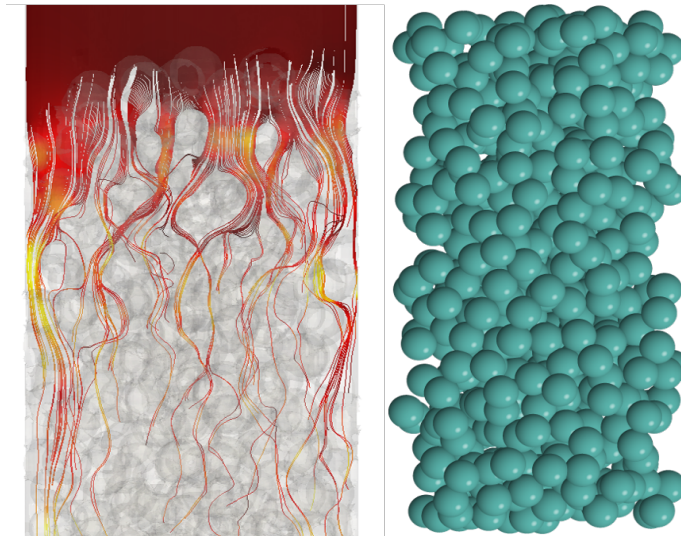


Figure 2: Left) Exemplary single-phase water flow simulation through a sphere packing. Right) A random generated sphere packing.

Furthermore similar droplet emulsification simulations in more complex geometries such as the CT-Scanned membrane illustrated in Figure 3 below will be carried out.

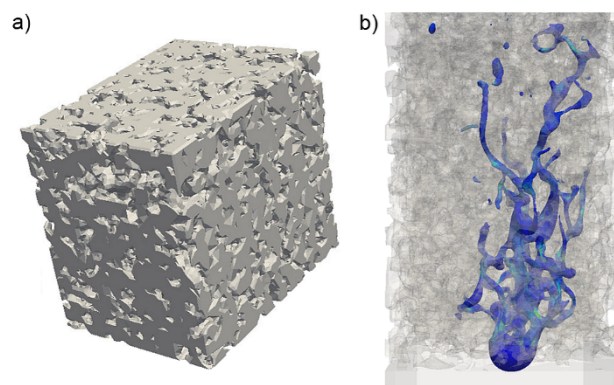


Figure 3: Left) CT-Scan of a sintered glass membrane (P2, ROBU) Right) Simulated droplet behaviour in the structure. (Wollborn et al., 2019)

Outlook

The most important step from this point on is for the viscoelasticFluidFoam solver to be coupled with interFoam and updated to OpenFOAM 7. This will allow us to use the latest tools available for two-phase flow simulations coupled with the relevant Newtonian or non-Newtonian properties for each fluid. The solver will of course need to be validated based on published experimental data for standard geometries as well as by own experiments in 3D printed idealised porous geometries. Moreover, Lattice Boltzmann simulations will be set-up for the various geometries and, in the beginning, only Newtonian fluids and comparing them with the OpenFoam and experimental results as well.

Publications

1. Wollborn, T., Luhede, L., & Fritsching, U. (2019). Evaluating interfacial shear and strain stress during droplet deformation in micro-pores. *Physics of Fluids*, 31(1), 012109. <https://doi.org/10.1063/1.5064858>

6.8 *hbi00037*: Molekulardynamische Untersuchung der Stressbeanspruchungen auf Proteine an der Phasengrenzfläche beim Premix-Membranemulgieren

| | |
|-----------------------|--|
| HLRN Project ID: | hbi00037 |
| Laufzeit: | I/2019 – I/2020 |
| Projektleiter: | Prof. Dr.-Ing. habil. Udo Fritsching |
| Projektbearbeiter: | M.Sc. Patrick Giefer |
| Institut/Einrichtung: | Fachgebiet Mechanische Verfahrenstechnik, Universität Bremen |

Überblick

Emulgierv Verfahren werden im Rahmen des Downstream-Prozessierens und der Weiterverarbeitung/Formulierung zur Homogenisierung oder auch Verkapselung in biogenen Produkten eingesetzt. Beim Premix-Emulgieren wird eine grobdisperse Voremulsion mittels der Dispergierung in porösen Membranen in eine Feinemulsion bzw. -dispersion überführt. Insbesondere das Stress-Verweilzeitverhalten und die darauf erfolgende Reaktion eines protein-stabilisierten dispersen Systems bedarf einer vertieften wissenschaftlichen Klärung. Hieraus können mechanistische Schädigungsmodelle abgeleitet werden. Die im Emulgier-Prozess auftretenden mikromechanischen Belastungen auf biologische Systeme sind nicht vollständig geklärt, die Prozessumgebung ist somit noch weiter zu entwickeln im Hinblick auf die Anpassung an spezielle biologische Systeme. Um den Einfluss des Premix-Emulgiervfahrens und der dabei auftretenden Stress-Verweilzeit-Belastungen auf die agglomerierten Proteine (hier β -Lactoglobulin) im Fluid und an den Phasengrenzflächen zu untersuchen, werden numerische Untersuchungen auf molekular-dynamischer Ebene an Proteinstrukturen durchgeführt. Diese Untersuchungen zeigen, inwieweit die Proteinstrukturen durch den Emulgiervorgang belastet und geschädigt werden können, beziehungsweise ob eine proteinschonendere Emulgierung mit den Membranen möglich ist.

Ergebnisse

Zielsetzung des vorangegangenen Projektzeitraumes war der Aufbau und die Untersuchung von Proteinschichten an Öl-Wasser-Grenzflächen und die Beschreibung der Auswirkungen strömungsinduzierter Scherbelastungen auf die adsorbierten Strukturen.

Dazu wurden Proteinschichten mit unterschiedlichen Belegungsdichten aufgebaut. Anstelle von Einzelproteinen wurden mehrere Proteine an der Phasengrenzfläche platziert und der Adsorptionsvorgang simuliert. Dazu wurden Belegungsdichten von 4, 6 und 10 Proteinen simuliert, um die Belegung der Phasengrenzflächen von teilbelegt bis zum Monolayer abzudecken, wie in Abb. 2 dargestellt. Um darüber hinaus den Einfluss unterschiedlicher Adsorptionskonfigurationen der einzelnen Proteine in der Schicht abschätzen zu können, wurde jedes Szenario mit drei unterschiedlichen Anfangsorientierungen der Proteine durchgeführt. Weiterhin wurde der pH-Wert zwischen 3 und 7 variiert.

Im Anschluss wurde die Entfaltung der Proteinfilme an den Phasengrenzflächen untersucht, sowie die Beanspruchung dieser Filme durch einen Schergradienten. Der Fokus dieses Vorhabens liegt einerseits auf der Analyse der strukturellen Veränderung der Proteine und andererseits auf der möglichen gegenseitigen Beeinflussung bei der Scherbeanspruchung.

All diese Vorhaben konnten nur dank der Bereitstellung von Rechenkapazität durch den HLRN durchgeführt werden. Es wurden umfangreiche Daten generiert, die sich aktuell in der Auswertung durch den vorherigen Projektbearbeiter befinden. Eine Veröffentlichung ist ebenfalls in Arbeit, zu der bereits ein Manuskript ausgearbeitet wird.

Zur Klärung der im Prozess auftretenden Stressbeanspruchungen wurden fluiddynamische Untersuchungen in porösen Strukturen in einem kooperierenden HLRN-Projekt (hbi00036) durchgeführt.

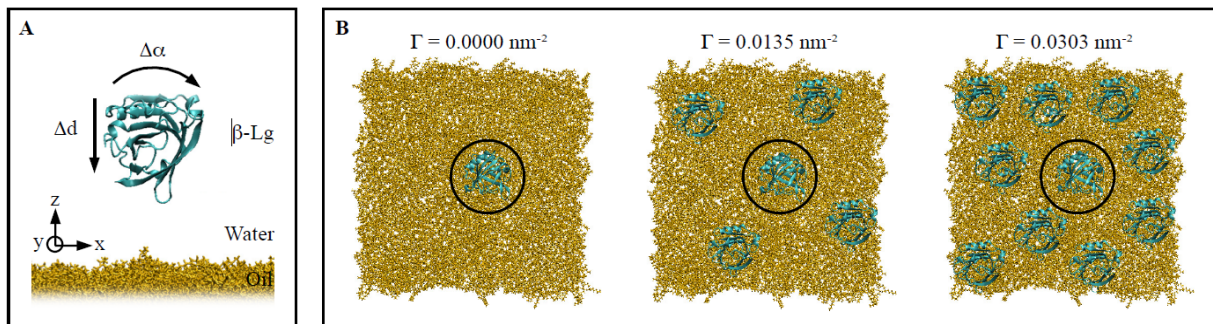


Abbildung 1: statische MD Simulation zur Untersuchung der möglichen gegenseitigen Beeinflussung des Adsorptionsvorganges der Einzelproteine

Ausblick

Als weiterer Mechanismus, der zur Veränderung des Grenzflächenverhaltens führen kann, werden Hochdruckschädigungen der Proteine betrachtet. Dazu wird zunächst ein Einzelprotein in einer Hochdrucksimulation geschädigt. Erste Simulationen haben eine Entfaltung der Proteine als Folge des Hochdrucks gezeigt. Durch die Entfaltung lässt sich eine erhöhte Grenzflächenaffinität vermuten, die im weiteren Verlauf des Projektes untersucht wird.

Eine Erweiterung des Systems auf mehrere Proteine ist geplant, um eine mögliche gegenseitige Beeinflussung abzudecken.

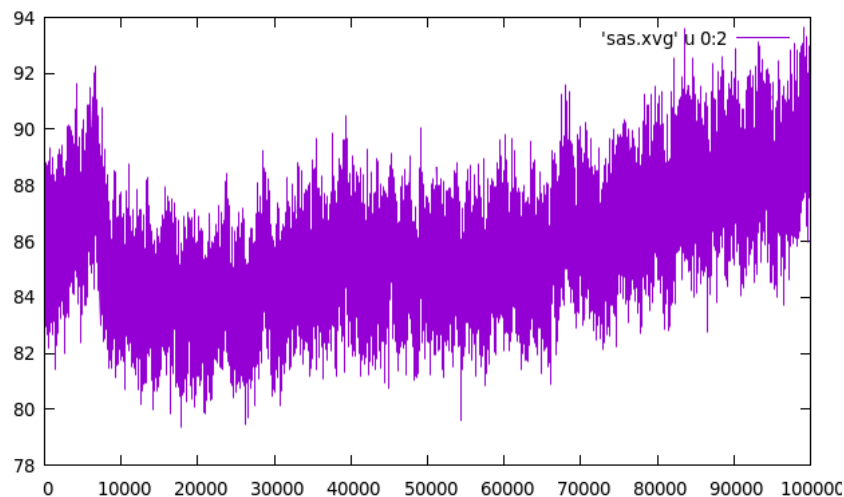


Abbildung 2: Darstellung der Solvent-Accessible-Surface bei Hochdruckschädigung von β -Lactoglobulin bei 600MPa für 1000ns

6.9 *hbi00038*: Direct Numerical Simulation and Modeling of Turbulent Convection in Porous Media

| | |
|---------------------|---|
| HLRNProject ID: | hbi00038 |
| Run time: | I/2019 – IV/2019 |
| Project Leader: | Dr. Yan Jin |
| Project Scientists: | Stefan Gasow; Feixiong Rao |
| Affiliation: | Center of Applied Space Technology and Microgravity (ZARM), Uni. Bremen |

Overview

A porous medium is a material containing a porous matrix and pores. The porous matrix is usually solid while the pores are filled with a fluid (liquid or gas). A wide range of materials falls to porous media under this definition, e.g. sponges, wood, sand or body tissues. Porous media like materials have been widely used in heat and mass transfer applications since their high surface area to volume ratio may significantly enhance heat and mass transfer.

Design and optimization of these engineering applications require accurate simulation of convection in porous media. Porous medium convection was traditionally calculated by solving the macroscopic equations. However, the physics of it is still not clear. Significant simplifications and strong assumptions have been made in these macroscopic equations. For example, the turbulent momentum and thermal dispersion terms were often neglected. In addition, there are still contradictory views on whether there is macroscopic turbulence in porous media. As a result, numerical simulation results sometimes have considerable model errors. More efforts are required to develop more accurate macroscopic models.

The main purpose of the proposed project is to better understand the physics of porous medium convection. Microscopic direct numerical simulation (MIC-DNS) methods, in which the detailed flows within the porous elements will be taken into account, will be used in the study. Particular attentions will be paid to natural and mixed convection problems due to their high complexity and significance in emerging industries. Through our understanding of physics, a more accurate macroscopic model for calculating porous medium convection should be developed. The developed model will be validated with our DNS results.

Results

To achieve the objectives of the proposed project, we have carried out the following work.

Direct numerical simulation of natural convection in porous media

Natural convection in porous media is a fundamental process for the long-term storage of CO₂ in deep saline aquifers. Typically, details of mass transfer in porous media are inferred from the numerical solution of the volume-averaged Darcy-Oberbeck-Boussinesq (DOB) equations, even though these equations do not account for the microscopic properties of a porous medium. According to the DOB equations, natural convection in a porous medium is uniquely determined by the Rayleigh number. However, in contrast with experiments, DOB simulations yield a linear scaling of the Sherwood number with the Rayleigh number (Ra) for high values of Ra ($Ra \gg 1,300$). Here, we perform Direct Numerical Simulations (DNS), fully resolving the flow field within the pores, see Fig. 1 for the porous matrices used in our DNS.

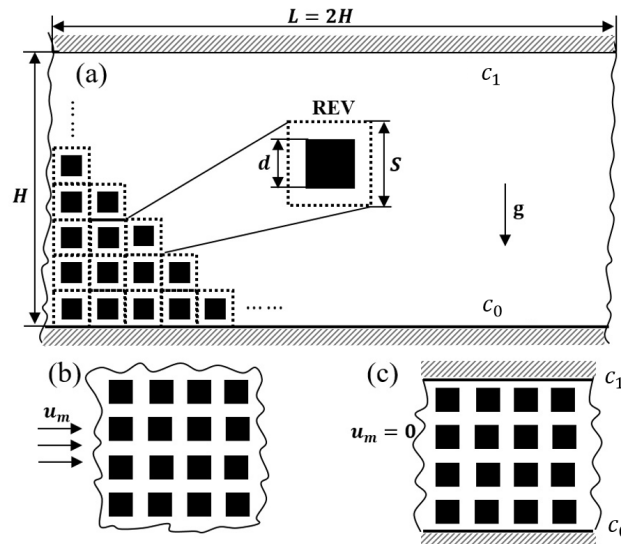


Figure 1: Porous matrices used in our DNS. In all cases, periodic boundary conditions are used in the horizontal direction. Taken from [1].

The DNS results for the temperature field are compared with the DOB results in Fig. 2. We show that the boundary layer thickness is determined by the pore size instead of the Rayleigh number, as previously assumed. The mega- and proto- plume sizes increase with the pore size. Our DNS results exhibit a nonlinear scaling of the Sherwood number at high porosity, and for the same Rayleigh number, higher Sherwood numbers are predicted by DNS at lower porosities. It can be concluded that the scaling of the Sherwood number depends on the porosity and the pore-scale parameters, which is consistent with experimental studies.

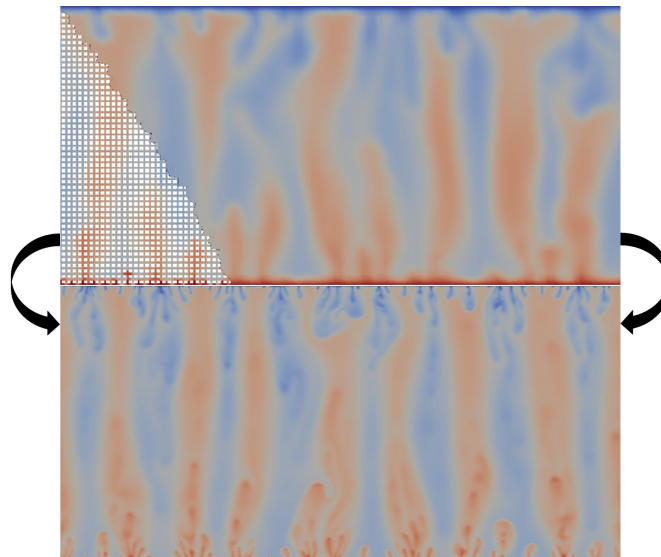


Figure 2: Temperature fields from the DNS results and the DOB results. Taken from [1].

Macroscopic modeling of flows in porous media

Based on the pore-scale-prevalence-hypothesis (PSPH), we proposed a macroscopic model that accounts for the effect of momentum dispersion on flows in porous media. The dispersion term in the macroscopic momentum equation is approximated using a Laplacian term. A local Reynolds number Re_d , which characterizes the strength of

momentum dispersion, is introduced to calculate the effective viscosity. The characteristic length used in defining Re_d is the pore size while the characteristic velocity is the mixing velocity. A Taylor expansion is made for the effective viscosity with respect to Re_d . The two leading order terms of the Taylor series are adopted in the present PSPH momentum-dispersion model. The model constants are determined from the direct numerical simulation (DNS) results of a flow in the same porous medium bounded by two walls. The effective viscosity approaches the molecular viscosity when the porosity is increased to 1. It approaches infinity when the porosity approaches 0.

The developed macroscopic equations are used to solve the flows in two types of porous media to demonstrate the utility of the developed macroscopic model. The first case deals with a flow in a channel occupied by a homogeneous and isotropic porous medium, see Fig. 3a. The second case deals with a flow in a porous medium with two porosity scales, see Fig. 3b. The benchmark studies show that the momentum dispersion can be approximated by the Laplacian term. The proposed PSPH momentum-dispersion model is highly accurate in a wide range of Reynolds and Darcy numbers as well as porosities.

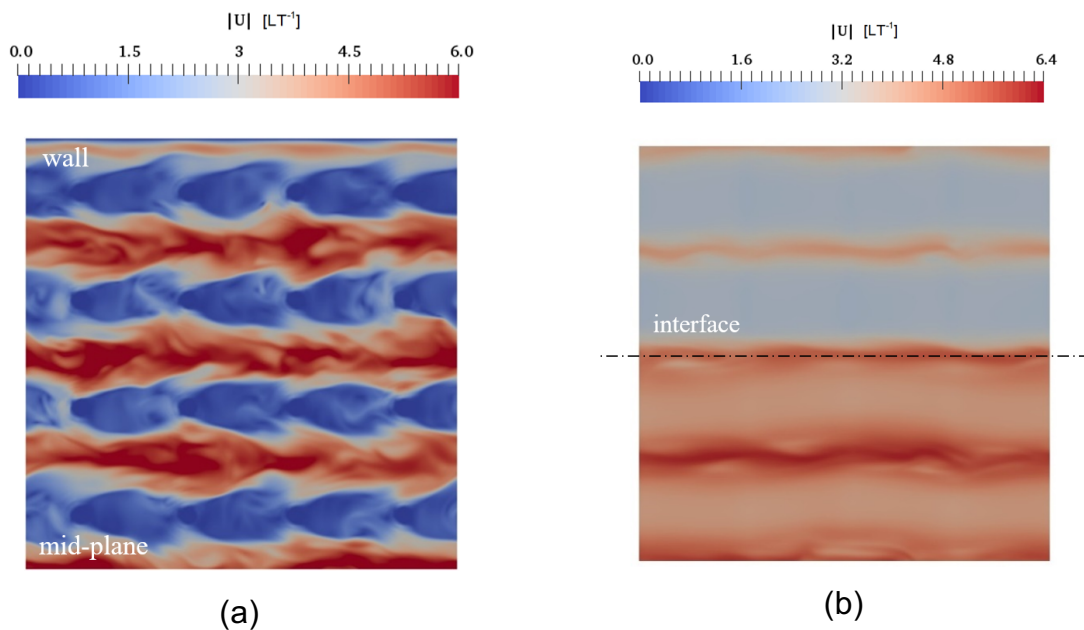


Figure 3: Instantaneous velocity magnitude. (a) Porous medium bounded by walls; (b) porous medium with two porosities.

Outlook

Our numerical study further validates the PSPH, which states that the size of turbulent eddies is restricted by the pore size. We show that the boundary layer thickness for natural convection in porous medium is determined by the pore size instead of the Rayleigh number, as previously assumed. A more accurate macroscopic model for forced/natural/mixed convection in porous media will be developed in our future work. The effect of both momentum and thermal dispersion will be taken into account. The developed model will be validated with the DNS results.

Publications

1. S Gasow, Z Lin, HC Zhang, HC, AV Kuznetsov, M Avila, Y Jin, *Effects of pore-scale on the macroscopic properties of natural convection in porous media*, J. Fluid Mech., in press (2020)
2. PU Kränzien, Y Jin, *Natural convection in a two-dimensional cell filled with a porous medium: a direct numerical simulation study*, Heat Trans. Eng., 40 (5-6), 487-496(2019)

Presentations

1. S Gasow, AV Kuznetsov, M Avila, Y Jin, 17th European Turbulence Conference (ETC-17), Torino, 2019

6.10 *hbi00041*: Large-scale energy flux in turbulent pipe flow

| | |
|---------------------|--|
| HLRN Project ID: | hbi00041 |
| Run time: | III/2019 – II/2020 |
| Project Leader: | Dr. Daniel Feldmann |
| Project Scientists: | Dr. Daniel Feldmann |
| Affiliation: | University of Bremen, Center of Applied Space Technology and Microgravity (ZARM) Am Fallturm 2, 28203 Bremen, Germany |

Where do superstructures obtain their energy from?

From weather forecast, oil spill prediction and climate modelling to the optimisation of vehicles, wind turbines and artificial heart valves: turbulent fluid flows are ubiquitous! However, understanding, predicting and modelling turbulence correctly, remains one of the greatest challenges in classical physics and modern engineering. It is estimated, that half the energy being spent worldwide to move fluids through pipes and channels or to move vehicles through air and water is dissipated by fluid turbulence in the immediate vicinity of a wall [4]. Therefore, a detailed understanding of wallbounded turbulent shear flows is of utmost importance to all engineering applications where the Reynolds number is generally high.

Highly turbulent flows carry energy in swirls and eddies of many different time and length scales. Because of its unpredictable and highly chaotic behaviour, turbulence is typically studied as a stochastic process. In his ground-breaking work, Kolmogorov [5] assumed, that turbulent flows are isotropic and homogeneous at sufficiently small scales and he showed precisely how energy is transferred from large to small eddies in a statistical sense. However, flows in nature and engineering usually feature anisotropic large-scale motions, which are often shaped by boundary conditions (e.g. walls), geometry (e.g. curvature) or source of driving (e.g. velocity, pressure or temperature gradients). As an example for the highly inhomogeneous and anisotropic nature of such flows, Figure 1a shows elongated low-momentum streaks in a turbulent pipe flow, which mainly populate the buffer layer. Streamwise streaks are probably the most prominent and best investigated structural feature of wall-bounded turbulence, first described by Kline [6]. Together with quasi-streamwise vortices, they play a major role in the self-sustaining wall-cycle and are often associated with sweep and ejection events [7]. So in practice, turbulent flows are neither isotropic nor homogeneous and with increasing Reynolds number, most wall-bounded flows additionally develop very-large scale motions or superstructures. Superstructures typically carry a substantial part of the kinetic energy of the flow and they can also determine its drag and transport properties (mass, heat, momentum). Hence, in order to go beyond state-of-the-art modelling and control strategies of wall-bounded turbulent flows, superstructures must be correctly accounted for.

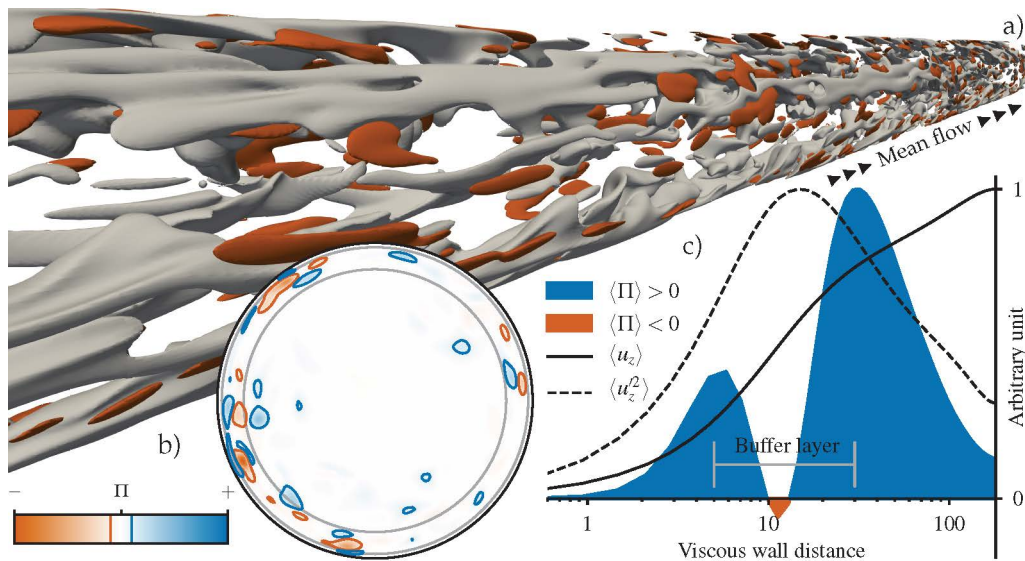


Figure 1: Typical coherent structures and inter-scale energy flux in a turbulent pipe flow DNS at $Re_\tau = 180$. a): Large connected regions of negative streamwise velocity fluctuations (grey iso-contours for $u'_z \sim -2.5 u_\tau$) represent typical low-momentum streaks in the near-wall region of the pipe domain. These elongated structures appear accompanied by much shorter regions of significant instantaneous backward energy flux (red iso-contours for $\Pi = -1/10 \max |\Pi|$). b): Forward and backward scatter events in a cross-sectional plane, which contains the most intensive backscatter event occurring in this instantaneous flow field realisation. Significant events appear clustered in the buffer layer (grey annular lines). c): Mean inter-scale energy flux as a function of the distance from the pipe wall. A distinct region of net small-to-large-scale energy flux ($\langle \Pi \rangle < 0$) indicates a localised inverse energy cascade in the buffer layer. The mean streamwise velocity $\langle u_z \rangle$ and streamwise Reynolds stress $\langle u_z'^2 \rangle$ serve as reference for regions of maximal mean shear and peak turbulence intensity. Reproduced from [1].

This project aims at analysing the onset and nature of large-scale structures in turbulent pipe flow. We are particularly interested in how kinetic energy is transferred across length scales and whether superstructures obtain their energy from e.g. the mean shear or from smaller-scale structures (i.e. backscatter). To this end, we perform highly resolved direct numerical simulations (DNS) in a large computational domain using our pseudo-spectral DNS code **nsPipe** [2]. The computed turbulent flow fields will be analysed in the following two regards.

On the one hand, we study the flux of kinetic energy across length scales based on explicit spatial filtering of the fully developed and fully resolved turbulent velocity field. We calculate and analyse the space-, time- and scale-local flux (Π^λ) of turbulent kinetic energy through a particular filter length scale (λ) based on the framework formulated by Eyink [8]. Figure 1a and b show an example of the instantaneous inter-scale energy flux field computed in one of our pipe flow DNS.

On the other hand, we probe the robustness and evolution of larger and smaller structural features with respect to each other. In addition to the fully developed DNS mentioned above, we perform numerical experiments, where we remove all scales smaller or larger than a particular λ from the fully-developed turbulent velocity field. Then we continue all three DNS with full spatial resolution, track the temporal evolution of the modal kinetic energy in particular wave numbers and monitor how the larger or smaller scales evolve from the existing small- or large-scale velocity field and how (fast) these three systems depart from each other.

How does filtering change the perspective on the scale-energetics of the near-wall cycle?

In a first step, we varied the shape of the filter kernel (Fourier, Gauss, box) used for scale-separation to systematically assess its effect on the local structure of the interscale energy flux (Π) and its statistics for one small filter length scale ($\lambda_\theta^+ \times \lambda_z^+$) = $(40^+ \times 75^+)$. The mean energy flux at each wall-normal distance is robust with respect to the filter kernel. In particular, the localised inverse energy cascade identified in the buffer layer (Figure 1c) is found for all three filter kernels. However, we identified significant differences in the estimated intensity and distribution of localised Π events. We also found conflicting correlations between typical structures in the velocity field (streaks, stream-wise vortices and Q events [7]) and regions of forward and backward scatter events in the instantaneous Π field. In particular, correlations are highly upstream-downstream symmetric for the Fourier filter, but asymmetric for the Gauss and box kernel, as expected because of the dominant stream-wise advection. More importantly, using the Gauss and box kernel we reveal a strong correlation between fluid transport away from the wall and backscatter events, which is absent for the Fourier kernel. Our results suggest that interpretations of inter-scale energy flux relying on Fourier filters should be taken with care, because Fourier filters act globally in physical space, whereas Π events are strongly spatially localised.

Outlook

In a next step, will further investigate the inter-scale energy flux based on Gauss filtering only and move to higher Reynolds number flow fields and also to larger filter scales. Simultaneously, we will record and analyse the temporal evolution of the modal kinetic energy in selected small wave numbers while starting from fully developed flow fields, which do not contain energy in length scales larger than typical near-wall structures.

Publications

1. **D. Feldmann**, M. Umair, M. Avila, A. von Kamecke, How does filtering change the perspective on the scale-energetics of the near-wall cycle?, *In preparation for Journal of Fluid Mechanics*.
2. J. M. López, **D. Feldmann**, M. Rampp, A. Vela-Martín, L. Shi, M. Avila, nsCouette – A high-performance code for direct numerical simulations of turbulent Taylor–Couette flow, *SoftwareX*, 11, 2020.

Presentations

3. **D. Feldmann**, M. Umair, J. Chen, M. Avila, A. von Kamecke, Effect of the spatial filter on one- and two-point inter-scale energy flux statistics in turbulent pipe flow, 17th European Turbulence Conference (ETC), Torino, Italy, 4th September 2019.

References

4. J. Jiménez, Cascades in Wall-Bounded Turbulence, *Annual Review of Fluid Mechanics*, 44 (1), p. 27–45, 2012.
5. A. N. Kolmogorov, Equations of turbulent motion in an incompressible fluid, *Doklady Akademiia Nauk SSSR*, 30 (4), p. 299–303, 1941.
6. S. J. Kline, W. C. Reynolds, F. A. Schraub, and P. W. Runstadler, The structure of turbulent boundary layers, *Journal of Fluid Mechanics*, 30 (12), p. 741–773, 1967.
7. J. M. Wallace, Quadrant Analysis in Turbulence Research: History and Evolution, *Annual Review of Fluid Mechanics*, 48 (1), P. 131–158, 2016.
8. G. L. Eyink, Local energy flux and the refined similarity hypothesis, *Journal of Statistical Physics*, 78 (1), p. 335–351, 1995.

6.11 *hbk00032*: Climate change and atmosphere / ocean interaction in the coupled FESOM/ECHAM model

| | |
|---------------------|------------------------------|
| HLRN Project ID: | hbk00032 |
| Run time: | III/2019 – II/2020 |
| Project Leader: | Prof. Dr. Thomas Jung |
| Project Scientists: | Dmitry Sidorenko, Qiang Wang |
| Affiliation: | AWI/Universität Bremen |

Overview

Substantial changes have occurred in the Arctic Ocean in the last decades. Not only sea ice has retreated significantly, but also the ocean at middepth showed a warming tendency. By using simulations we identified a mechanism that intensifies the upward trend in ocean heat supply to the Arctic Ocean through Fram Strait. The reduction in sea ice export through Fram Strait induced by Arctic sea ice decline increases the salinity in the Greenland Sea, which lowers the sea surface height and strengthens the cyclonic gyre circulation in the Nordic Seas. The Atlantic Water volume transport to the Nordic Seas and Arctic Ocean is consequently strengthened. This enhances the warming trend of the Arctic Atlantic Water layer, potentially contributing to the Arctic “Atlantification.” The intensification of the Atlantic Water volume transport through Fram Strait can impact not only the Arctic heat budget, but also potentially the nutrient budget and the primary production.

Results

The Arctic Ocean has undergone pronounced changes during the past decades. At the surface, the sea ice has declined in both extent and thickness. The sea ice decline results in a significant reduction in sea ice volume export through Fram Strait. Below the halocline, the Atlantic Water (AW) layer has a warming tendency. The eastern Eurasian Basin was observed to have a weaker stratification in the halocline above a warmer AW layer in recent years in comparison to the climatological condition, a phenomenon termed as Atlantification. Previous studies suggest that temperature anomalies travel from the North Atlantic through the Nordic Seas into the Arctic Ocean. It was recently shown that local processes such as the Greenland Sea Gyre circulation also influence the northward AW transport and the temperature at the Fram Strait. However, dynamical processes responsible for the recent upward trends in AW temperature and ocean heat transport at Fram Strait are not fully understood.

In this study we used numerical simulations carried out at HLRN to explore the mechanism leading to enhanced Arctic Ocean warming. The discovered mechanism is depicted in Figure 1. When sea ice declines, the Arctic sea ice volume export through Fram Strait decreases, which increases the salinity in the Greenland Sea. The halosteric height, thus the SSH, decreases in the Greenland Sea and Nordic Seas. The cyclonic gyre circulation in the Nordic Seas strengthens accordingly. The reduction of SSH and strengthening of the AW boundary current increases the AW transport into the Nordic Seas and the Arctic Ocean. The warming trends of the AW at Fram Strait and in the Arctic Ocean are thus intensified. In these processes, the Nordic Seas play the role of a switchyard, while the reduction of sea ice export flux caused by increased air-sea heat flux over the Arctic Ocean is the switchgear.

The impact of sea ice decline on the Arctic AW layer is shown in Figure 2. The largest impact is located in the Eurasian Basin, while it is visible also on the Canadian Basin side of the Lomonosov Ridge. The increased AW supply to the Arctic Ocean is clearly shown by the concentration of a dye tracer released at the Fram Strait (Figures 2c and 2f). Without Arctic sea ice decline, the Eurasian Basin also has a warming tendency during recent years (Figure 2d), because AW temperature and the volume transport at Fram Strait still have upward trends. The sea ice decline strengthens the Fram Strait inflow and increases the temperature, thus increasing the warming trend in the Arctic Ocean (Figure 2a). As some of the increased ocean heat from the Fram Strait induced by the sea ice decline is accumulated in the Arctic AW layer with time, the ocean warming trend inside the Arctic Ocean is significantly strengthened (cf. Figures 2a and 2d). Sea ice decline not only increases the AW layer temperature as found in this study, but also significantly increases the salinity in the halocline of the Eurasian Basin by changing water mass spatial distribution (Wang et al., 2019). The two effects together can contribute to the Atlantification of the eastern Eurasian Basin. The AW inflow through Fram Strait is also highly relevant for nutrient supply to the Arctic Ocean. The processes we discussed imply that the Arctic sea ice decline can also influence oceanic primary productivity in the Arctic Ocean indirectly through changing the AW inflow, besides its direct impacts, for example, through changing light availability.

Outlook

Increasing ocean heat can reduce sea ice thickness, and currently this occurs mainly in certain regions including the western Eurasian Basin near the Fram Strait and the northern Kara Sea. Although ocean heat is important for the sea ice budget in the current climate, the air-sea heat flux still plays a dominant role. However, if the ocean heat transport through Fram Strait continues to increase in the future, the induced basal melting on larger scales may reduce the sea ice volume export through Fram Strait more significantly. In this case, the feedback as depicted in Figure 1 may play an increasingly important role in strengthening the AW heat inflow and Arctic sea ice decline. The latter requires further dedicated studies.

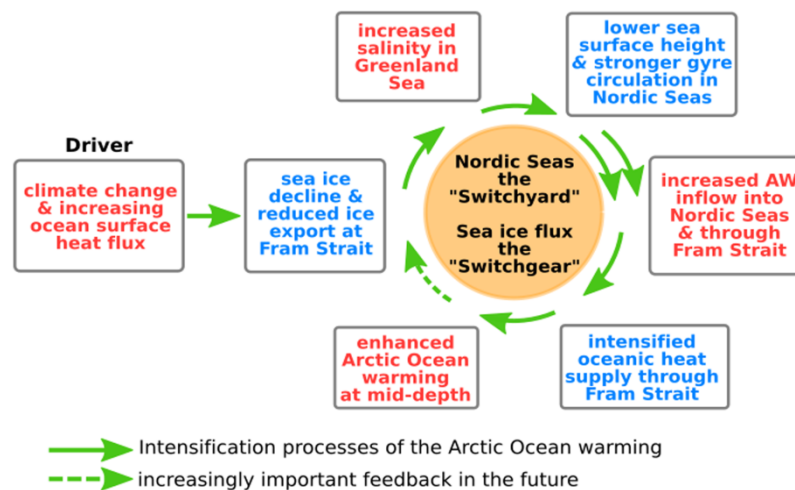


Figure 1: Schematic diagram illustrating the discovered mechanism that intensifies the warming of the Atlantic Water layer at the Fram Strait and in the Arctic Ocean at middepth.

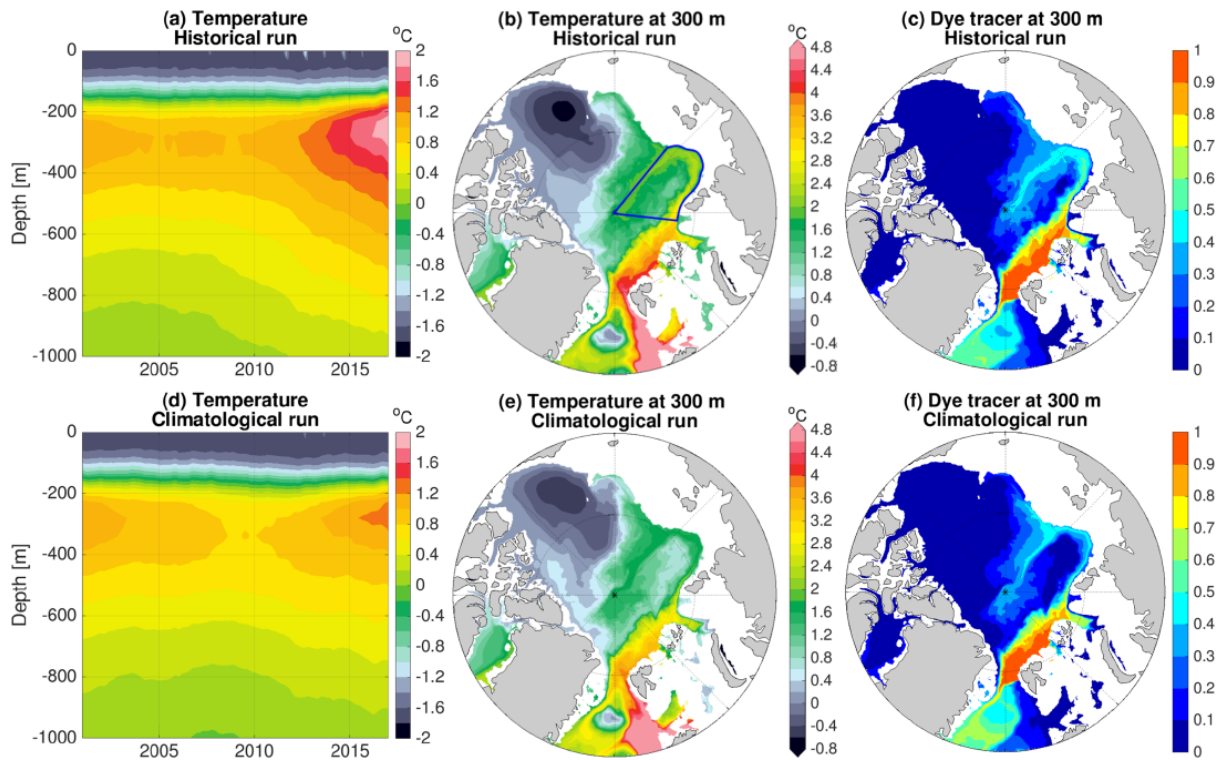


Figure 2: (a) Hovmöller diagram of temperature averaged over the eastern Eurasian Basin (indicated by the blue box in (b)) in the historical run. (b) Temperature at 300 m depth averaged over the last 3 years in the historical run. (c) Dye tracer at 300 m depth averaged over the last 3 years in the historical run; the tracer is released in the Atlantic Water layer east of 0°E at Fram Strait. (d, e, f) The same as (a)-(c), respectively, but for the climatological run. The historical run is a hindcast control run. The climatological run is the same as the historical run, except that the climatological thermal forcing is used over the Arctic Ocean.

Publications

1. Wang, Q., Wekerle, C., Danilov, S., Sidorenko, D., Koldunov, N., Sein, D., & Jung, T. (2019). Recent sea ice decline did not significantly increase the total liquid freshwater content of the Arctic Ocean. *Journal Climate*, 32, 15–32.
2. Wang, Q., Wekerle, C., Wang, X., Danilov, S., Koldunov, N., Sein, D., Sidorenko, D. von Appen, W., Jung, T. (2020). Intensification of the Atlantic Water supply to the Arctic Ocean through Fram Strait induced by Arctic sea ice decline. *Geophysical Research Letters*, 47, e2019GL086682.

6.12 *hbk00034*: Ice sheet - ice shelf - ocean interaction in the marginal seas of the Southern Ocean

| | |
|---------------------|--|
| HLRN Project ID: | hbk00034 |
| Run time: | III/2013-III/2020 |
| Project Leader: | Prof. Torsten Kanzow ^{1,2} |
| Project Scientists: | Frank Schnaase ¹ , Lukrecia Stulic ² , Dr. Ralph Timmermann ² |
| Affiliation: | ¹ University of Bremen ² Alfred Wegener Institute, Helmholtz Centre for Polar and Marine Research |

Overview

In this project we use a global sea ice – ice shelf – ocean model to study the interaction between the deep Southern Ocean, the ice shelves fringing the Antarctic continent, and the Antarctic Ice Sheet. With its unstructured grid, the Finite Element Sea ice – Ocean Model (FESOM) allows for an adequate resolution of the key regions, namely the grounding lines, the ice shelf fronts, and the continental shelf break. We are particularly interested in water mass exchange between the deep ocean and the continental shelf, and the pathways of water in the sub-ice cavities. We have developed a coupled ocean – ice shelf - ice sheet model, which enables us to investigate the relevant processes in decadal to centennial-scale simulations in a consistent way. With the high computational burden imposed by the use of a finite-element ocean model (to which there is no alternative if local processes are to be represented in a global system), the project depends on resources provided through the HLRN.

Results

Ice-shelf basal melting has been shown to be an important component in the southern hemisphere's ice mass budget and its variability. In order to explore mechanisms of ice-ocean interaction and the potential of substantial changes to ice-shelf basal mass loss in a warmer climate, we use the global Finite Element Sea ice–ice shelf–Ocean Model FESOM (Timmermann et al., 2012) with a high resolution in the Antarctic marginal seas. A key achievement of the past year is the successful implementation of a new coupled ocean – ice shelf – ice sheet model (FESOM-PISM) with an explicit representation of variable cavity geometry and grounding line dynamics. This was achieved in close collaboration with Dr. Torsten Albrecht (Potsdam Institut for Climate Impact Research, PIK) and supported by funding from the DFG SPP “Antarktischforschung”. Similar to the Regional Antarctic and Global Ocean (RAnGO) model (Timmermann and Goeller, 2017), the coupled system is based on a global FESOM implementation with a mesh that uses hybrid vertical coordinates and is substantially refined in the marginal seas of the Southern Ocean. The Antarctic cryosphere is now represented by a regional setup of the Parallel Ice Sheet Model PISM, comprising the Filchner-Ronne Ice Shelf (FRIS) and the grounded ice in its catchment area up to the ice divides. At the base of the FRIS, melt rates and boundary layer temperatures from FESOM are applied. PISM returns ice thickness and the position of the grounding line. Dynamic FESOM mesh modification and several other aspects of the RAnGO coupler have been adopted to the new system. The ice sheet model is run on a horizontal grid with 1 km resolution to ensure an appropriate representation of grounding line processes. Enhancement factors for the approximation of the stress balance, as often used in coarse-resolution ice sheet models, become obsolete at such high resolution.

The Antarctic ice sheet responds on timescales that are longer than those of climate variability. As it is thus never in equilibrium, the ice-sheet model component requires a high-resolution spin-up procedure that provides a realistic configuration of the present-day Antarctic Ice Sheet and at the same time accounts for the long-term drift as a delayed response to the climate conditions during the last glacial cycles. The distributed architecture of the RAnGO coupling interface allows us to perform spin-up and coupled integration of the ice sheet model on the same server (not at HLRN), thus avoiding unnecessary porting of the PISM code, and at the same time benefit from the very robust and computationally efficient FESOM installation at HLRN.

At the time of writing this report, the coupled model has completed a 250-year control simulation with 20th century climate. A future projection by the coupled model has proceeded until the second half of the 22nd century. Compared to the 10 km resolution used in the ice sheet component of RAnGO, year-to-year fluctuations of the grounding-line position are smaller in FESOM-PISM. A tendency towards advancing grounding lines for 20th-century climate (Fig. 1) may indicate an underestimation of basal melt in the immediate vicinity of the grounding line. We are currently looking into the governing processes here.

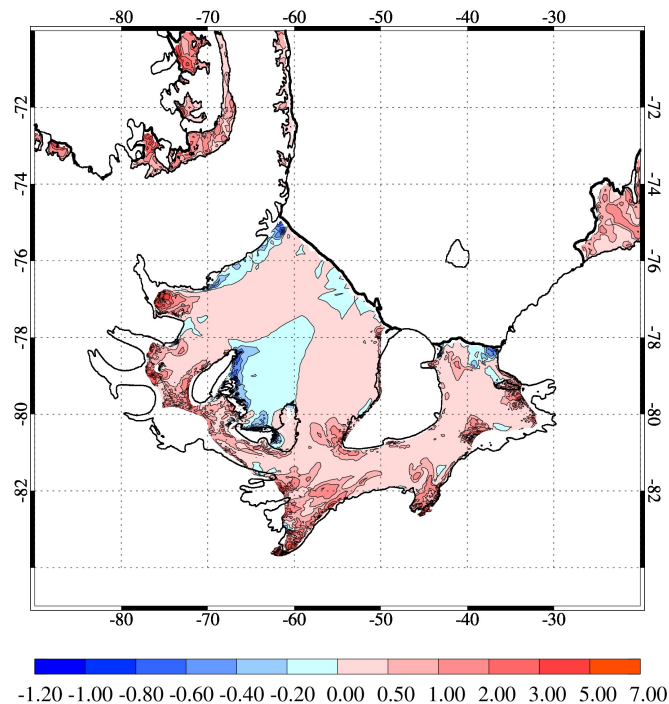


Figure 1: Annual-mean basal melt rates (m/yr) for Filchner Ronne Ice Shelf simulated with the coupled FESOM-PISM model after 40 years of coupled integration. Note the nonlinear color scale. The coloured area represents the modelled cavity geometry. Black lines denote coast and grounding lines from RTopo-2.

Similar to previous studies with uncoupled ocean-ice shelf models (e.g. Timmermann and Hellmer, 2013) and with the coupled RAnGO model (Timmermann and Goeller, 2017), a regime shift from cold to warm water on the continental shelf off Filchner-Ronne Ice Shelf leads to a substantial increase of ice shelf basal melt rates towards the end of the 21st century (Fig. 2, top).

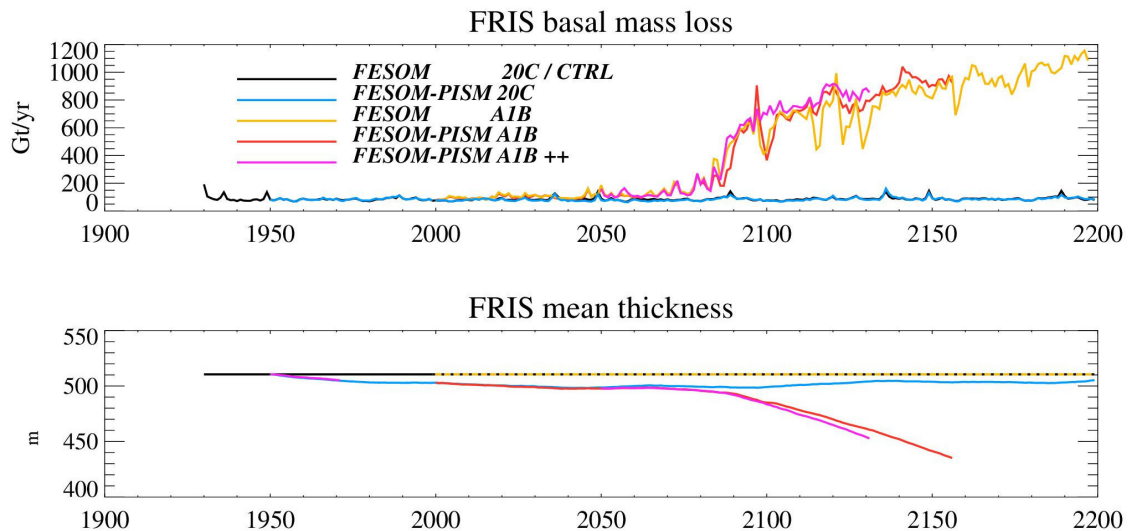


Figure 2: top: Simulated basal melt rates for Filchner Ronne Ice Shelf in uncoupled FESOM experiments (black and yellow lines) and with the coupled FESOM-PISM model (blue and red/magenta lines). bottom: Mean thickness of FRIS in the coupled control experiment with 20th-century climate (blue line) and the coupled model projection for the A1B scenario (red and magenta lines). The magenta line indicates results from a sensitivity study with free-slip boundary conditions at the FESOM grounding lines.

In the FESOM-PISM coupled model projection, this leads to a thinning of FRIS by an average number of about 10 % between 2100 and 2150 (Fig. 2, bottom). Reduced buttressing by thinner ice causes an increasing discharge of grounded ice into the ocean. The difference between the A1B projection (FESOM-PISM A1B) and the control run (FESOM-PISM 20C) amounts to an additional 20 mm of sea level rise.

References

- Timmermann, R., Q. Wang, and H.H. Hellmer (2012): Ice shelf basal melting in a global finite-element sea ice–ice shelf–ocean model, *Annals of Glaciology*, 53(60), 303-314, doi:10.3189/2012AoG60A156.
- Timmermann, R. and H.H. Hellmer (2013): Southern Ocean warming and increased ice shelf basal melting in the twenty-first and twenty-second centuries based on coupled ice-ocean finite-element modelling. *Ocean Dyn.* 63, 1011–1026.
- Timmermann, R. and Goeller, S. (2017): Response to Filchner–Ronne Ice Shelf cavity warming in a coupled ocean–ice sheet model – Part 1: The ocean perspective, *Ocean Sci.*, 13, 765-776, <https://doi.org/10.5194/os-13-765-2017>.

Publications

1. Mueller, R.D. and R. Timmermann: Weddell Sea Circulation. In: J. Cochran, H. Bokuniewicz and P. Yager (editors), *Encyclopedia of Ocean Sciences 3rd Edition*, Cambridge MA, Academic Press, 7 p., ISBN: 9780128130827, doi: 10.1016/B978-0-12-409548-9.11631-8, 2019.
2. Schnaase, F. and Timmermann, R.: Representation of shallow grounding zones in an ice shelf-ocean model with terrain-following coordinates, *Ocean Modelling*, 144, doi: 10.1016/j.ocemod.2019.101487, 2019.

Presentations

1. Timmermann, R. and T. Albrecht: Coupled ocean–ice simulation of the Weddell Sea basin. *Forum for Research into Ice Shelf Processes*, Oxford, 15.-18.09.2019.

6.13 **hbk00038: Interaction between marine terminating glaciers and the ocean circulation in Northeast Greenland**

| | |
|---------------------|--|
| HLRNProject ID: | hbk00038 |
| Run time: | IV/2019 – III/2020 |
| Project Leader: | Prof. Dr. Torsten Kanzow |
| Project Scientists: | Dr. Ralph Timmermann und Dr. Claudia Wekerle |
| Affiliation: | Alfred Wegener Institute |

Introduction

The Greenland ice sheet has been subject to strong mass loss in the last decades (Bamber et al., 2018). Greenland freshwater fluxes have implications for the global sea level (Chen et al., 2017), and can affect the strength of the Atlantic Meridional Circulation (Böning et al., 2016). Anomalously high transport of Atlantic Water through the Nordic Seas was observed in the last decades (Beszczynska-Möller et al., 2012), and is thought to increase melting of marine terminating glaciers around Greenland (Rignot et al., 2012).

Future projections of climate warming around Greenland indicate particularly large melting rates on the east coast of Greenland, between Fram Strait and Denmark Strait (Lique et al., 2015). In Northeast Greenland, the Zachariae Isstrom lost its entire floating ice tongue between 2012 and 2014 (Mouginot et al., 2015). A warming in Atlantic Water temperatures has been suggested to be the main driver for the collapse of the ice tongue (Khan et al., 2014; Mouginot et al., 2015). Both Zachariae Isstrom and the 79 North Glacier (79NG) drain the Northeast Greenland Ice Stream. High resolution modeling studies of the Northeast Greenland glaciers which allow to investigate local processes at the glacier fronts are however still missing. Warm Atlantic Water (AW) has to pass through the trough system of the Northeast Greenland continental shelf to reach the glacier fronts. Schaffer et al. (2017) showed, based on observations from 1979-2016, that warm Atlantic Intermediate Water mainly reaches the 79NG via the southern trough, i.e. the Norske Trough. However, the observational data used by Schaffer et al. (2017) mainly covers the summer season. Long-term high-resolution model integrations will help to fill the gap.

Some of the important scientific questions that we are investigating in our project are listed below:

- (1) How does the warm Atlantic Water interact with the glaciers? Through which pathways does it reach them?
- (2) How is Atlantic Water transported onto the Northeast Greenland continental shelf into the troughs? Is meso-scale eddy activity in the EGC an important process in bringing the Atlantic Water onto the shelf? The role of eddies is still unclear.
- (3) How do recent changes occurring in the Arctic Ocean and Nordic Seas (sea ice decline and increased Atlantic Water transport) impact the glaciers?

Methods

In our study, we apply a global version of the Finite-Element-Sea ice-Ocean Model 1.4 (FESOM1.4, Wang et al. 2014). It consists of a finite element ocean model, coupled to a dynamic-thermodynamic finite element sea ice model. FESOM is based on unstructured triangular meshes in the horizontal, and tetrahedral elements in the volume.

An eddy-resolving simulation with focus on the Fram Strait and the Northeast Greenland continental shelf has been carried out for the time period 2000-2009 using CORE2 atmospheric forcing (Wekerle et al. 2017), and extended for the time period 2010-2016 using ERA interim forcing. The mesh resolution is up to 1 km in our area of interest. A comparison with observational data in the Fram Strait (hydrography and velocity measured by a mooring array in Fram Strait) showed that the model performs well in reproducing circulation structure, eddy kinetic energy and hydrography (Wekerle et al. 2017).

Results

Model assessment: sea level variability

We analyzed sea level variability in the northern Greenland Sea by comparing our high-resolution simulation with satellite altimetric data from Envisat (Müller et al. 2019a). The altimetry observations, particularly in the western part of Fram Strait and on the Greenland continental shelf, are characterized by irregular sampling and by sea-ice coverage, complicating reliable sea level estimations. In order to overcome this difficulty, a classification was performed to detect small open water gaps within the sea ice covered region. On the Northeast Greenland continental shelf (defined as the region between 72°N and 81.5°N and shallower than 450 m), there is a relatively high correlation in residual sea level variability (after removing constant offsets and the annual cycle) between altimetry and FESOM ($r=0.67$). The correlation is slightly smaller than for the mostly ice-free central Fram Strait ($r=0.81$) and Barents Sea ($r=0.75$), indicating that the treatment of altimetric data below sea ice is complicated, and that there is still need to improve the sea ice-ocean model. Nonetheless, the relatively well agreement between FESOM and altimetry led to the development of a combined sea surface height data product (Müller et al. 2019b).

Atlantic Water layer

For our study, the structure of the Atlantic Water layer is of particular importance since a trough system on the Northeast Greenland continental shelf carries warm Atlantic Water from the shelf break towards the marine-terminating outlet glaciers draining the Northeast Greenland Ice Stream. Consistent with observations by Schaffer et al. (2017), our simulation shows that warm Atlantic Water enters the shelf mainly through the southern trough, Norske Trough (Figure 1).

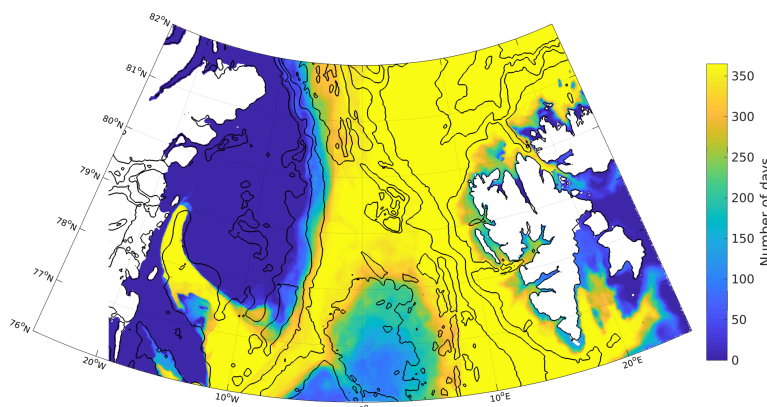


Figure 1: Number of days in 2009 where Atlantic Water (AW, defined as $T > 2^\circ\text{C}$) is present in the water column. On the Greenland continental shelf, AW is present in the Norske Trough, but not in the Westwind Trough.

The role of eddies for the AW recirculation

The northeast Greenland glaciers are strongly influenced by Atlantic Water that recirculated in the Fram Strait. The oceanic conditions there are strongly turbulent, and it was shown before that eddies play an important role in the recirculation (e.g. Hattermann et al. 2016). In a study

submitted to *Ocean Science* we investigated eddy properties and dynamics in the Fram Strait simulated in two high-resolution models, ROMS and FESOM (Wekerle et al., submitted). In both models, the relative vorticity field exhibits strong eddy activity, particularly along the pathway of the main currents, WSC and EGC, along the Yermak and Svalbard branches and in the AW recirculation area (Figure 2). Apart from well defined eddies, the relative vorticity fields show lots of elongated filamentary structures. Eddies are more abundant in the eastern part of Fram Strait than in the western part. On the northeast Greenland continental shelf, eddy density is rather low.

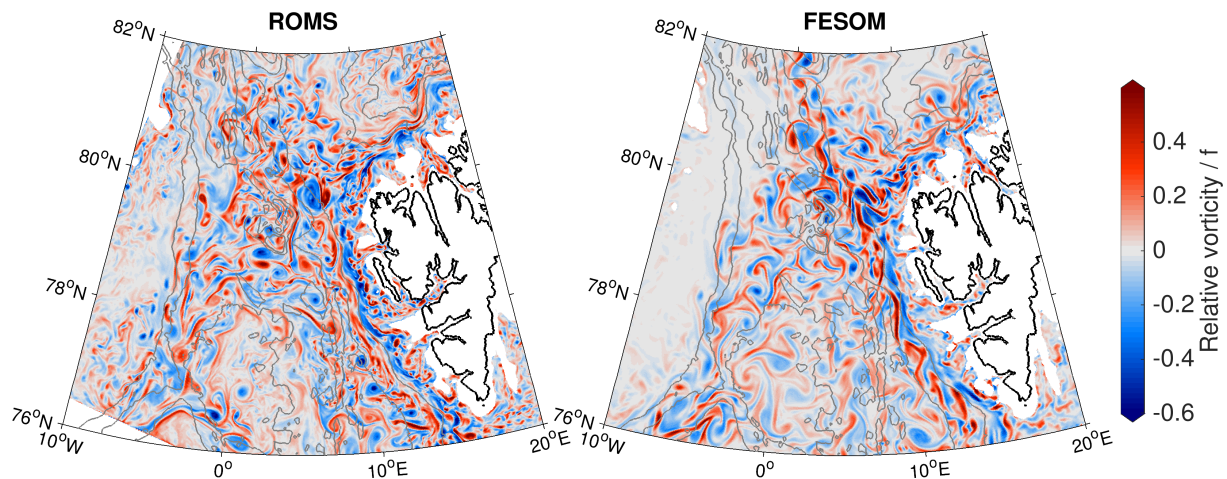


Figure 2: Snapshots of relative vorticity divided by the Coriolis parameter f in 100 m depth in simulations with ocean models ROMS and FESOM.

Impact of Arctic Ocean sea ice decline

A recent study by Wang et al. (2020) showed that sea ice decline leads to an intensification of Atlantic Water transport through the Fram Strait. In particular, the reduction in sea ice export through Fram Strait induced by Arctic sea ice decline increases the salinity in the Greenland Sea, which lowers the sea surface height and strengthens the cyclonic gyre circulation in the Nordic Seas. This possibly also leads to increased supply of warm AW to the northeast Greenland glaciers.

Outlook

At the moment, we conduct simulations with a FESOM configuration that comprises the ice shelf component described by Timmermann et al. (2013). Furthermore, we plan to conduct coupled ocean-ice shelf simulations in the future.

Publications

- Müller, F. L., Wekerle, C., Dettmering, D., Passaro, M., Bosch, W., and Seitz, F.: Dynamic ocean topography of the northern Nordic seas: a comparison between satellite altimetry and ocean modeling, *The Cryosphere*, 13, 611-626, doi.org/10.5194/tc-13-611-2019, 2019a.
- Müller, F. L., Dettmering, D., Wekerle, C., Schwatke, C., Passaro, M., Bosch, W., and Seitz, F.: Geostrophic currents in the northern Nordic Seas from a combination of multi-mission satellite altimetry and ocean modeling, *Earth Syst. Sci. Data*, 11, 1765–1781, doi.org/10.5194/essd-11-1765-2019, 2019b.

Wang, Q., Wekerle, C., Wang, X., Danilov, S., Koldunov, N., Sein, D., et al: Intensification of the Atlantic Water supply to the Arctic Ocean through Fram Strait induced by Arctic sea ice decline. *Geophysical Research Letters*, 47, doi.org/10.1029/2019GL086682, 2020.

Wekerle, C., Hattermann, T., Wang, Q., Crews, L., von Appen, W.-J., and Danilov, S.: Properties and dynamics of mesoscale-eddies in the Fram Strait from a comparison between two high-resolution ocean-sea ice models, submitted to *Ocean Science*.

References

Bamber, J. L., A. J. Tedstone, M. D. King, I. M. Howat, E. M. Enderlin, M. R. van den Broeke, and B. Noel (2018), Land Ice Freshwater Budget of the Arctic and North Atlantic Oceans: 1. Data, Methods, and Results, *Journal of Geophysical Research: Oceans*, 123 (3), 1827-1837.

Beszczynska-Möller, A., E. Fahrbach, U. Schauer, and E. Hansen (2012), Variability in Atlantic water temperature and transport at the entrance to the Arctic Ocean, 1997-2010, *ICES J. Mar. Sci.*, 69, 852-863.

Böning, C. W., E. Behrens, A. Biastoch, K. Getzlaff, and J. L. Bamber (2016), Emerging impact of Greenland meltwater on deepwater formation in the North Atlantic Ocean, *Nature Geosci.*, 9, 523-527.

Chen, X., X. Zhang, J. A. Church, C. S. Watson, M. A. King, D. Monselesan, B. Legresy, and C. Harig (2017), The increasing rate of global mean sea-level rise during 1993-2014, *Nature Clim. Change*, 7, 492-495.

Hattermann, T., Isachsen, P. E., von Appen, W.-J., Albretsen, J., and Sundfjord, A. (2016), Eddy-driven recirculation of Atlantic Water in Fram Strait, *Geophys. Res. Lett.*, 43.

Khan, S. A., et al. (2014), Sustained mass loss of the northeast Greenland ice sheet triggered by regional warming, *Nature Clim. Change*, 4, 292-299.

Lique, C., H. L. Johnson, Y. Plancherel, and R. Flanders (2015), Ocean change around Greenland under a warming climate, *Clim. Dyn.*, 45, 1235-1252.

Mouginot, J., E. Rignot, B. Scheuchl, I. Fenty, A. Khazendar, M. Morlighem, A. Buzzi, and J. Paden (2015), Fast retreat of Zachariae Isstrom, northeast Greenland, *Science*.

Münchow, A., J. Schaffer, and T. Kanzow (2020): Ocean Circulation Connecting Fram Strait to Glaciers off Northeast Greenland: Mean Flows, Topographic Rossby Waves, and Their Forcing. *J. Phys. Oceanogr.*, 50, 509–530.

Rignot, E., I. Fenfy, D. Menemenlis, and Y. Xu (2012), Spreading of warm ocean waters around Greenland as a possible cause for glacier acceleration, *Annals of Glaciology*, 53 (60).

Schaffer, J., W.-J. von Appen, P. A. Dodd, C. Hofstede, C. Mayer, L. de Steur, and T. Kanzow (2017), Warm water pathways toward Nioghalvfjærdsfjorden Glacier, Northeast Greenland, *J. Geophys. Res. Oceans*, 122 (5), 4004-4020.

Timmermann, R., and H. H. Hellmer (2013), Southern Ocean warming and increased ice shelf basal melting in the twenty-first and twenty-second centuries based on coupled ice-ocean finite-element modelling, *Ocean Dynamics*, 63 (9), 1011-1026.

Wang, Q., S. Danilov, D. Sidorenko, R. Timmermann, C. Wekerle, X. Wang, T. Jung, and J. Schröter (2014), The Finite Element Sea Ice-Ocean Model (FESOM) v.1.4: formulation of an ocean general circulation model, *Geosci. Model Dev.*, 7, 663-693.

Wekerle, C., Q. Wang, W.-J. von Appen, S. Danilov, V. Schourup-Kristensen, and T. Jung (2017), Eddy-resolving simulation of the Atlantic Water circulation in the Fram Strait with focus on the seasonal cycle, *J. Geophys. Res. Oceans*, 122, 8385–8405.

6.14 *hbk00055*: Investigating the biogeochemistry of the high latitudes during the period of rapid change: modelling and satellite retrievals

| | |
|---------------------|--|
| HLRNProject ID: | hbk00055 |
| Run time: | IV/2017 – III/2019 |
| Project Leader: | Prof. Dr. A Bracher ^{1,2} |
| Project Scientists: | S. Losa ¹ , V. Pefanis ¹ , J. Oelker ² , M. A. Soppa ¹ , M. Losch ¹ |
| Affiliation: | ¹ Alfred Wegener Institute Helmholtz Centre for Polar and Marine Research, Bremerhaven ² University of Bremen |

Overview

The aim of the computing project is to obtain long-term time series of ocean biogeochemical model simulations and satellite retrievals to analyse the changes in biodiversity and biogeochemical cycling observed over the last years in the Polar regions (the Southern and Arctic Oceans) and to improve our understanding of possible interactions between the open water, sea ice, snow, ocean biogeochemistry and ecosystem and chemical composition of the Atmospheric Boundary Layer under the recently observed climate changes. Within the HLRN project, the coloured dissolved organic matter (CDOM) and phytoplankton distribution as well as phytoplankton diversity in response to Arctic Amplification are simulated with the biogeochemical model Darwin (Dutkiewicz et al., 2015) coupled to the Massachusetts Institute of Technology General Circulation Model (MITgcm, MITgcm Group, 2012). The study relates to the DFG project “**Artic**Amplification: **C**limate Relevant **A**tmospheric and **S**urfa**C**e Processes, and **F**eedback Mechanisms (**AC**)³” within the establishment of Transregional Collaborative Research Centre TR 172 and is partly conducted in the frame of the Helmholtz Climate Initiative **REKLIM** (Regional Climate Change), a joint research project of the Helmholtz Association of German Research Centres (HGF). In support to the DFG research “**PhySyn**” within the framework of the DFG-Priority Program 1158 “Antarctic Research” we simulate phenology and time series of the dominant phytoplankton functional types (PFTs) in the Southern Ocean (including the Great Calcite Belt).

Results

Within this computing project, a version of the Darwin-MITgcm was adjusted to simulate composition, dominance and phenology of the key phytoplankton types (PFTs) observed (by satellite and in situ) in the Southern Ocean (Soppa et al., 2016, Smith et al. 2017, Soppa et al., 2017). The obtained results of the model adjustment and sensitivity studies allow us to hypothesize on biological factors controlling the observed Southern Ocean PFT biogeography: for instance, the high affinity of coccolithophores to nutrients, its low palatability for grazers, *Phaeocystis* sp. morphological shift, size diversity within diatoms (Losa et al. 2019).

To investigate possible bio-physical interactions in the Arctic Ocean (etc. radiative heating due to CDOM absorption and phytoplankton attenuation, Soppa et al. 2019), in the MITgcm ocean physics and sea ice modules we explicitly introduced a dependence of the penetrated shortwave radiation on the prognostic phytoplankton chlorophyll concentration and CDOM absorption. We compared coupled model simulations with the explicit formulation of the biogeochemical feedback to the ocean and sea-ice against model outputs obtained with Jerlov’s approximation of the light vertical path. In comparison with the reference (Jerlov), the

simulations with the explicit biogeochemical feedback reveal 0.25°C higher summer sea surface temperature (SST) with 46% of this difference explained by CDOM absorption, which in turns led to the summer sea ice extent decreased. Differences in the SST annual range and days with sea ice concentration (SIC) more than 15% are depicted in Figure 2. In these simulations, however, we did not account for CDOM loading by the rivers and thawing permafrost.

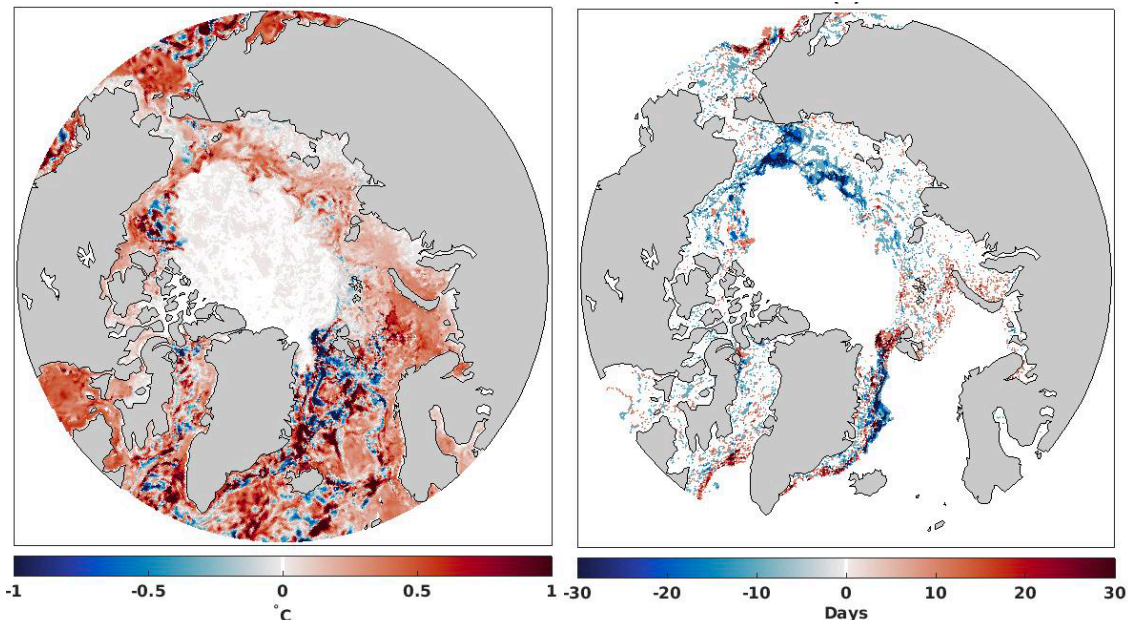


Figure 2: Difference in SST annual range (a) and in days with more than 15% SIC (b) between the model simulations with and without accounting for biogeochemical feedback for the year 2012.

Outlook

A precise evaluation of the Arctic PFT and CDOM model results is to be performed with available *in situ* observations (Gonçalves-Araujo et al., 2015, 2016, Liu et al. 2018, 2019). Further investigations are required with respect to possible impacts of the terrestrial CDOM and feedbacks to the surface biogeochemistry and phytoplankton composition.

Publications

1. Losa, S. N., Dutkiewicz, S., Losch, M., Oelker, J., Soppa, M., Trimborn, S., Xi, H., Bracher, A. (2019): On the modelling the Southern Ocean Phytoplankton Functional Types, *Biogeoscience Discussions*, doi:10.5194/bg-2019-289.

Presentations

1. Losa, S. N., Pefanis, V., Soppa, M. A., Oelker, J., Losch, M., Xi, H., Trimborn, S., Dutkiewicz, S., Rozanov, V. V., Richter, A., Burrows, J. P. and Bracher, A. (2019): Recent advances in ocean biogeochemical modelling: towards synergy between models and *in situ* and satellite observations, AWI-IUP joint seminar, AWI, Bremerhaven, 24 June 2019. (Oral presentation)
2. Pefanis, V., Losa, S. N., Soppa, M. A., Losch, M., Heim, B., Dutkiewicz, S., Rozanov, V. V. and Bracher, A. (2019): Modelling the Arctic Ocean bio-physical feedbacks: impact of biogeochemistry on ocean hydrography and sea ice. REKLIM, Workshop, Herrsching am Ammersee (Germany), 6 May 2019 – 8 May 2019. (Poster)

3. Pefanis, V., Losa, S. N., Soppa, M. A., Losch, M., Dutkiewicz, S., Janout, M., Rozanov, V. V. and Bracher, A. (2019): Assessing bio-physical feedbacks in the Arctic Ocean under Arctic amplification, EGU General Assembly 2019, Vienna, Austria, 7 April 2019 – 12 April 2019. (Oral presentation).

References

1. Dutkiewicz, S., Hickman, A. E., Jahn, O., Gregg, W. W., C. B. Mouw, C. B., and M. J. Follows (2015) Capturing optically important constituents and properties in a marine biogeochemical and ecosystem model, *Biogeosciences*, 12, 4447–4481.
2. Gonçalves-Araujo, R., Stedmon, C. A., Heim, B., Dubinenkov, I., Kraberg, A., Moiseev, D. and Bracher, A. (2015) From Fresh to Marine Waters: Characterization and Fate of Dissolved Organic Matter in the Lena River Delta Region, Siberia, *Front. Mar. Sci.*, 2, 108, doi:10.3389/fmars.2015.00108.
3. Gonçalves-Araujo, R., Granskog, M. A., Bracher, A., Azetsu-Scott, K., Dodd, P. A. and Stedmon, C. A. (2016) Using fluorescent dissolved organic matter to trace and distinguish the origin of Arctic surface waters, *Sci. Rep.*, 6, 33978, doi:10.1038/srep33978.
4. Liu, Y., Boss, E., Chase, A., Xi, H., Zhang, X., Röttgers, R., Pan, Y. and Bracher, A. (2019): Retrieval of Phytoplankton Pigments from Underway Spectrophotometry in the Fram Strait, *Remote Sensing*. doi:10.3390/rs11030318.
5. Liu, Y., Röttgers, R., Ramírez-Pérez, M., Dinter, T., Steinmetz, F., Nöthig, E. M., Hellmann, S., Wiegmann, S. and Bracher, A. (2018): Underway spectrophotometry in the Fram Strait (European Arctic Ocean): a highly resolved chlorophyll a data source for complementing satellite ocean color, *Optics Express*. doi:10.1364/OE.26.00A678.
6. Losa, S. N., Oelker, J., Soppa, M. A., Dutkiewicz, S., Losch, M., Dinter, T., Rozanov, V. V., Richter, A., Burrows, J. P. and A. Bracher, Investigating the phytoplankton diversity in the great calcite belt: perspectives from hyper- and multispectral satellite retrievals and numerical modelling. Extended Abstract of the XXIV Ocean Optics, Dubrovnik, Croatia (2018); https://oceanopticsconference.org/extended/Losa_Svetlana.pdf
7. MITgcm Group (2012), MITgcm Manual, Online documentation, MIT/EAPS, Cambridge, MA 02139, USA.
8. Smith et al. (2017) The influence of the environmental variability on the biogeography of coccolithophores and diatoms in the Great Calcite Belt, *Biogeosciences*, 14, 4905–4925 and diatoms in the Great Calcite Belt, *Biogeosciences*, 14, 4905–4925.
9. Soppa, M. A., Pefanis, V., Hellmann, S., Losa, S. N., Hölemann, J., Martynov, F., Heim, B., Janout, M. A., Dinter, T., Rozanov, V., Bracher, A. (2019). Assessing the Influence of Water Constituents on the Radiative Heating of the Laptev Sea Shelf Waters, *Frontiers in Marine Science*, 6: 221.
10. Soppa, M. A., Peeken, I., and Bracher, A. (2017). Global chlorophyll “a” concentrations for diatoms, haptophytes and prokaryotes obtained with the Diagnostic Pigment Analysis of HPLC data compiled from several databases and individual cruises. doi:10.1594/PANGAEA.875879.
11. Soppa, M., Völker, C. and Bracher, A. (2016): Diatom Phenology in the Southern Ocean: Mean Patterns, Trends and the Role of Climate Oscillations, *Remote Sensing*, 8 (420), pp. 1–17.

6.15 *hbk00057*: Persistent ozone depletion in the tropical stratosphere: identifying possible reasons

| | |
|---------------------|--|
| HLRN Project ID: | hbk00057 |
| Run time: | I/2017 – II/2020 |
| Project Leader: | Dr. Alexei Rozanov |
| Project Scientists: | Dr. Evgenia Galytska |
| Affiliation: | Institute of Environmental Physics, University of Bremen |

Overview

Playing a key role in the radiative budget of the Earth's atmosphere stratospheric ozone also protects the biosphere from the harmful UV radiation and is closely related to stratospheric circulation and meteorology. After the anthropogenic emission of the ozone depleting species has been ruled out by Montreal Protocol and its amendments the severe ozone decline discovered in early eighties of the last century began to slow down and even some indications of the ozone recovery have been inferred from observations (Newchurch et al., 2003, WMO, 2007, 2011, Yang et al., 2006). During the last decade the vertical distribution of stratospheric ozone trends has been moved into the focus (Eckert et al., 2014, Gebhardt et al., 2014, Kyrola et al., 2013). Analyzing the vertically resolved time series of ozone in the tropics during the first decade of the XXI century all authors agree in their conclusions that a strong ozone recovery was seen in the middle to lower stratosphere (below about 30 km) while a significant ozone depletion was observed at altitudes of about 35 km. Being vertically integrated these opposite trends result in a slightly positive change which is consistent with the signatures of a recovery seen in the observations of the ozone total column.

In this study we focused at the investigation of vertical distributions of NO_2 and BrO retrieved from limb measurements from the SCIAMACHY (SCanning Imaging Absorption spectroMeter for Atmospheric CHartograohY) instrument (Bovensmann et al., 1999) onboard the ESA Envisat satellite. The main objective of this study was to assess if the behavior of NO_2 is consistent with the findings of Nedoluha et al. (2015) with respect to the NO_y family and if halogen species might have a significant contribution to the ozone depletion mechanisms in this latitude/altitude region. The investigation includes modeling studies using the Chemical Transport Model (CTM) TOMCAT (Chipperfield et al., 2006) to evaluate if the observed behavior of the species can be reproduced by the model and if the observed trends in the tropical stratospheric ozone can be explained by the observed trends in both NO_2 and BrO. A consideration of BrO is believed to be important as on the one hand it is an ozone depleting species and on the other hand it reacts with nitrogen species to form inactive reservoir species.

Results

While the anticorrelated linear changes of ozone and NO_2 inferred in the framework of this study are consistent with those reported by Nedoluha et al. (2015), the linear changes in the age of air showed no indication for a slowdown in the upwelling speed as suggested by Nedoluha et al. (2015) to explain the observed positive trends of NO_2 . However, when analyzing the age of air resolved by seasons, it was found that the circulation speeds up during the boreal winter while slowing down during the boreal autumn. These trends, however, cancel out when considering the whole year. With the increasing circulation speed, the amount of

N_2O , which is a precursor of NO_2 , increases resulting in the increase of NO_2 and the decrease of ozone (and vice versa). As the amount of N_2O is controlled by both the transport from the troposphere and photochemical destruction its variations are not canceled out when considering the whole year.

Figure 1 shows the linear changes of ozone, NO_2 and age of air for December-January-February (DJF) and September-October-November (SON) seasons from TOMCAT model. It is seen that the accelerating upwelling during the boreal autumn causes a strong increase in the NO_2 amount and the decrease in the ozone. For DJF season the opposite behavior is observed. Thus it was concluded that the observed trends are caused by the seasonal variations in the change of the circulation speed.

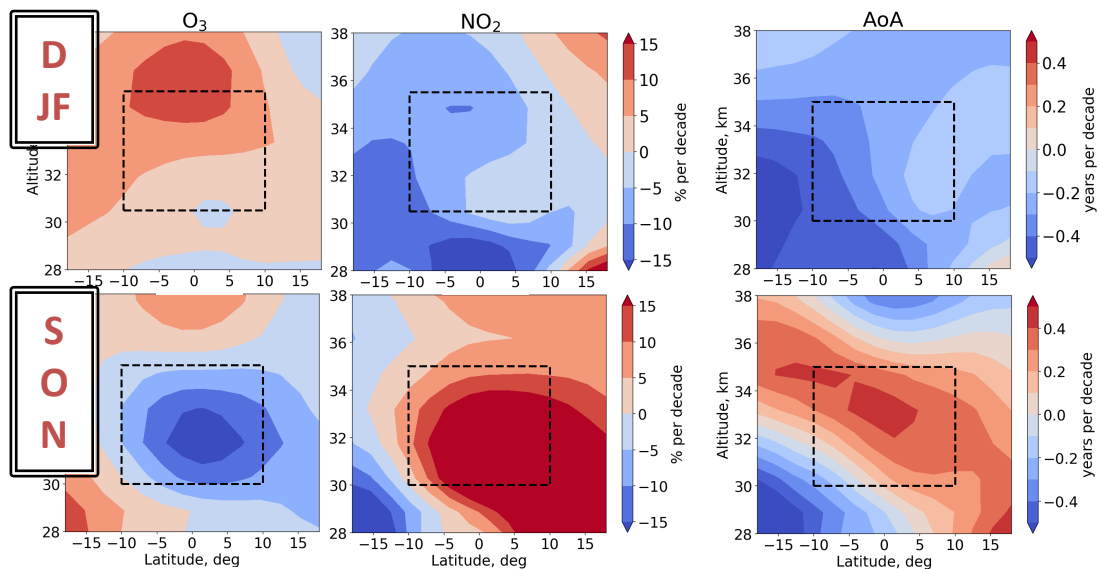


Figure 3: Linear changes of ozone, NO_2 and age of air for December-January-February (DJF) and September-October-November (SON) seasons from TOMCAT model.

With respect to BrO data set an unexpected result was obtained which contradicted the model simulations and results from SCIAMACHY nadir observations, see Fig. 2. The trends in the stratospheric BrO were found to be positive while negative trends are expected as a result of the restrictions applied to the emission of the halogenated species by the Montreal protocol and its amendments. Since both modeling results for the stratosphere and the retrieval results for the total column of BrO show negative trends, the probability of a retrieval artifact in the SCIAMACHY limb BrO was rated as very high. As no technical issues related to the instrument were identified so far, the cause of the observed behavior was suspected to be a correlation between the retrieval parameters or unexpected influence of a change of atmospheric parameters, other than BrO, on the retrieval results.

To identify the reasons for the observed retrieval artifacts the sensitivity of the resulting time series to the retrieval parameters was investigated. While no significant influence was found for most of the settings, the order of the polynomial, which is subtracted from the spectral data, was found to be the most crucial parameter. Figure 3 depicts the SCIAMACHY BrO time series obtained with different parameter settings. The retrieval runs V4.2 and V4.3 shown in the plot by green and orange lines, respectively, differ mainly by using a quadratic instead of linear polynomial. It is clearly seen that V4.3 run lies much closer to the model curve and do not show the unrealistic increase of BrO with the time. As a further step, V4.4 run was done by applying a third order polynomial. In addition no correction for a wavelength independent offset of the spectra and no squeeze correction when adjusting the wavelength calibration were done. The

resulting time series shown by the blue line in Fig. 3 agrees better with the model one for tropics, looks quite similar to V4.3 run in the northern mid-latitudes but shows quite different seasonal behavior at southern mid-latitudes. Further investigations are needed to analyze different parameter settings and make a decision which parameter set is optimal for SCIAMACHY BrO retrieval.

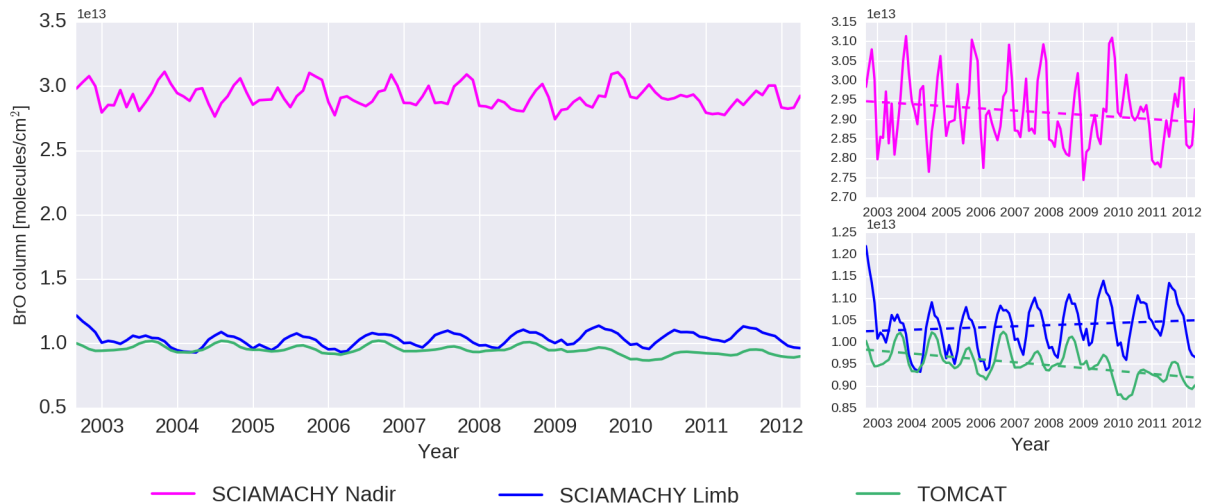


Figure 4. BrO stratospheric column obtained from SCIAMACHY limb observations and TOMCAT model simulations as well as BrO total column from SCIAMACHY nadir observations.

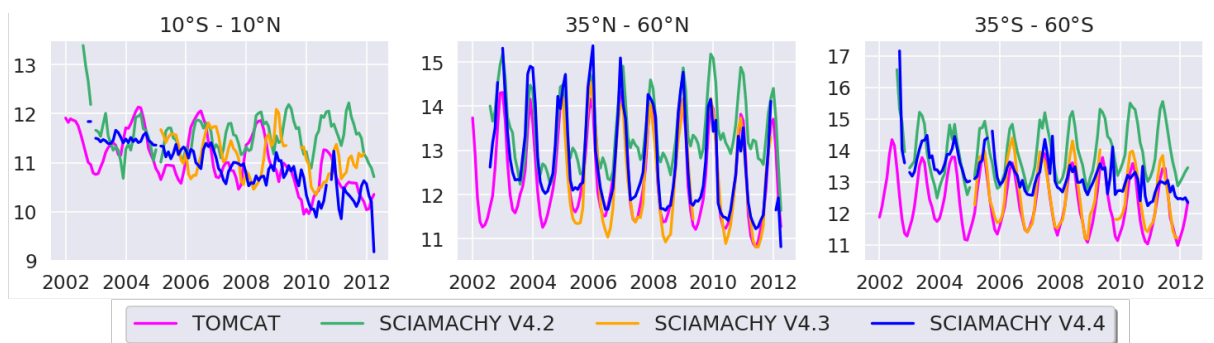


Figure 5. BrO volume mixing ratio (pptV) at 20 km at different latitudes from TOMCAT model and different SCIAMACHY retrievals.

Outlook

Further investigations are needed to make a decision on the optimal retrieval parameter set. After all data are processed with the selected retrieval parameters, BrO linear changes for SCIAMACHY operational period need to be calculated and compared to the model data.

PhD Thesis

1. Galytska, E., Spatio-temporal variations of observed and modelled stratospheric trace gases, Universität Bremen, <http://nbn-resolving.de/urn:nbn:de:gbv:46-00107599-10>, 2019

Publications

1. Galytska, E., Rozanov, A., Chipperfield, M. P., Dhomse, S. S., Weber, M., Arosio, C., Feng, W., and Burrows, J. P.: Dynamically controlled ozone decline in the tropical mid-stratosphere observed by SCIAMACHY, *Atmos. Chem. Phys.*, 19,767-783, <https://doi.org/10.5194/acp-19-767-2019>, 2019.

Presentations

1. Galytska, E., Rozanov, A., Chipperfield, M. P., Dhomse, S. S., Weber, M., Noël, S., Bourassa, A., Degenstein, D., Damadeo, R., Burrows, J. P.: Validation of SCIAMACHY limb NO₂ scientific data V4.0, its changes in the stratosphere and their impact on O₃ chemistry in the tropical region. 10th International Limb Workshop, Greifswald, Germany, 4-7 June 2019.
2. Galytska, E., Rozanov, A., Chipperfield, M. P., Arosio, C., Dhomse, S. S., and Burrows, J. P.: Ozone decline in the tropical mid-stratosphere observed by SCIA-MACHY and its relation to the stratospheric dynamics. IUP/AWI Block Seminar, 04.02.2019, Bremen, Germany.
3. Galytska, E., Arosio, C., Rozanov, A., Chipperfield, M. P., Dhomse, S. S., Sofieva, V., and Burrows, J. P.: Seasonal variability in transport in the tropical mid-stratosphere and its impact on ozone and key trace gases. European Geosciences Union General Assembly 2019, 7-12.04.2019, Vienna, Austria.

References

1. Eckert, E., von Clarmann, T., Kiefer, M., Stiller, G. P., Lossow, S., Glatthor, N., Degenstein, D. A., Froidevaux, L., Godin-Beekmann, S., Leblanc, T., McDermid, S., Pastel, M., Steinbrecht, W., Swart, D. P. J., Walker, K. A., and Bernath, P. F.: Drift-corrected trends and periodic variations in MIPAS IMK/IAA ozone measurements, *Atmos. Chem. Phys.*, 14, 2571-2589, 2014.
2. Gebhardt, C., Rozanov, A., Hommel, R., Weber, M., Bovensmann, H., Burrows, J. P., Degenstein, D., Froidevaux, L., and Thompson, A. M.: Stratospheric ozone trends and variability as seen by SCIAMACHY from 2002 to 2012, *Atmos. Chem. Phys.*, 14, 831-846, doi:10.5194/acp-14-831-2014, 2014.
3. Galytska, E., Rozanov, A., Chipperfield, M. P., Dhomse, Sandip, S., Weber, M., Arosio, C., Feng, W., and Burrows, J. P.: Dynamically controlled ozone decline in the tropical mid-stratosphere observed by SCIAMACHY, *Atmos. Chem. Phys.*, 19, 767-783, <https://doi.org/10.5194/acp-19-767-2019>, 2019.
4. Kyrölä, E., Laine, M., Soeva, V., Tamminen, J., Paivarinta, S.-M., Tukiainen, S., Zawodny, J., and Thomason, L.: Combined SAGE II-GOMOS ozone profile data set for 1984-2011 and trend analysis of the vertical distribution of ozone, *Atmos. Chem. Phys.*, 13, 10645-10658, doi:10.5194/acp-13-10645-2013, 2013.
5. Nedoluha, G. E., D. E. Siskind, A. Lambert, and C. Boone, The decrease in mid-stratospheric tropical ozone since 1991, *Atmos. Chem. Phys.*, 15, 4215-4224, doi:10.5194/acp-15-4215-2015, 2015.
6. Newchurch, M. J., Yang, E.-S., Cunnold, D. M., Reinsel, G. C., Zawodny, J. M., and Russell III, J. M.: Evidence for slowdown in stratospheric ozone loss: First stage of ozone recovery, *J. Geophys. Res.*, 108, 4507, doi:10.1029/2003JD003471, 2003.
7. WMO: Scientific Assessment of Ozone Depletion: 2006, Global Ozone Research and Monitoring Project Report 50, World Meteorological Organization, Geneva, www.wmo.int/pages/prog/arep/gaw/ozone2006/ozoneasstreport.html, 2007.
8. WMO: Scientific Assessment of Ozone Depletion: 2010, Global Ozone Research and Monitoring Project Report 52, World Meteorological Organization, Geneva, www.unep.ch/ozone/AssessmentPanels/SAP/ScientificAssessment2010/00-SAP-2010-Assement-report.pdf, 2011.
9. Yang, E.-S., Cunnold, D. M., Salawitch, R. J., McCormick, M. P., Russell III, J. M., Zawodny, J. M., Oltmans, S., and Newchurch, M. J.: Attribution of recovery in lower-stratospheric ozone, *J. Geophys. Res.*, 111, D17309, doi:10.1029/2005JD006371, 2006.

6.16 *hbk00059*: Joint state-parameter estimation for the Last Glacial Maximum with CESM1.2

| | |
|---------------------|--|
| HLRN Project ID: | hbk00059 |
| Run time: | III/2018 – II/2020 |
| Project Leader: | Prof. Dr. M. Schulz |
| Project Scientists: | J. García-Pintado |
| Affiliation: | Fachbereich Geowissenschaften, MARUM-- Zentrum für Marine Umweltwissenschaften, Universität Bremen |

Overview

The PALMOD project, funded by BMBF, seeks to understand climate system dynamics and variability during the last glacial cycle. Specific topics are: i) to identify and quantify the relative contributions of the fundamental processes which determined the Earth's climate trajectory and variability during the last glacial cycle, ii) to simulate with comprehensive Earth System Models (ESMs) the climate from the peak of the last interglacial (the Eemian warm period) up to the present, including the changes in the spectrum of variability, and iii) to assess possible future climate trajectories beyond this century during the next millennia with sophisticated ESMs tested in such a way.

Relevant to this computing project proposal, an expected major outcome of the first (4-yr) phase of PALMOD is to obtain a comprehensive data synthesis of paleoclimatic conditions during the last glacial cycle, associated with explicit estimates of uncertainty. This involves combining in the best possible ways the outcome of long-term climate model simulations with the last generation of multi paleo proxy data (planktic foraminifera, diatoms, dinoflagellates, radiolaria, geochemical proxies as Mg/Ca in planktic foraminifera shells, etc.). For this, we are using a global climate model; the Community Earth System Model version 1.2 (CESM1.2), and assimilating homogenized multi-proxy observations, generated within the scope of PALMOD, into CESM. Ensemble reconstructions from the coupled model at the Last Glacial Maximum (LGM) are being analysed along with a transient higher resolution simulation of the post LGM-deglaciation.

Results

In the previous years, we setup an assimilation scheme and conducted analysis of tropical coral $\delta^{18}O$ and Sr/Ca for preindustrial conditions and synthetic analysis based on LGM pseudo-proxy observations of SST derived from the MARGO multiproxy database, in preparation for the coming PalMod compilation of marine and terrestrial proxy observations. García-Pintado and Paul (2018), supported by computations in HLRN-III, summarises some work regarding the synthetic analyses. Overall, the sensitivity analyses were extremely useful to rank a number of key uncertain parameters in the coupled climate model, which are not sufficiently constrained by modern observations (past climates are an extrapolation situation under which current parameter have not been tested), and so to guide decisions regarding the selection of control variables for the coming LGM analyses. Also, the analysis of tropical coral, calibrated against HadISST, illustrated some of the problems in relation with the sparsity of the datasets and on the model-data comparison approaches, which are a stumbling stone for the assimilation of paleoclimate proxy observations. It is clear that from a local point of view strong nonlinear sensitivities appear and hamper linear approaches to data assimilation. An example is depicted in Figure 1, which shows a strong nonlinear relationship between SST at an

observation location in the North Atlantic and a global parameter controlling low cloud formation as a function of moisture. While this may be seen as an extreme case, it is not unique and illustrates the issue of nonlinearity when combined with the issue of sparsity in the observational dataset. This calls for specific quality control design and reconsideration of the model-data comparison for paleoclimate analyses.

As summarized in the caption of Figure 1, in this case, the strongest factor in the nonlinear relation actually results from a southward movement of the North Atlantic subpolar. This does not necessarily mean that there is a substantial change of regime. However, in addition to these situations, strong transitions appear for some model configurations, which (at the view of more recent experiments in HLRN-IV) indicate, e.g., that a bistable AMOC is possible with this model. The implications for the resulting modeled climate are huge. Moreover, a “low AMOC” regime is shown as a strong attractor, in which the model sensitivity to certain parameters for the model physics is negligible as compared with the corresponding sensitivities for a “strong AMOC” regime. Also, recent simulations in HLRN-IV confirm that integration times of ~1000 year are needed to have a reasonable trust in the sensitivity estimation. Other example of the conducted experiment is shown in Figure 2, where the finite difference sensitivity iterated Kalman smoother (FDS-IKS, as described in García-Pintado and Paul, 2018) is evaluated versus an (spherical simplex) ensemble transform Kalman filter (EKTF). In this case, the bias reduction is quantitatively similar, but the computational cost is substantially lower for the FDS-IKS. Future increase in computational power could allow for expanded experiments. As an example, if it was computationally feasible, an iterated ensemble Kalman smoother (which considers global sensitivities as opposed to the (adjoint-like) local sensitivities of the FDS-IKS could potentially show to be more robust than the FDS-IKS.

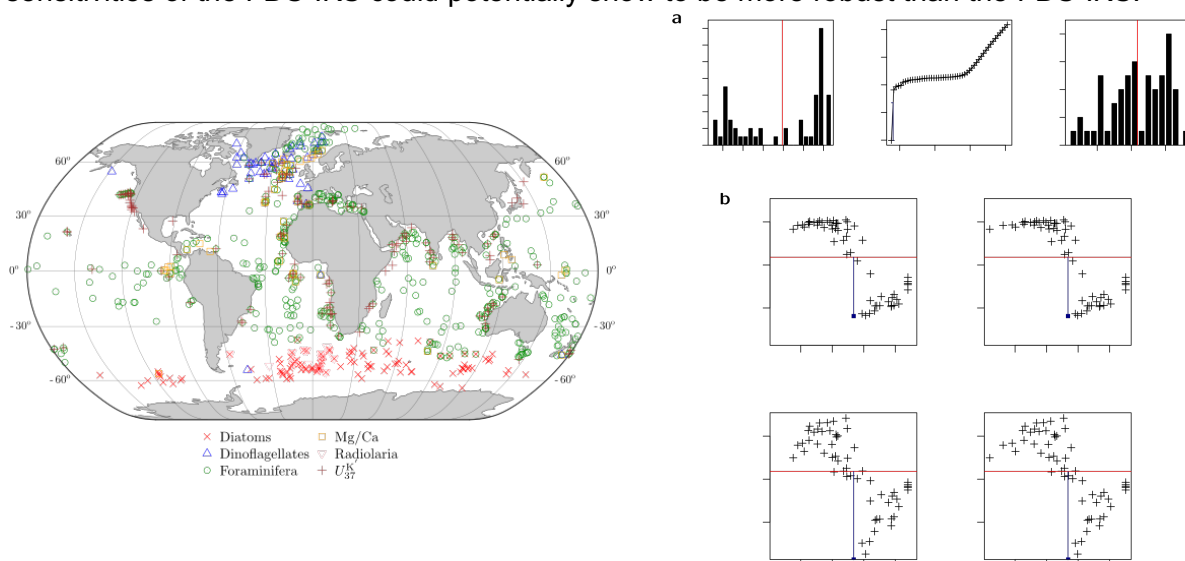


Figure 1: Distribution of MARGO paleoclimate proxy observations for LGM, and one example of strong nonlinear relation between SST at a location in the North Atlantic and the global threshold in moisture for low cloud formation. A southward displacement of the North Atlantic subpolar front as this threshold increases creates the strong negative jump at the observation location, contrasting with the otherwise positive sensitivity of SST to this parameter at the site.

The last year of computing project has been somehow difficult with the transition from HLRN3 to HLRN4. We decided on an early migration to the new environment in HLRN4 Göttingen, which, in addition to the required adaptation of CESM to the new computing environment, came along with our new implementation of the (carbon and water) isotope enabled CESM. Initially, HLRN4 suffered a successive updating of modules and lacked a parallel debugger. With these factors together it became complicated to disentangle the issues due to

incompatibilities with the new system libraries (e.g. MPI & netCDF versions) from issues due to the new isotope modules. This has brought the project to a substantial delay. Still, we have managed to have a running version of CESM with a dynamic carbon cycle, and with carbon and water isotopes simulations, as well as conducted tests for preindustrial and Last Glacial Maximum (LGM) conditions.

The implementation of isotope-enabled CESM (iCESM) and throughput analysis and configuration in HLRN4 Göttingen is now complete. As mentioned, the configuration includes both carbon and water isotopes, and we have implemented the protocols for preindustrial and LGM conditions. We have conducted successful simulations with the atmospheric component (iCAM5) forced by gridded boundary conditions for SST and sea ice, as well as initial simulations with the fully coupled iCESM.

As an example, Fig 2 shows total Delta18O in precipitation from the atmospheric component and Delta18O in the surface layer in the ocean component of CESM for preindustrial conditions. The latter can, e.g., be compared against the dataset published by LeGrande and Schmidt (2006), which has the same range and location of extrema (Hudson Bay minimum and Mediterranean maximum), as well as similar global patterns. The new configuration is running at 1° global resolution. Currently we have stopped the LGM simulation, as we have found some indication that the long-term trend of the global water-isotope patterns departs from what we expected for the ocean after some thousand years, while the look stable for the atmospheric component. This happens similarly for simulations with and without depth-dependent tracer acceleration for the ocean. To be on the side of caution with respect to NPL consumption we are now currently running only carbon-isotope simulations and simultaneously evaluating the code for the ocean water isotopes and its matching with data for modern observations.

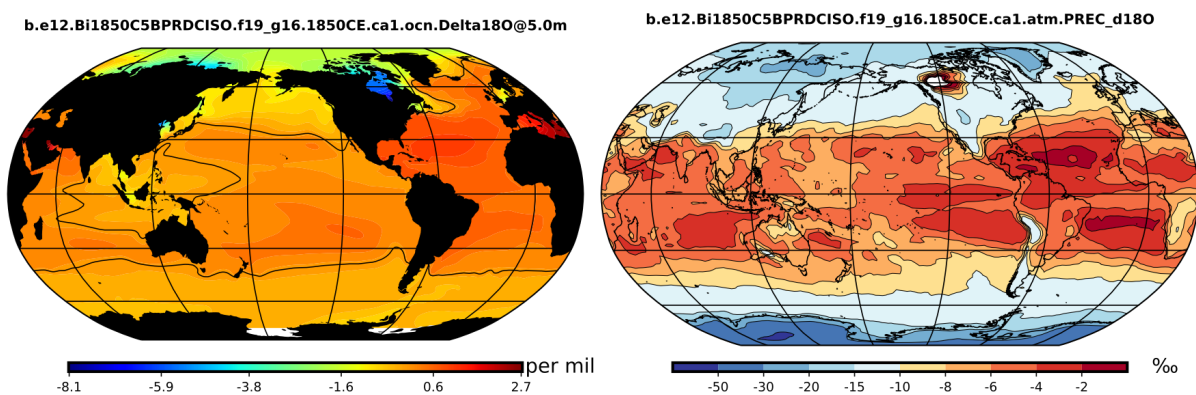


Figure 2: CESM delta18O in total precipitation and the ocean surface layer for preindustrial conditions.

Outlook

We are in the process of setting up initial conditions, including the water isotopes and carbon isotopes for the equilibrium simulation at LGM. The isotope-enabled CESM simulations will be finished for preindustrial conditions and LGM in first instance. Results will be intercompared, within the framework of PalMod, with results from the model MPI-ESM-wiso (conducted by collaborators in AWI), and analysed with the new proxy compilations processed within PalMod by other groups.

Publications

1. J. García-Pintado, A. Paul, *Evaluation of iterative Kalman smoother schemes for multi-decadal past climate analysis with comprehensive Earth system models*, *Geoscientific Model Development*, 11, 5051-5084 (2018)

Presentations

1. J. García-Pintado, B. Fallah, T. Felis, J. Zinke, M. Pfeiffer, A. Paul., *Exploring coral data for multi-decadal paleoclimate reanalysis with the Community Earth System Model*, EGU, Vienna, 11 April, 2018

6.17 *hbk00061*: Combining ocean models and proxy data

| | |
|--------------------|--|
| HLRN Project ID: | hbk00061 |
| Run time: | III/2017 – II/2019 |
| Project Leader: | Prof. Michael Schulz |
| Project Scientist: | Charlotte Breitzkreuz |
| Affiliation: | MARUM – Center for Marine Environmental Sciences and Faculty of Geosciences, University of Bremen |

Overview

This project is part of the National Climate Modeling Initiative PalMod. The overarching goal of PalMod is to simulate the complete last glacial cycle, that is, the past 120 thousand years, with comprehensive Earth-system models. Understanding past climate states is essential for predicting future climate change and validating climate models by applying them to climate states that were very different from today is important to deepen our trust in models and hence, in their projections for future climate.

Our project focuses on the development and application of a data assimilation (DA) method to estimate the state of the ocean during the Last Glacial Maximum (LGM, 19-23 thousand years ago) with ocean general circulation model and proxy data. The LGM was the last time during the Earth's history when the climate was substantially different from today, but remained relatively stable for a few thousand years. The large-scale patterns of the ocean circulation during this time remain uncertain. Reconstructions from proxy data as well as from modeling studies have large uncertainties and different studies show a broad range of possibilities of the ocean state during that time interval. Uncertainties in paleo-climate modeling originate, for example, from uncertain boundary conditions, uncertainties in model parameters, and other model errors. Proxy data, on the other hand, have uncertainties regarding the imprint of the climate signal in the proxy, disturbances during the deposition, and measurement errors. Combining climate models with proxy data and their respective uncertainties via DA is a powerful means to obtain more reliable estimates of past climate states.

The DA method in this project aims at optimizing uncertain model parameters and boundary conditions including the atmospheric forcing of the ocean, such as precipitation and air temperature. A successful estimate is consistent with the physics incorporated in the model and with the proxy data within their respective uncertainties. Data assimilation is frequently used in the field of weather forecasting, but it is still not well-established in the community of paleoclimatology because available proxy data is very sparse and comprehensive data sets of past climate states have only become available in the past years.

Methods

We employ the Massachusetts Institute of Technology general circulation model (MITgcm), a coupled ocean-sea ice general circulation model. The model uses a cubed-sphere grid with 192 x 32 horizontal grid cells, resulting in a resolution of about 285 km, and 15 vertical levels. The low resolution of the model enables us to perform long equilibrium simulations, running about 2,000 model years to a quasi-steady state. The MITgcm is enhanced with a water isotope module (Völpel et al., 2017) that gives us the possibility to simulate the oxygen isotopic ratio of seawater ($\delta^{18}\text{O}_{\text{sw}}$) in the whole water column.

A recent state estimate of the LGM ocean was obtained by Kurahashi-Nakamura et al. (2017) with the adjoint method. The method requires the adjoint of the model code, which can be obtained by "automatic differentiation". However, this approach is not applicable to many models. Moreover, the adjoint method does not readily provide an uncertainty estimate of the solution and it is computationally very expensive. We, therefore, aim at developing an efficient DA method that provides an uncertainty estimate and that is independent of the existence of an adjoint, such that it can be applied with other, more expensive models.

To that end, we combine a state reduction approach with a finite difference sensitivity-iterative Kalman smoother (FDS-IKS, García-Pintado and Paul, 2018) to estimate the spatially varying atmospheric forcing fields. The state reduction approach enables us to estimate the spatially varying atmospheric forcing by only estimating a number of parameters at the order of 10^1 . The FDS-IKS is based on the iterative Kalman smoother (Bell, 1994) and uses an approximation of the tangent linear derivative of the model through finite difference sensitivities obtained from perturbation experiments.

Results

We tested the approach by applying it to pseudo-proxy data generated from target model simulations and estimating 16 parameters in air temperature, precipitation, and isotopic composition of precipitation and water vapor. The data were sampled from the target model simulation at locations where data is available for the LGM and an error was added to the data to include the uncertainty that is present in LGM proxy data. Our results demonstrate that the method is capable of efficiently reducing the model-data misfit and reconstructing the target ocean circulation.

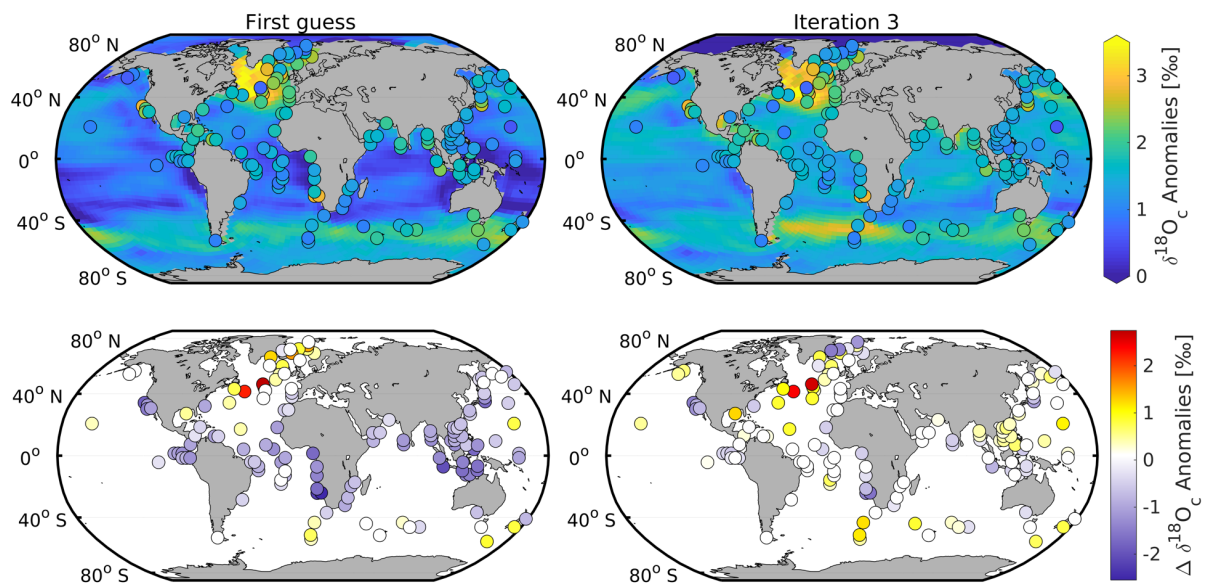


Figure 1: Simulated 100-year mean surface field (0–50 m) of $\delta^{18}\text{O}_a$ LGM-Late Holocene anomalies in the first guess and LGM optimization (iteration 3) and assimilated planktic $\delta^{18}\text{O}_c$ anomaly data (upper panels), and respective model-data differences (lower panels). Differences smaller than the uncertainty of the observational data are displayed in white.

We additionally applied the method to estimate the state of the LGM ocean. To constrain the LGM estimate, we used global data on the oxygen isotopic composition of calcite ($\delta^{18}\text{O}_c$) and a global sea surface temperature reconstruction (MARGO Project members, 2009). The model-data misfit is greatly reduced within the first three iterations (Figure 1), but some model-data misfit remains for the planktic and benthic $\delta^{18}\text{O}_c$ data (Figures 1 and 2). The estimated LGM ocean state shows a shallower North Atlantic Deep Water (Figure 2, lower panel) compared to today coinciding well with previous estimates (e.g., Lynch-Stieglitz et al., 2007).

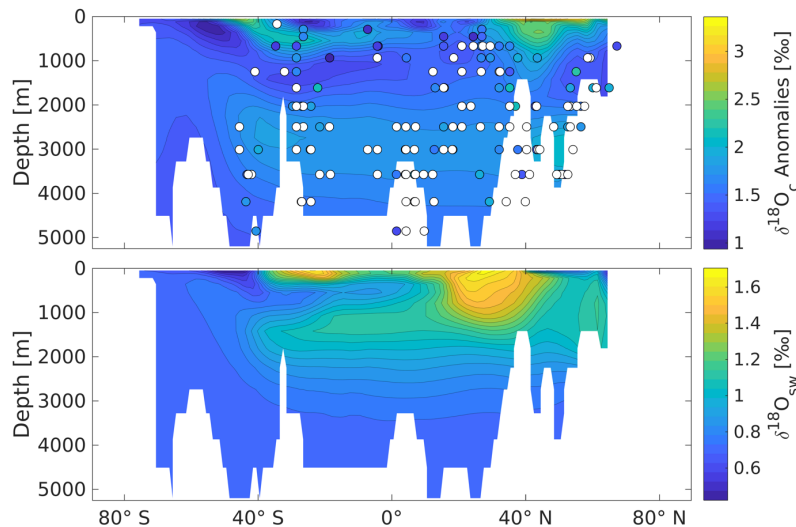


Figure 2: Simulated 100-year mean $\delta^{18}\text{O}_c$ LGM-Late Holocene anomalies (upper panel) and simulated 100-year mean $\delta^{18}\text{O}_{sw}$ at a vertical transect through the Atlantic Ocean at 32.5°W in the LGM optimization (iteration 3) and assimilated benthic $\delta^{18}\text{O}_c$ anomaly data. Data points where the model agrees with the observational data within their respective uncertainties are displayed in white.

Publications

1. C. Breitkreuz, A. Paul, S. Mulitza, J. García-Pintado, and M. Schulz: A reduced-order Kalman smoother for (paleo-)ocean state estimation: assessment and application to the LGM, *Geosci. Model Dev. Discuss.*, <https://doi.org/10.5194/gmd-2019-32>, in review, 2019.

Presentations

1. C. Breitkreuz, A. Paul, P. J. van Leeuwen, M. Schulz, *A new particle filter method to estimate the state of the ocean during the Last Glacial Maximum*, Poster at EGU General Assembly, April 2018, Vienna.
2. C. Breitkreuz, A. Paul, J. García-Pintado, M. Schulz, *Using data assimilation to estimate the global ocean state during the Last Glacial Maximum*, Poster at the 3 Cluster Conference, October 2018, Berlin.

References

- Bell, B. M.: The iterated Kalman smoother as a Gauss–Newton method, *SIAM Journal on Optimization*, 4, 626–636, 1994.
- García-Pintado, J. and Paul, A.: Evaluation of iterative Kalman smoother schemes for multi-decadal past climate analysis with comprehensive Earth system models, *Geoscientific Model Development*, 11, 5051–5084, 2018.
- Kurahashi-Nakamura, T., Paul, A., and Losch, M. Dynamical reconstruction of the global ocean state during the Last Glacial Maximum. *Paleoceanography*, 32(4):326–350, 2017.

Lynch-Stieglitz, J., Adkins, J. F., Curry, W. B., Dokken, T., Hall, I. R., Herguera, J. C., Hirschi, J. J.-M., Ivanova, E. V., Kissel, C., Marchal, O., et al.: Atlantic meridional overturning circulation during the Last Glacial Maximum, *Science*, 316, 66–69, 2007.

MARGO Project Members. Constraints on the magnitude and patterns of ocean cooling at the last glacial maximum. *Nature Geoscience*, 2(2):127–132, 2009.

Völpel, R., André, P., Krandick, A., Mulitza, S., and Schulz, M. Stable water isotopes in the MITgcm. *Geoscientific Model Development*, 10(8):3125, 2017.

6.18 *hbk00062*: Retrieval of stratospheric ozone profiles from OMPS observations in limb geometry and long term trends

| | |
|---------------------|--|
| HLRN Project ID: | hbk00062 |
| Run time: | IV/2017 – III/2020 |
| Project Leader: | Dr. Alexei Rozanov |
| Project Scientists: | Dr. Carlo Arosio, Dr. Alexei Rozanov |
| Affiliation: | Institute of Environmental Physics, University of Bremen |

Overview

Stratospheric ozone recovery is expected during the 21st century according to model studies (Eyring et al. 2010), as a consequence of the decreasing emission of chlorine-containing ozone depleting substances (ODSs) and the increasing concentration of CO₂ in the troposphere. ODSs are namely involved in catalytic cycles, which contribute to ozone destruction, while the increasing CO₂ concentration leads to a cooling of the stratosphere, which reduces the efficiency of some temperature-dependent ozone depleting reactions.

To monitor the status of the ozone layer and the onset of its recovery, satellite measurements are an important tool, as they provide observations with high temporal and spatial resolution. In particular, measurements in limb geometry, as performed by SCIAMACHY (SCanning Imaging Absorption spectroMeter for Atmospheric Chartography) and OMPS-LP (Ozone Mapping and Profiler Suite – Limb Profiler), enable the study of ozone profiles with a vertical resolution of about 3 km. However, single satellite missions are generally too short to assess long-term ozone changes and the merging of several time series is therefore required.

Several studies addressed the analysis of stratospheric ozone trends over the last decades, for example Harris et al. (2015), Sofieva et al. (2017) and Steinbrecht et al. (2017). The authors considered zonally averaged data and found a large variability between data sets. They detected positive trends in the upper stratosphere, particularly at mid-latitudes, a hint of the ozone recovery. In the lower stratosphere, where a decrease in ozone concentration is expected due to the speed-up of the tropical upwelling, results are still affected by a large uncertainty and the observation of negative trends still disputed (Ball et al. 2017).

In this framework, the main activities within this project are related to the retrieval of ozone profiles from OMPS-LP satellite observations, starting from the beginning of 2012 till present. The radiative transfer model and spectroscopic data bases are the same used for the retrieval of SCIAMACHY ozone profiles. The retrieval approach is also similar, in order to minimize systematic biases between the two time series. Once OMPS-LP ozone profiles are retrieved and validated, the second goal is the merging with the SCIAMACHY time series, to study altitude, latitude and longitude resolved ozone changes over the last 15 years. Improvements in the retrieval of ozone profiles are ongoing, with particular regard to the lowermost stratosphere in the tropics.

Results

Retrieval of ozone profiles

A new complete retrieval of OMPS-LP time series (from February 2012 to December 2019) has been performed during the last year. To check the quality of the data set, we validated the ozone profiles against ozonesonde measurements, particularly valuable in the lower stratosphere up to 30 km. The high vertically-resolved observations from sondes had first to be convolved with the averaging kernels of the retrieval, to be comparable with lower resolution satellite observations. Fig. 1 shows the results of the comparison in terms of relative differences between sondes and OMPS-LP ozone profiles in several latitude bands, averaged over the 2012-2019 period. The best performance has been found at northern mid-latitudes with an agreement within $\pm 3\%$ between 12 and 28 km. In the tropics a discrepancy above 10% is visible below 15 km. The small ozone values in the ULTS amplifies the relative difference at these altitudes. In addition, even though we accounted for aerosol and cirrus clouds in the ozone retrieval, they may still affect the retrieval at these altitudes. In the southern hemisphere the comparison is not as good as in the northern hemisphere, but still within $\pm 7\%$ below 30 km.

Over a restricted time period, several retrieval have also been tested in order to improve the quality of the profiles in the lower stratosphere and upper troposphere (UTLS), particularly in the tropics. Panel (b) of Fig. 1 displays profiles of the relative difference between IUP-OMPS and sondes averaged in the tropics over 6 months in 2016, considering four versions of the retrieval. The use of retrieved aerosol profiles was implemented in the so-called 'Vers 1'. The exclusion from the Chappuis band of spectral points affected by the absorption of species like O_4 , O_2 and H_2O was implemented between 'Vers 1' and 'Vers 2', and it is crucial to reduce the discrepancy around 16-20 km. The decrease of the cloud flag threshold, implemented in 'Vers 3', helps to exclude thin cirrus cloud cases and improves the agreement with sondes below 18 km. Tuning the Tikhonov parameter at the lower altitudes is also important to reduce the oscillations of the profile in a region where the sensitivity of limb measurements decreases.

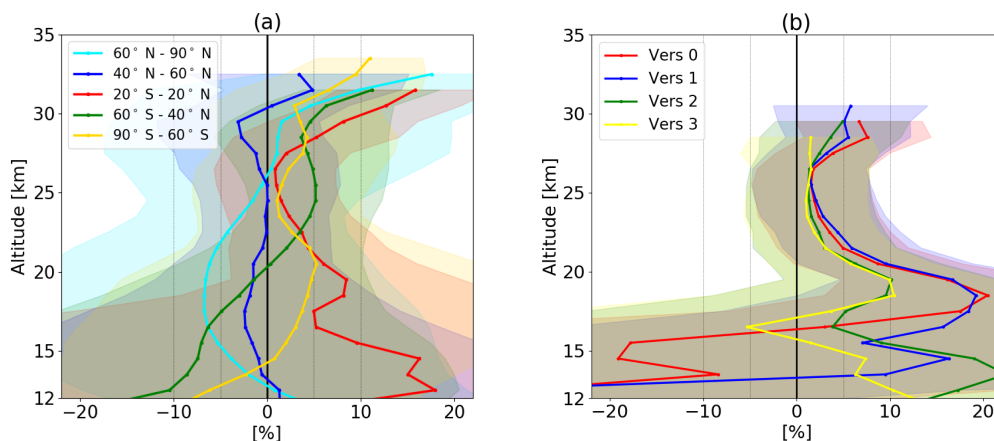


Figure 1: Panel (a), relative differences between OMPS-LP retrieved ozone profiles and ozonesonde measurements in 5 latitude bands averaged over the 2012-2019 period. Panel (b), relative differences with respect to sondes in the tropics using different retrieval versions, averaged over the period Jan 2016 – Jun 2016.

Merging and long term trends

The merging with SCIAMACHY time series was performed using MLS (Microwave Limb Sounder) satellite observations as a transfer function. SCIAMACHY and OMPS missions have an overlap of only 2 months, not sufficient to remove the bias between the two. By merging the two data sets, we obtained an ozone time series starting from 2003, vertically resolved every 3.3 km. Spatially, we binned the profiles every 5° latitude and 20° longitude, enabling the study of longitudinally resolved structures and changes in the ozone distribution. Details of the merging procedure can be found in Arosio et al. (2019).

A multi-linear regression model, accounting for several phenomena which affect the ozone distribution, like the Quasi Biennial Oscillation, the Solar activity and El Nino, was applied. Results are reported in Fig. 2: on the left panel zonally averaged trends over the 2003-2018 period are shown. Statistically significant trends correspond to non-dashed areas and were mainly found at mid-latitudes in the middle and upper stratosphere, with the highest values in the northern hemisphere. In the lower tropical stratosphere, we detected negative but not significant trends. In panel (b) of this figure, the longitudinally resolved structure is displayed at 41 km, where a large variability was found: positive values over the Canadian sector and small non-significant values over Siberia. The assessment of the stability and reliability of these longitudinal structures is still ongoing, exploiting a possible synergy with a chemistry transport model.

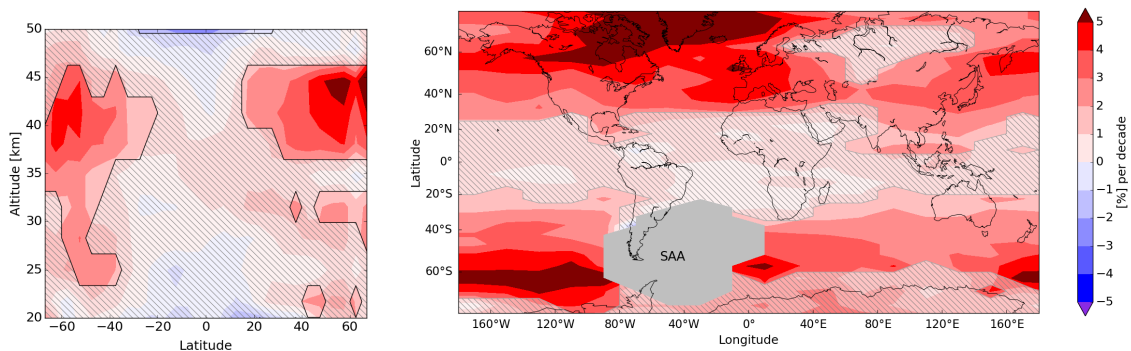


Figure 2: Long-term ozone changes over the 2003-2018 period: in the left panel the zonally averaged trends, in the right panel longitudinally resolved results at the altitude of 41 km. Shaded areas indicate non-significant trends.

In the tropical middle stratosphere over the last 15 years, a fluctuation of the trend has been found, from negative values until 2011 to positive values from 2011. The causes behind this change are still under investigations. Galytska et al. 2019 studied the long-term changes over SCIAMACHY period and related the positive trend around 35 km in the tropics to dynamical changes: the vertical transport was found to speed up during winter months, causing a change in the residence time of NO₂, which in turn affects ozone concentration in this region.

Outlook

An improvement of the ozone retrieval is planned, including also a retrieval of polar mesospheric clouds (PMC). Currently, profiles affected by the presence of a PMC in the instrument field of view are screened out.

A comparison with a chemistry transport model is planned to help understanding the changes in ozone distribution over the last 15 years and assess the reliability of the longitude-resolved features that we found in our merged data set.

Publications

1. Arosio, C., et al. "Retrieval of ozone profiles from OMPS limb scattering observations." *Atmospheric Measurement Techniques*, 11.4 (2018): 2135-2149.
2. Arosio, C., et al. "Merging of ozone profiles from SCIAMACHY, OMPS and SAGE II observations to study stratospheric ozone changes", *Atmospheric Measurement Techniques*, 12.4, (2019): 2423-2444.
3. Arosio, C. "Retrieval of ozone profiles from OMPS-LP observations and merging with SCIAMACHY and SAGE II time series to study long-term changes.", PhD dissertation, (July 2019).

Presentations in 2019

4. Arosio, C., et al. "Merging ozone profiles from SCIAMACHY and OMPS limb observations to study long-term ozone changes in the stratosphere." Unpublished, presented at the conference Living Planet 2019, Milan, (2019, May).
5. Arosio, C., et al. "Merging ozone profiles from SCIAMACHY and OMPS limb observations to study longitudinally resolved long-term ozone changes in the stratosphere." Unpublished, presented at the conference 10th Atmospheric Limb Workshop, Greifswald, (2019, June).

References

- Ball, W. T., et al. "Continuous decline in lower stratospheric ozone offsets ozone layer recovery." *Atmospheric Chemistry and Physics* (2017).
- Eyring, V., et al. "Multi-model assessment of stratospheric ozone return dates and ozone recovery in CCMVal-2 models." *Atmospheric Chemistry and Physics* 10.19 (2010): 9451-9472.
- Galytska, E., et al. "Dynamically controlled ozone decline in the tropical mid-stratosphere observed by SCIAMACHY." *Atmospheric Chemistry and Physics* 19.2 (2019): 767-783.
- Harris, N. R. P., et al. "Past changes in the vertical distribution of ozone—Part 3: Analysis and interpretation of trends." *Atmospheric Chemistry and Physics* 15.17 (2015): 9965-9982.
- Sofieva, V. F., et al. "Merged SAGE II, Ozone_cci and OMPS ozone profile dataset and evaluation of ozone trends in the stratosphere." *Atmospheric Chemistry and Physics* 17.20 (2017): 12533-12552.
- Steinbrecht, Wolfgang, et al. "An update on ozone profile trends for the period 2000 to 2016." *Atmospheric chemistry and physics* 17.17 (2017): 10675-10690.

6.19 *hbk00064*: Coupled ensemble data assimilation for Earth system models

| | |
|--------------------|--|
| HLRNProject ID: | hbk00064 |
| Run time: | I/2019 – I/2020 |
| Project Leader: | Prof. Dr. Thomas Jung ^{1,2} |
| ProjectScientists: | Dr. Qi Tang ² , Dr. Lars Nerger ² |
| Affiliation: | ¹ also at University of Bremen ² Alfred-Wegener-Institute for Polar and Marine Research, Bremerhaven |

Overview

Earth system models simulate different compartments like the ocean, atmosphere, or land surface. Data assimilation for Earth system modeling is challenging due to the complexity of different compartments within the model. In this project, we explore the role of data assimilation into an Earth system model which contains different compartments like the ocean and the atmosphere. Numerical experiments are carried out using the AWI climate model AWI-CM (Sidorenko et al., 2015) and the parallel data assimilation framework PDAF (<http://pdaf.awi.de>, Nerger et al., 2005, Nerger and Hiller, 2013). Within AWI-CM, the ocean model FESOM and the atmospheric model ECHAM are coupled through the coupler software OASIS3-MCT.

Currently the system allows us to assimilate global satellite sea surface temperature (SST) and temperature and salinity profiles into the ocean state. Thus, it influences the atmospheric state only through the model dynamics, which is the so-called ‘weakly coupled data assimilation’. The satellite SST observations used in this study are the Copernicus Level-3 product and were collected daily from multiple sensors covering almost the complete globe (80 °N- 80 °S) with a resolution of 0.1 degrees. Data gaps exist due to clouds. The temperature and salinity profiles are from the EN4 data set of the UK MetOffice. They can reach down to 5000m and the average number of profiles is about 1000 per day with quality check. The sea surface height, velocity, temperature and salinity are updated daily using an ensemble Kalman filter (EnKF) for a one-year assimilation period of 2016. The ensemble size is set to 46. For FESOM, the resolution is varying between 160 km in the open ocean and about 30 km in the equatorial region and parts of the Arctic Ocean. For ECHAM a resolution of T63 with 47 layers is used. The initial ensemble was generated from an EOF decomposition of a 1-year model run for the same year 2016. For the one-year assimilation run, 12,144 processor cores were used with fully parallelized codes for 5.5 hours on HLRN.

Results

Four different simulation scenarios were carried out for different types of observations:

- 1) A free run scenario without data assimilation, denoted as ‘Free_run’
- 2) A scenario where only the SST data were assimilated, denoted as ‘DA_SST’
- 3) A scenario where only the profile data were assimilated, denoted as ‘DA_proTS’
- 4) A scenario where both the SST and profile data were assimilated, denoted as ‘DA_all’

We analyze whether data assimilation can improve the prediction of the ocean as well as the atmospheric states in a coupled ocean-atmosphere model by assimilating only the ocean observations. The RMSE is calculated for the SST, and subsurface temperature and salinity over all the observation points and the whole simulation period to evaluate the data

assimilation experiments. An overview of the RMSE for different simulation scenarios is given in Figure 1.

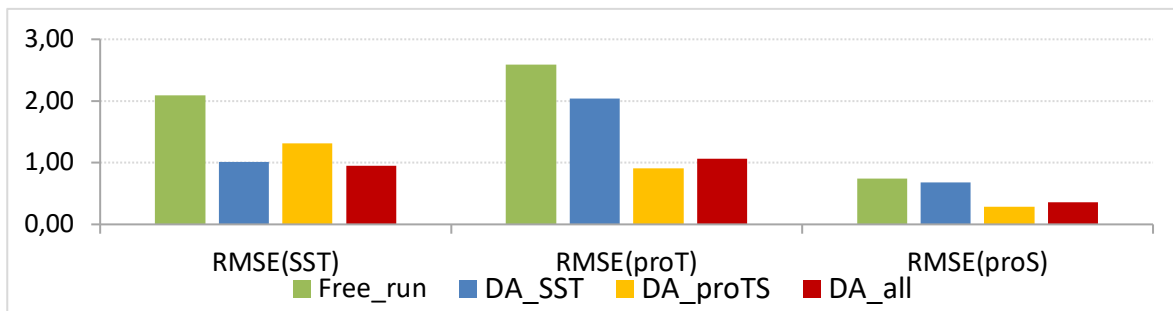


Figure 1: RMSE of SST, subsurface temperature and salinity for different simulation scenarios for the whole one-year simulation period.

1) Assimilation impact on the ocean temperature and salinity

When assimilating SST in DA_SST, the deviation between the modeled SST and the assimilated SST data is reduced globally by 50% compared to the free run. If only the subsurface temperature and salinity are assimilated (DA_proTS), the reduction of the RMSE of SST is still 35%. This indicates that the limited subsurface temperature information can also improve the SST by utilizing the highly vertical correlations in the mixed layer. The RMSE of the subsurface temperature is reduced by 18% by assimilating only the surface temperature (DA_SST), which again shows that the temperature at deeper layers is highly correlated to the surface temperature.

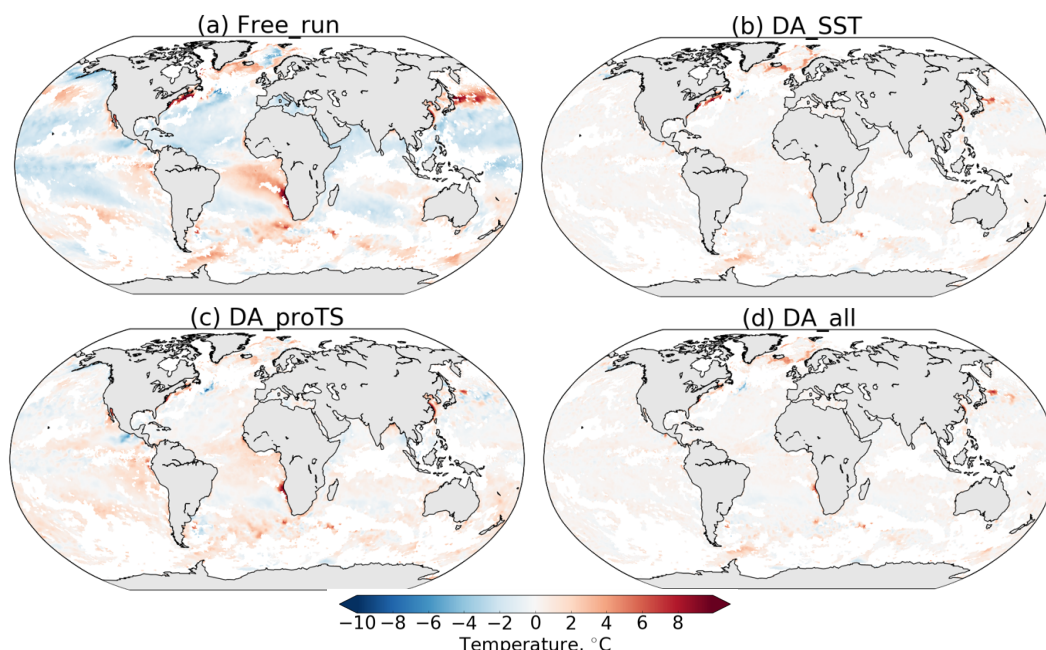


Figure 2: Difference of sea surface temperature between the model simulation and the observations on December 31st, 2016 for different simulation scenarios: a) Free_run, b) DA_SST, c) DA_proTS and d) DA_all.

Figure 2 shows the SST difference between the model simulation and the observations at the end of the assimilation period on 31st Dec 2016. The difference is strongly decreased when assimilating either the surface or the subsurface temperature or both of them. The global

average of the absolute SST difference is only 0.44 °C for scenario DA_SST compared to 1.54 °C for the free run. The subsurface deviation is also reduced by all the assimilation runs, which is not shown here. The reduction can be up to 65% by scenario DA_proTS, and 30% by scenario DA_SST.

Assimilating the profile observations in scenario DA_proTS leads to a 51% reduction in the RMSE of the subsurface salinity compared to the free run. If only SST is assimilated (DA_SST), the error in the salinity is reduced by 7%. This is quite limited compared to the other scenarios. As expected, scenario DA_all gives the lowest errors for the salinity prediction with an RSME reduction of subsurface salinity of up to 59%.

2) Assimilation impact on the atmosphere temperature and wind velocity

We evaluate the impact of the DA into the ocean on the atmosphere by comparing the atmospheric variables from the model prediction with daily fields from the ERA-Interim atmospheric reanalysis provided by ECMWF (Berrisford et al., 2011) for temperature at 2m above surface, surface pressure, zonal and meridional wind velocity at 10m above surface.

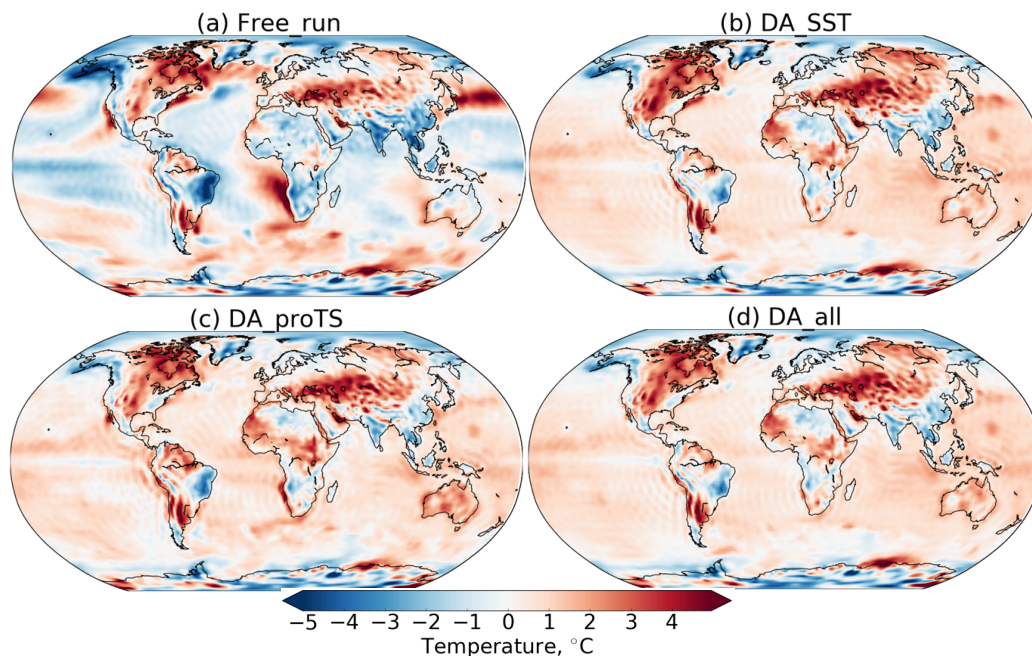


Figure 3: Mean difference over months March to December of temperature at 2m above the surface for different simulation scenarios: (a) the free run, (b) DA_SST, (c) DA_proTS and (d) DA_all.

Figure 3 shows the mean difference for the months March to December of temperature at 2m above surface between the model simulation and the ERA-Interim reanalysis data for the different simulation scenarios. In general, the three assimilation runs show a smaller difference than the free run in essentially all oceans. When assimilating only profile data in DA_proTS, the predicted 2-m temperature is also closer to ERA-Interim than the free run yielding a similar spatial pattern to assimilating only SST or both the SST and profile data. While the amplitude of the difference is generally smaller and more homogeneous for the assimilation scenarios compared to the free run, a positive bias is visible everywhere over the oceans except in the Arctic Ocean and parts of the Southern Ocean. While the free run has a bias of -0.15 °C, the assimilation leads to this positive bias of 0.32 °C for DA_SST, 0.26 °C for DA_proTS, and 0.28 °C for DA_all. Thus, the assimilation of DA_SST has the largest effect. The origin of this bias is unclear.

As SST is at the interface of the ocean and the atmosphere, an improved prediction of SST is expected to lead to a better prediction of the temperature in the atmosphere. However, the effect is only direct for the air temperature above the ocean. Over the continents the changes in the 2-m temperature are less evident than over the ocean. In particular the strong negative bias over South America is reduced by the assimilation. Likewise, the negative bias over India and South-East Asia is reduced. On the other hand the positive bias extending from the eastern Mediterranean to Siberia is increased.

Over land, the 10-m meridional and zonal wind velocities in the free run and the three data assimilation runs are rather similar (figures now shown in this report). The assimilation does not give rise to significant influence on the velocities there.

Outlook

The present weakly coupled data assimilation is limited to assimilating only ocean observations. Obviously, the additional assimilation of atmospheric observation would lead to a direct effect on the atmosphere. The alternative to weakly coupled DA is strongly coupled DA, in which the atmospheric as well as the oceanic variables are updated jointly using cross-covariances between the two components. Given that the data assimilation system used here can be extended for strongly-coupled assimilation, this study is a step toward the future investigation of the role of assimilating ocean observations into both the ocean and the atmosphere using a strongly coupled data assimilation system.

Publications

Tang Q., et al. *Improving the ocean and atmosphere in a coupled ocean-atmosphere model by assimilating satellite sea surface temperature and subsurface profile data*, Quarterly Journal of the Royal Meteorological Society, submitted

Presentations

Tang, Q., Sidorenko, D., and Nerger, L., Assimilation of satellite and profile observations into a coupled ocean-atmosphere model. Workshop on Conservation Principles, Data, and Uncertainty in Atmosphere-Ocean Modelling. April 3rd, 2019. Potsdam, Germany. Oral.

Tang, Q., Sidorenko, D., and Nerger, L., Assimilation of satellite and profile observations into a coupled ocean-atmosphere model. EGU General Assembly 2019. April 12th, 2019. Vienna, Austria. Oral.

Tang, Q., Mu, L., Sidorenko, D., and Nerger, L., Impact of assimilation of satellite sea surface temperature and profile observation on the ocean and atmosphere in a coupled ocean-atmosphere model. ESM summer school. September 2019. Bad Aibling, Germany. Poster.

References

Berrisford, P., et al. (2011). The ERA-Interim archive, version 2.0.

Nerger, L., and W. Hiller (2013), Software for ensemble-based data assimilation systems - Implementation strategies and scalability, *Computers & Geosciences*, 55, 110-118.

Nerger, L., W. Hiller, and J. Schröter (2005), PDAF-the parallel data assimilation framework: experiences with Kalman filtering, in *Use Of High Performance Computing In Meteorology*, edited, pp. 63-83, World Scientific.

Sidorenko, D., et al. (2015), Towards multi-resolution global climate modeling with ECHAM6-FESOM. Part I: model formulation and mean climate, *Climate Dynamics*, 44(3), 757-780.

6.20 **hbk00071: Development of an Earth system model coupled with a sediment diagenesis model toward long-term paleoclimate simulations**

| | |
|---------------------|--|
| HLRNProject ID: | hbk00071 |
| Run time: | I/2019 – IV/2019 |
| Project Leader: | Prof. Dr. Michael Schulz |
| Project Scientists: | Dr. Takasumi Kurahashi-Nakamura |
| Affiliation: | Fachbereich Geowissenschaften, MARUM – Zentrum für Marine Umweltwissenschaften, Universität Bremen |

Overview

It is well known that the CO₂ concentration in the atmosphere (hereafter, CO₂ level) has been increasing since the industrial revolution due to human's CO₂ emission so that it has reached a level that is unprecedented for at least the last 800,000 years. Our life in the future can suffer from climate changes induced by the increase in the CO₂ level and/or from the CO₂ increase itself (e.g., ocean acidification). To reliably project the CO₂ level in the future, it is essential to properly understand and model the mechanisms for CO₂-level changes. We are tackling this issue from a paleoclimatological viewpoint.

More specifically, simulating the history of CO₂ level during the last glacial cycle is one of the crucial tasks of the PalMod project (<https://www.palmod.de/>). Thus far, no comprehensive Earth system models (ESMs) are able to explain such a large change of the CO₂ level, which demonstrates our insufficient knowledge of the global carbon cycle. This HLRN project focuses on the marine carbon cycle because it is considered to play a crucial role in the variations of the CO₂ level during the last glacial cycle.

Diagenetic processes within ocean-floor sediments have a large influence on the marine carbon cycle at long timescales, and hence coupling a process-based sediment diagenesis model to ESMs is essential for our purpose. Therefore, in this project, we developed a new coupling scheme (Fig. 1) for the Community Earth System Model version 1.2 (CESM1.2) and the Model of Early Diagenesis in the Upper Sediment of Adjustable complexity (MEDUSA). The coupling contributes to the better modelling of exchange of biogeochemical matter between the bottom seawater and ocean-floor sediments, which leads to the improvement of model representation of seawater chemistry. Moreover, the sediment model acts as a more reliable “bridge” between the ocean model and paleoceanographic data (mostly obtained from ocean-floor sediments) providing an important fingerprint for the paleo-carbon cycle.

The MEDUSA coupling will yield another remarkable advantage with regard to the CaCO₃ dynamics. For long-term climate simulations including the global carbon cycle, the dynamical treatment of the CaCO₃ dissolution or preservation in the upper sediments will be essential because the budget of CaCO₃ in the global ocean, that is, the balance of the CaCO₃ inflow by land weathering and the outflow by sedimentary burial, would have had a substantial effect on the distribution of total carbon to the ocean and atmosphere, and hence CO₂ level, by changing the acidity or basicity of the entire ocean. We consider the MEDUSA–CESM coupled model including the “carbonate compensation” mechanism as a powerful tool to explore the climate dynamics at glacial–interglacial timescales that will give new insights into the feedback between the sediment processes and the global climate.

Results

The coupling of the two models was done in a so-called “offline” manner. We adopted the offline coupling considering the much longer characteristic timescale of the sediment model compared to that of the ESM. The offline method allowed manageability of model development and maintenance while being physically credible at the same time. We have substantially altered the source code of both models to provide proper interfaces for the coupling and newly developed routines to manage the exchange of necessary information (i.e. the boundary conditions) between the two models.

Having done initial experiments driven by model input corresponding to the preindustrial time-period, we found that the sediment-model coupling already had non-negligible immediate advantages for ocean biogeochemistry in millennial-timescale simulations. First, the MEDUSA-coupled CESM outperformed the original uncoupled CESM in reproducing the observation-based global distribution of sediment properties. Second, the MEDUSA-coupled model and the uncoupled model had a difference of 0.2‰ or larger in terms of $\delta^{13}\text{C}_{\text{dic}}$ of bottom water over large areas, which implied that different methods of sediment-diagenesis modelling can bring significant uncertainty of the simulated chemical composition of bottom seawater. Such model uncertainty would be a fundamental issue for paleo model–data comparison often relying on data derived from benthic organisms.

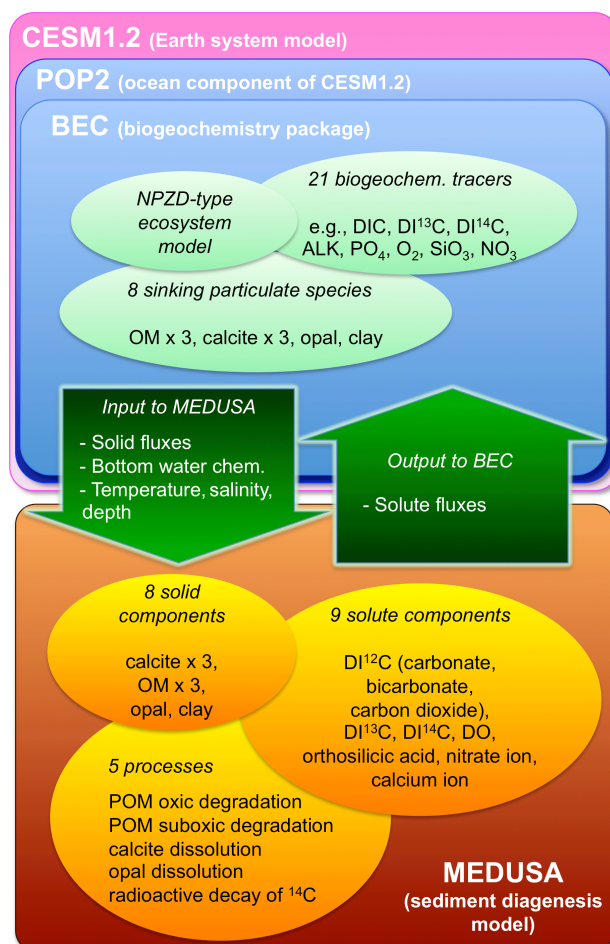


Figure 1: A schematic illustration of the coupling scheme for CESM and MEDUSA in this project (Kurahashi-Nakamura et al., 2020). In the list of chemical species, “D” stands for “dissolved” and “I” for “inorganic”; for example, DO means dissolved oxygen and DIC dissolved inorganic carbon. OM stands for organic matter. Each of OM and calcite components had three categories corresponding to each of major carbon isotopes (¹²C, ¹³C and ¹⁴C).

Other two time-slice simulations driven by glacial model input, which had different coupling frequencies among the CESM model components from each other, suggested that the sea-ice extent would have a great influence on the ocean state through the displacement of deep-

convection site in the high-latitude regions of both hemispheres. The glacial simulation with a higher coupling frequency yielded a much weaker and shallower upper cell of Atlantic meridional ocean circulation (AMOC) than that obtained in the low-coupling-frequency run. We simulated the solid weight fraction of CaCO_3 in the upper sediments with the MEDUSA-coupled model, and found that the global distribution of the weight fraction obtained from the high-coupling-frequency run would be more preferable in terms of the contrast to the modern distribution (Fig. 2).

This result strongly suggested that a weaker and shallower AMOC compared to the modern one would be more reasonable than a stronger and deeper AMOC as a feature of the physical ocean state during the LGM. On the other hand, the high-coupling-frequency setting somewhat impaired the model performance in a modern simulation to harm the model calibration aiming at the modern climate. In future simulations, therefore, it is required to improve the glacial ocean state obtained with the standard (low) coupling frequency, in turn, by changing a part of the model forcing, so that we can have a weaker and shallower AMOC and a more appropriate water-mass configuration for the glacial time period without harming the modern simulation.

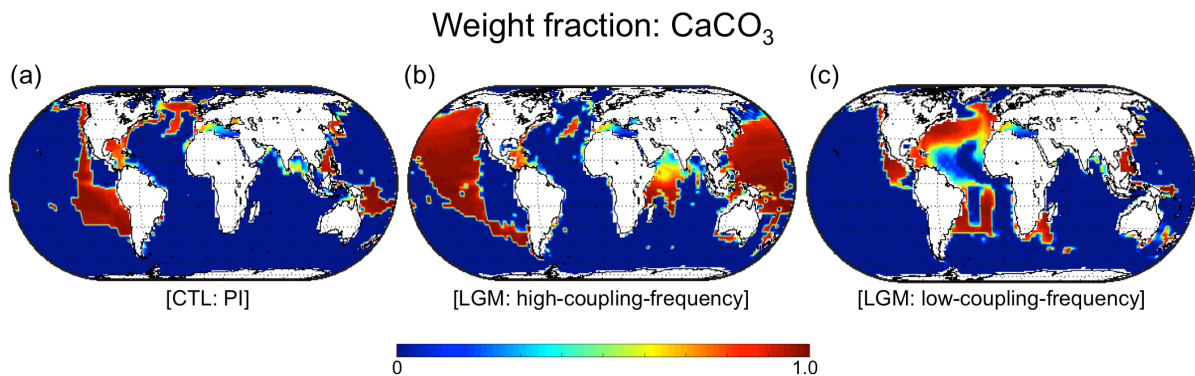


Figure 2: Simulated weight fraction of CaCO_3 out of total solid components in the upper sediments. (a) The control case corresponding to the modern state, and the glacial cases with (b) the high coupling frequency and (c) the low coupling frequency. An observation-based dataset (Catubig et al., 1998) show that the glacial weight fraction of calcite in the upper sediment is lower in the Atlantic and higher in the Pacific than the modern fraction, which was better reconstructed in the high-coupling-frequency run.

Outlook

We will continue the time-slice simulation series to obtain a common model configuration that provides appropriate model performance both for the modern age and the glacial time period. After obtaining a reasonable set of time-slice simulations, we will move on to transient simulations to reconstruct the transition of the climate system from the glacial regime to the interglacial regime. The simulated evolution of sediment composition and physical/biogeochemical ocean states will be analyzed to assess the model performance. The effect of carbonate compensation on the total inventory of dissolved inorganic carbon and alkalinity in the global ocean will be also discussed. In the coming phase of the project, the history of the CO_2 level used for the radiative forcing will be detached from the model carbon cycle and will be given by observation-based data instead. This will work as an important step towards a (potential) future project phase where the CO_2 level will interactively change as a result of the carbon cycle.

Publications

1. T. Kurahashi-Nakamura, A. Paul, G. Munhoven, U. Merkel, and M. Schulz, *Coupling of a sediment diagenesis model (MEDUSA) and an Earth system model (CESM1.2): a contribution toward enhanced marine biogeochemical modelling and long-term climate simulations*, Geosci. Model Dev., 13, 825–840, <https://doi.org/10.5194/gmd-13-825-2020> (2020)

References

N.R. Catubig, D.E. Archer, R. Francois, P. de-Menocal, W. Howard, and E-F. Yu, Global deep-sea burial rate of calcium carbonate during the Last Glacial Maximum, *Paleoceanography*, 13(3), 298–310, doi:10.1029/98PA00609 (1998)

6.21 *hbk00072*: Interannual variability of air-sea CO₂ exchange: high-resolution ocean biogeochemical simulations

| | |
|--------------------|---|
| HLRNProject ID: | hbk00072 |
| Run time: | I/2020 – IV/2020 |
| Project Leader: | Dr. Dieter Wolf-Gladrow ¹ |
| ProjectScientists: | Dr. Judith Hauck ² , Dr. Özgür Gürses |
| Affiliation: | Alfred Wegener Institute, Helmholtz Centre for Polar and Marine Research, ¹ principal investigator, also at the University of Bremen, ² project administrator |

Overview

Carbon dioxide (CO₂) emissions from fossil fuels and land-use change amounted to 11.3 PgC yr⁻¹ in 2017 (Le Quéré et al., 2018a) and force anthropogenic climate change. Ocean and land sinks provide an extremely valuable service to humankind by each drawing down about 25% of anthropogenic CO₂ emissions (Le Quéré et al., 2018a), thereby slowing the rate of anthropogenic climate change. On time-scales longer than a century the ocean will be the main repository for anthropogenic CO₂ emissions (Archer et al., 1997) and the Southern Ocean is the main conduit by which this CO₂ enters the ocean (Khatiwala et al., 2009).

In the Global Carbon Budget 2018 (Le Quéré et al., 2018a), a model evaluation metric was introduced that illustrates the mismatch between modelled and observed surface ocean pCO₂. It illustrates the amplitude of interannual variability that the models and the pCO₂-based flux products (Rödenbeck et al., 2014; Landschützer et al., 2014, surface ocean CO₂ Atlas, SOCAT) produce. One important outcome of this evaluation is that the models underestimate the interannual to decadal variability that is seen in the pCO₂-based flux products, especially in the temperate and high-latitudes (polewards of 30° N/S). Multiple studies based on observations have shown variability in the ocean CO₂ sink larger than estimated by the models, particularly related to representing the effects of variable ocean circulation in models (e.g., DeVries et al., 2017). This may be due to the absence of internal variability which is not captured by single realizations of coarse resolution model simulations (Li and Ilyina, 2018), and is thought to be largest in regions with strong seasonal and interannual climate variability, i.e. the high latitude ocean regions (poleward of the subtropical gyres) and the equatorial Pacific (McKinley et al., 2016).

In this project, we use FESOM (Finite Element Sea Ice-Ocean Model v. 1.4, Wang et al. 2014) coupled to REcoM2 (Regulated Ecosystem Model 2, Geider et al., 1996, 1998). Our main objective is to quantify the differences between low and high ocean resolution to allow more detailed interpretation of the hypothesis that variability of ocean circulation and air-sea CO₂ exchange will improve in a higher resolution set-up.

Currently, we compare simulations performed with FESOM1.4 on two unstructured meshes having non-uniform resolution distributions (Fig. 1) The first mesh is a relatively coarse resolution mesh containing almost 0.13 M surface nodes (CORE). The mesh has a nominal resolution of 1° in most parts of the global ocean, except north of 50° N, where resolution is increased to ca.25 km, and in the equatorial belt, where resolution is increased to 1/3°. The second mesh, HR, has a background resolution comparable in size to the mesh with uniform

1/4°, eddy permitting resolution, with high SSHV and decrease it in regions with low SSHV (Sein et al., 2016).

Results

As a first step of developing a high-resolution FESOM-REcoM2 setup, we performed a high-resolution physical spin-up run for two cycles of JRA55 forcing from 1958 - 2017 using the HR mesh (second cycle is done until the year 1990) for the physical ocean model spin-up. We initialized our model from an existing simulation driven by CORE-II forcing (Large and Yeager, 2009). This is justified given the high computational cost of the high-resolution set-up.

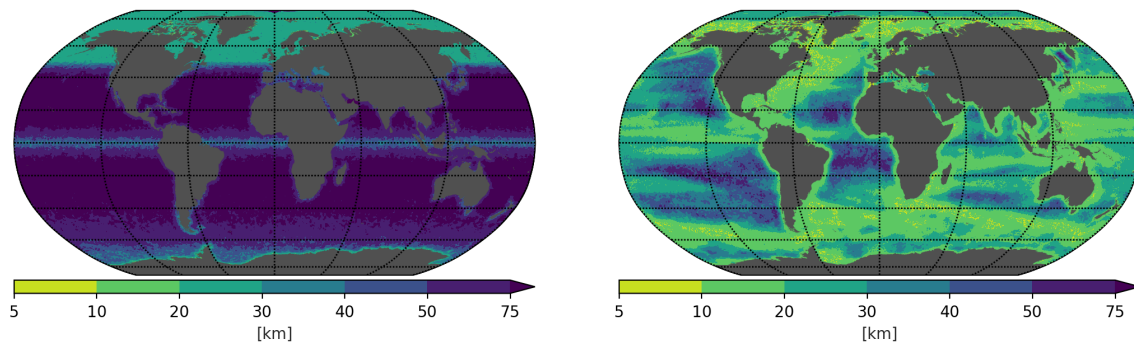


Figure 1: Mesh resolution of the model grids used in this study. CORE (left) and HR (right) that is produced to meet sea surface height in addition to Rossby radius of deformation, respectively. Number of surface nodes: CORE = ~0.13 M, HR = ~1.3 M.

We show here only the results from HR mesh. We compared the spatial distribution of departure from simulated surface and 1000 m temperature and salinity fields to the Polar Science Center Hydrographic Climatology (Steele et al. (2001)) which we chose as the reference. In deep (1000 m) mid-east North Atlantic, there is a strong negative temperature and salinity bias in our HR simulation (Figure 2 bottom left panel). The source of this bias is most likely related to the bathymetric representation of Gibraltar Strait and associated outflow of the warm and salty Mediterranean waters at this depth. This bias could be reduced by increasing the mesh resolution in the strait. Another reason might be the relatively high resolution atmospheric JRA55 forcing which changes the depth and pattern of the recirculated North Atlantic Current. The spatial pattern of the bias and its strength compares to previous FESOM mesh refinement studies (Sein et al., 2016, 2017).

Outlook

We continue our simulations with coupled FESOM-REcoM2 simulation from 1980 to 2017 (38 years) using the HR mesh 1) with constant atmospheric CO₂ concentration to quantify a potential model drift and 2) with an increasing atmospheric CO₂ concentration.

The biogeochemical model fields for the year 1979 from the simulation on the CORE mesh will be interpolated to the HR mesh and be used as initial fields. The physics and biogeochemistry will be run together from 1980 to 2017 which is the time-period for which the observation-based products of Landschützer et al. (2014) and Rödenbeck et al. (2015) exist for comparison. This approach of interpolating biogeochemical fields to a higher resolution grid is also applied in other modelling groups to produce high-resolution ocean biogeochemical model simulations (e.g. Terhaar et al., 2018) due to computational costs of running expensive biogeochemical models in high resolution.

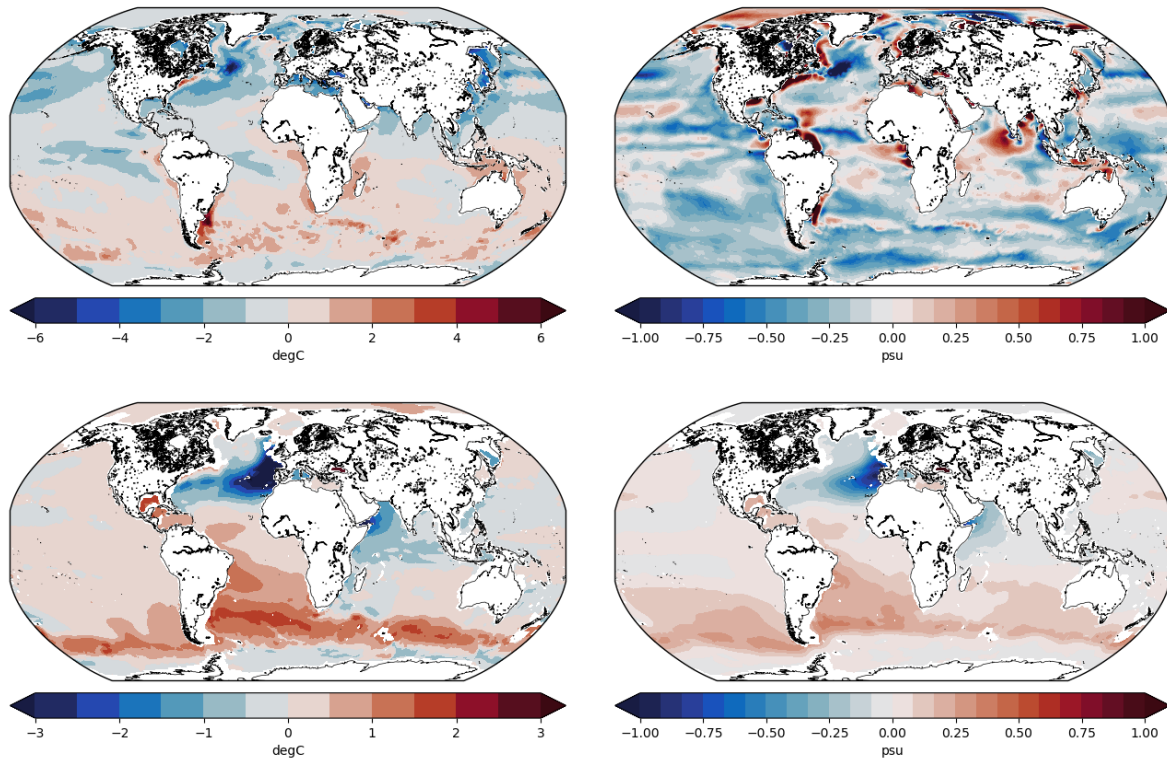


Figure 2: Departure of temperature (top panel) and salinity (bottom panel) simulated with the FESOM HR configuration from the Polar Science Center Hydrographic Climatology (Steele et al. (2001)) at the ocean surface (left) and at intermediate depth (1000 m, right).

References

- Archer, D., H. Kheshgi, and E. Maier-Reimer (1997), Multiple timescales for neutralization of fossil fuel CO₂, *Geophysical Research Letters*, 24, 405–408, doi:10.1029/97GL00168.
- DeVries, T., M. Holzer, and F. Primeau (2017), Recent increase in oceanic carbon uptake driven by weaker upper-ocean overturning, *Nature*, 542(7640), 215, doi:10.1038/nature21068.
- Geider, R. J., MacIntyre, H. L., and Kana, T. M.: A dynamic model of photoadaptation in phytoplankton, *Limnol. Oceanogr.*, 41, 1–15, 1996.
- Geider, R. J., MacIntyre, H. L., and Kana, T. M.: A dynamic regulatory model of phytoplanktonic acclimation to light, nutrients, and temperature, *Limnol. Oceanogr.*, 43, 679–694, doi:10.4319/lo.1998.43.4.0679, 1998.
- Khatiwala, S., F. Primeau, and T. Hall (2009), Reconstruction of the history of anthropogenic CO₂ concentrations in the ocean, *Nature*, 462, 346–349, doi:10.1038/nature08526.
- Landschützer, P., N. Gruber, D. C. E. Bakker, and U. Schuster (2014), Recent variability of the global ocean carbon sink, *Global Biogeochemical Cycles*, 28(9), 927–949, doi:10.1002/2014GB004853.
- Large, W. G., and S. G. Yeager (2009), The global climatology of an interannually varying air–sea flux data set, *Climate Dynamics*, 33(2), 341–364, doi:10.1007/s00382-008-0441-3.
- Le Quéré, C., R. M. Andrew, P. Friedlingstein, S. Sitch, J. Hauck, J. Pongratz, P. A. Pickers, J. I. Korsbakken, G. P. Peters, J. G. Canadell, A. Arneeth, V. K. Arora, L. Barbero, A. Bastos, L. Bopp, F. Chevallier, L. P. Chini, P. Ciais, S. C. Doney, T. Gkritzalis, D. S. Goll, I. Harris, V. Haverd, F. M. Hoffman, M. Hoppema, R. A. Houghton, G. Hurtt, T. Ilyina, A. K. Jain, T. Johannessen, C. D. Jones, E. Kato, R. F. Keeling, K. K. Goldewijk, P. Landschützer, N.

Lefèvre, S. Lienert, Z. Liu, D. Lombardozi, N. Metzl, D. R. Munro, J. E. M. S. Nabel, S. Nakaoka, C. Neill, A. Olsen, T. Ono, P. Patra, A. Peregon, W. Peters, P. Peylin, B. Pfeil, D. Pierrot, B. Poulter, G. Rehder, L. Resplandy, E. Robertson, M. Rocher, C. Rödenbeck, U. Schuster, J. Schwinger, R. Séférian, I. Skjelvan, T. Steinhoff, A. Sutton, P. P. Tans, H. Tian, B. Tilbrook, F. N. Tubiello, I. T. van der Laan-Luijkx, G. R. van der Werf, N. Viovy, A. P. Walker, A. J. Wiltshire, R. Wright, S. Zaehle, and B. Zheng (2018a), Global carbon budget 2018, *Earth System Science Data*, 10(4), 2141–2194, doi:10.5194/essd-10-2141-2018.

Li, H., and T. Ilyina (2018), Current and future decadal trends in the oceanic carbon uptake are dominated by internal variability, *Geophysical Research Letters*, 45(2), 916–925, doi:10.1002/2017GL075370.

McKinley, G. A., D. J. Pilcher, A. R. Fay, K. Lindsay, M. C. Long, and N. S. Lovenduski (2016), Timescales for detection of trends in the ocean carbon sink, *Nature*, 530(7591), 469,

Rödenbeck, C., D. C. E. Bakker, N. Metzl, A. Olsen, C. Sabine, N. Cassar, F. Reum, R. F. Keeling, and M. Heimann (2014), Interannual sea-air CO₂ flux variability from an observation-driven ocean mixed-layer scheme, *Biogeosciences*, 11(17), 4599–4613, doi:10.5194/bg-11-4599-2014.

Sein, D. V., S. Danilov, A. Biastoch, J. V. Durgadoo, D. Sidorenko, S. Harig, and Q. Wang (2016), Designing variable ocean model resolution based on the observed ocean variability, *Journal of Advances in Modeling Earth Systems*, 8(2), 904–916, doi:10.1002/2016MS000650.

Sein, D. V., N. V. Koldunov, S. Danilov, Q. Wang, D. Sidorenko, I. Fast, T. Rackow, W. Cabos, and T. Jung (2017), Ocean modeling on a mesh with resolution following the local Rossby radius, *Journal of Advances in Modeling Earth Systems*, 9(7), 2601–2614, doi:10.1002/2017MS001099.

Steele, M., R. Morley, and W. Ermold (2001), Phc: A global ocean hydrography with a high-quality arctic ocean, *Journal of Climate*, 14(9), 2079–2087, doi:10.1029/2006GL026152, 2001.

Terhaar, J., J. C. Orr, M. Gehlen, C. Ethé, and L. Bopp (2018), Model constraints on the anthropogenic carbon budget of the Arctic Ocean, *Biogeosciences Discussions*, 2018, 1–36, doi:10.5194/bg-2018-283.

Wang, Q., Danilov, S., Sidorenko, D., Timmermann, R., Wekerle, C., Wang, X., Jung, T., and Schröter, J.: The Finite Element Sea Ice–Ocean Model (FESOM) v.1.4: formulation of an ocean general circulation model, *Geosci. Model Dev.*, 7, 663–693, doi:10.5194/gmd-7-663-2014, 2014.

Publications and Presentations

Biogeochemical simulations to be started, no presentation of results with physics only yet.

6.22 *hbk00076*: Simulation der letzten glazialen Termination mit einem gekoppelten Klima-Eisschild-Modell

| | |
|-------------------------|--|
| HLRN-Projektkenung: | hb00076 |
| Laufzeit: | II/2019 – I/2020 |
| Projektleiter: | Prof. Michael Schulz |
| Projektbearbeiter: | Dr. Matthias Prange |
| Institut / Einrichtung: | MARUM – Zentrum für Marine Umweltwissenschaften, Universität Bremen |

Überblick

Die letzte eiszeitliche Termination (21.000-11.000 Jahre vor heute) stellt eine Schlüsselperiode für unser Verständnis von globalen Klimaveränderungen dar. Diese Phase ist das paläoklimatologisch bestdokumentierte Beispiel für eine massive Reorganisation des Erd- und Klimasystems, bei der große Eismassen vom amerikanischen und eurasischen Kontinent, aber auch von der Antarktis, abschmolzen und sich der globale Meeresspiegel infolgedessen um rund 120 m hob. Globale Temperaturen stiegen im Jahresmittel um mehrere Grad Celsius und der atmosphärische Kohlendioxid-Gehalt nahm um fast 100 ppmv zu. Dieser Übergang vom letzten glazialen Maximum (LGM) in die jetzige Zwischeneiszeit (Interglazial) geschah jedoch nicht gleichmäßig, sondern war vielmehr durch mehrere abrupte Teilübergänge gekennzeichnet. Dabei wurde die extreme Kaltphase in nördlichen Breiten des Heinrich-Stadials 1 (ca. 18.000-14.700 Jahre vor heute) von der wärmeren Periode des Bölling-Alleröd-Interstadials (ca. 14.700-12.800 Jahre vor heute) abgelöst, bevor es mit dem Jüngeren-Dryas-Stadial (12.800-11.700 vor heute) vorübergehend wieder kälter wurde. Schmelzwassereinträge von den sich zurückziehenden Eisschilden in den Ozean und deren Effekt auf die Tiefenwasserbildung und Tiefenzirkulation werden für diese Klimaschwankungen mitverantwortlich gemacht. Gleichwohl ist das genaue zeitliche Zusammenspiel zwischen Eiszerfall und Änderungen der Ozeanzirkulation noch immer unverstanden.

Bislang wurden Simulationen der Termination mit ungekoppelten Eisschildmodellen (angetrieben durch vorgeschriebene Klimatologien und statistischen Modellen der Atmosphäre), Eisschildmodellen gekoppelt mit einfachen Energiebilanzmodellen der Atmosphäre oder Erdsystemmodellen mittlerer Komplexität durchgeführt. Wichtige Wechselwirkungsprozesse zwischen Ozean und Eisschilden, aber auch zwischen Eisschilden und Atmosphärenzirkulation konnten somit nicht simuliert werden. Zur Untersuchung der relevanten Prozesse, die zum Zerfall der eiszeitlichen Eisschilde führen und dem resultierenden Einfluss auf das Klimasystem (z. B. mögliches Auslösen von Stadialen), verwenden wir in diesem Projekt daher das komplexe Klimamodell (allgemeines Zirkulationsmodell) CESM, gekoppelt an ein dynamisch-thermodynamische Eisschildmodell. Ein interaktives Mineralstaubmodul, das im Klimamodell implementiert ist, erlaubt den Vergleich mit Staubdaten aus Eisbohrkernen. Dies kann einerseits zur Validierung der Simulation verwendet werden, woraus sich wichtige Rückschlüsse über vergangene atmosphärische Zirkulationsänderungen ableiten lassen können. Andererseits wirkt der interaktive Staub auf die atmosphärische Strahlungsbilanz zurück. Die Untersuchung der Termination mit gekoppelten Eisschilden erfordert zwangsläufig lange transiente Simulationen (im Gegensatz zu kostengünstigeren Zeitscheiben-Klima-Experimenten, die von Gleichgewichtszuständen ausgehen und bei denen die Randbedingungen konstant bleiben). Zur Einsparung von Rechenzeit verwenden wir für die Spin-up- und Tuning-Phase zunächst

eine asynchrone Koppelungstechnik zwischen Klima- und Eisschildmodell. Hierbei kann das im Vergleich zum Eismodell wesentlich rechenzeitaufwändigere Klimamodell beschleunigt gerechnet werden.

Das Projekt ist Teil der Arbeitspakete WP1.1 (Coupling of ice sheet models with AOGCMs) und WP1.3 (Long transient simulations) der BMBF-finanzierten nationalen Klimamodellierungsinitiative „PalMod – From the Last Interglacial to the Anthropocene“. Das übergeordnete Ziel dieser Arbeitspakete ist die Simulation der letzten Termination mit Hilfe gekoppelter Klima-Eisschild-Modelle angetrieben durch kontinuierliche Änderungen in Treibhausgaskonzentrationen und Erdbitalparametern. In einer späteren Projektphase soll das mit Hilfe von Paläo-Proxydaten validierte gekoppelte Modell dann in die Zukunft gerechnet werden, um verlässlichere Aussagen über die zukünftige Entwicklung der Eisschilde und des globalen Meeresspiegels machen zu können.

Das verwendete Klimamodell CESM1.2 wird mit einer horizontalen Auflösung von 2° für das Atmosphären-/Landmodellgitter betrieben, während das Ozean-/Meereisgitter eine räumlich variable Gitterweite von ca. 1° in zonaler und bis zu $0,3^\circ$ in meridionaler Richtung besitzt. Die vertikale Darstellung des Atmosphärenmodells umfasst 30 Schichten, der Ozean wird mit 60 Niveaus in der Vertikalen diskretisiert. Das Eisschild-Modell SICOPOLIS wird für beide Hemisphären mit einer Auflösung von 20 km integriert.

Erste Ergebnisse

Erste transiente Klima-Eisschild-Simulationen der letzten Deglaziation wurden zur Untersuchung der Sensitivität des gekoppelten Systems bzgl. bestimmter Modellparameter oder Störungen durchgeführt. Beispielhaft zeigt Abb. 1 „Schnappschüsse“ des antarktischen Eisschildes aus voll gekoppelten transienten Simulationen, in denen Wassertemperaturen im Südpolarmeer um 0.5°C bzw. 1°C künstlich erhöht wurden, um die Sensitivität des basalen Schmelzens und den damit zusammenhängenden Eisschild-Rückgang zu untersuchen.

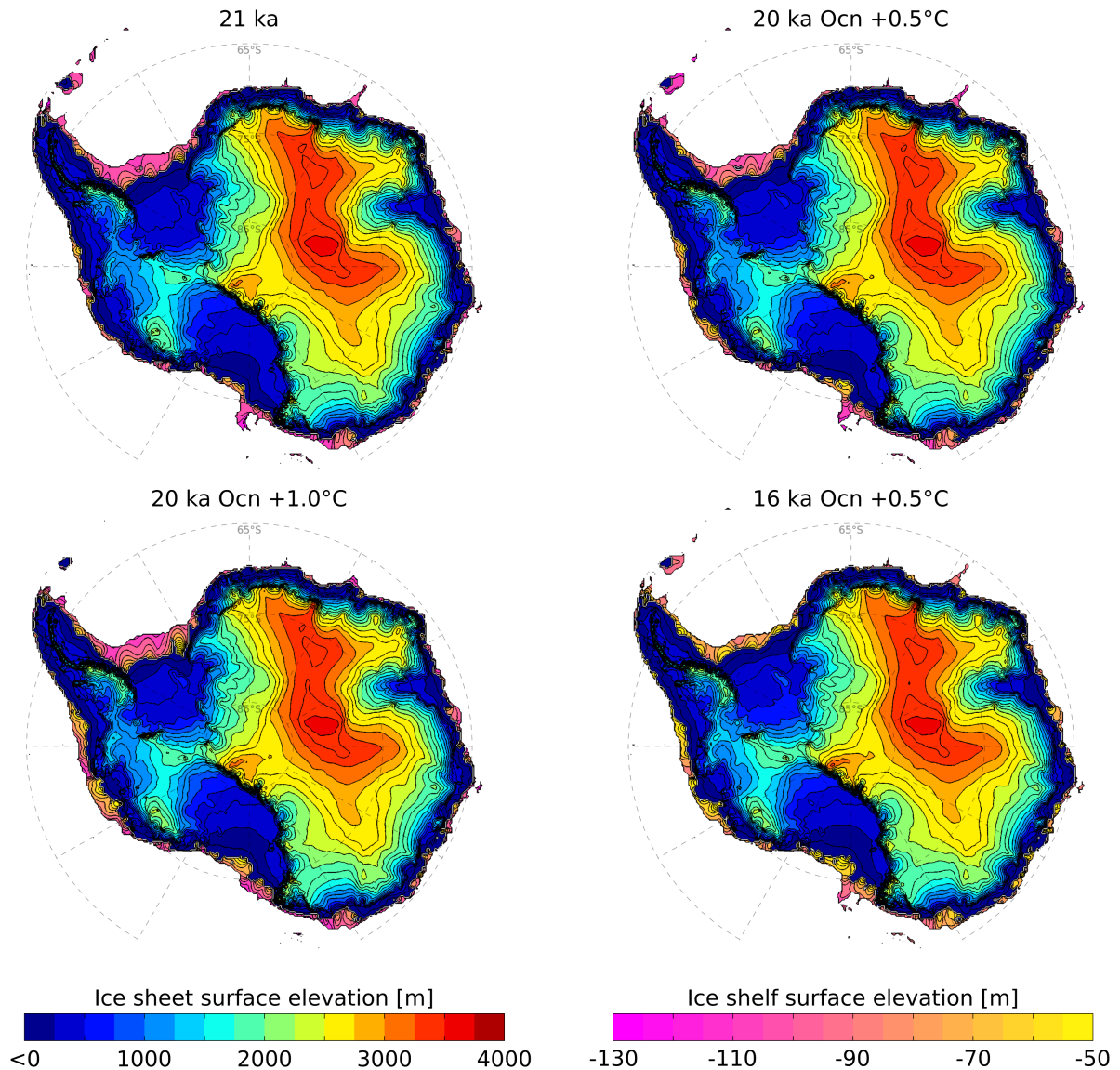


Abbildung 1: Deglaziale Entwicklung des antarktischen Eisschildes im voll gekoppelten Klima-Eisschild-Modell zu verschiedenen Zeitpunkten (ka = 1000 Jahre vor heute) und mit verschiedenen Störungen der Wassertemperatur im Südpolarmeer (+0.5°C und +1°C).

Publikationen

1. Bakker, P., I. Rogozhina, U. Merkel, **M. Prange**, Hypersensitivity of glacial temperatures in Siberia. *Climate of the Past*, **16**, 371-386, doi:10.5194/cp-16-371-2020 (2020).

6.23 *hbp00029*: Carrier dynamics and optical properties of transition metal dichalcogenides

| | |
|-------------------------|--|
| HLRN-Projektkenung: | hbp0029 |
| Laufzeit: | IV/2015 – IV/2020 |
| Projektleiter: | Dr. rer. nat. Michael Lorke Prof. Dr. Frank Jahnke |
| Projektbearbeiter: | Dr. rer. nat. Alexander Steinhoff Dr. rer. nat. Matthias Florian M. Sc. Daniel Erben |
| Institut / Einrichtung: | Institut für Theoretische Physik, Universität Bremen |

Introduction

Van der Waals heterostructures (vdW-HS) as artificial solids composed of atomically thin materials like transition metal dichalcogenides (TMDs), graphene or hexagonal boron nitride (hBN) are today one of the busiest research areas of condensed matter physics.

Already in the single-layer limit, TMD semiconductors are ideal platforms for studying a broad range of electronic, optoelectronic, and quantum phenomena as a function of charge carrier density due to strong Coulombic interactions. The configuration into vdW-HS allows to combine different semiconducting, (semi-)metallic and isolating materials, which yields a manifold of options for the rational design of devices.

Charge carrier dynamics and optical processes in vdW-HS are prone to dielectric screening from adjacent layers as well as ultra-fast charge separation between layers. These aspects of vdW-HS have been investigated in this project using state-of-the-art many-body methods.

Results

Optical generation of high carrier densities in 2D semiconductor heterobilayers

Two-dimensional (2D) TMDs are ideal for studying highly correlated quantum phenomena as a function of charge carrier density such as charge densitywaves and superconductivity. These phenomena are realized at high charge carrier densities ($\sim 10^{14} \text{ cm}^{-2}$) achievable for example with ionic liquidgating. Alternatively, in TMD type-II heterobilayers, photoexcited electrons and holes separate on femtosecond time scales to form oppositely charged monolayers. Due to the long radiative lifetimes of spatially separated electrons and holes, these systems offer a unique opportunity to control high carrier densities in individual 2D monolayers.

In publication [1], photoluminescence spectroscopy and time-resolved reflectance spectroscopy has been used to demonstrate the optically driven Mott transition from a gas of interlayer excitons to charge-separated e/h plasmas in $\text{aWSe}_2 / \text{MoSe}_2$ heterobilayer. The achieved carrier density is as high as $4 \times 10^{14} \text{ cm}^{-2}$, two orders of magnitude above the Mott density. The experimental findings are supported by many-body calculations that have been carried out in the scope of HLRN project hbp0029.

In particular, we have calculated the optical susceptibility of a photoexcited $\text{WSe}_2 / \text{MoSe}_2$ heterobilayer by solving the semiconductor Bloch equations (SBE) in the screened-exchange-Coulomb-hole approximation assuming a quasi-equilibrium distribution of electrons and holes at a given carrier density. The SBE are based on a bandstructure in effective mass approximation including the various K, Q and Γ valleys as well as their time-reversal

counterparts. Coulomb interaction matrix elements are obtained from a macroscopic dielectric function together with form factors that describe the spatial separation of electrons and holes. From the optical susceptibility, reflectance and absorptance spectra are derived taking into account the experimental sample geometry.

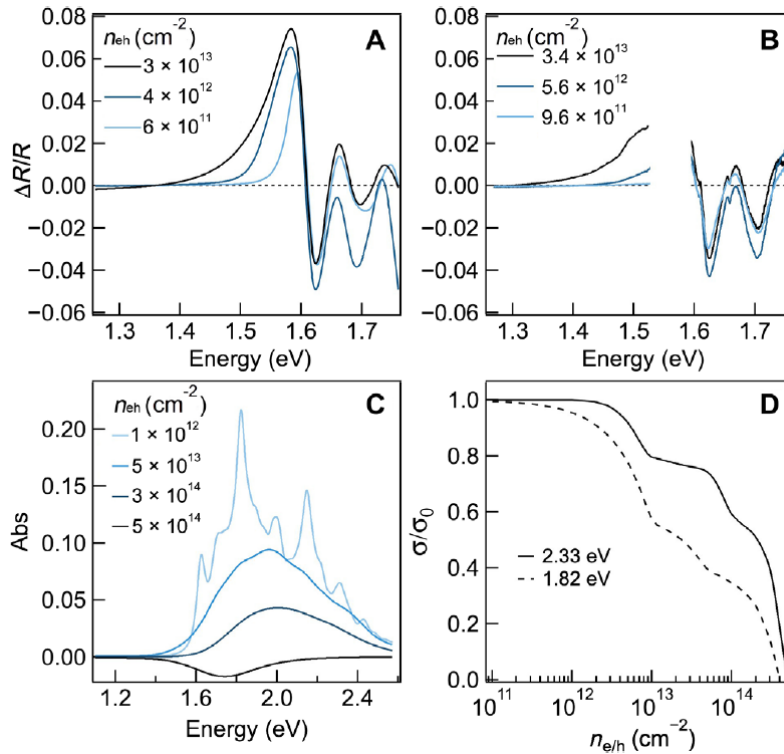


Figure 1: Calculated optical spectra of the WSe₂/MoSe₂ heterobilayer.

(a) Simulated reflectance spectra from theoretical optical susceptibility and experimental sample geometry at the indicated excitation densities ($n_{eh} = 6 \times 10^{11}$ to $3 \times 10^{13} \text{ cm}^{-2}$).

(b) Experimental reflectance spectra at initial excitation densities of $n_0 = 9.6 \times 10^{11}$ to $3.4 \times 10^{13} \text{ cm}^{-2}$.

(c) Calculated optical absorptance spectra at $n_{eh} = 1 \times 10^{11}$ to $5 \times 10^{14} \text{ cm}^{-2}$.

(d) Calculated relative optical absorptance as a function of n_{eh} at two photon energies used in the experiments.

Fig. 1a shows simulated transient reflectance spectra at excitation densities $n_0 = 6 \times 10^{11}$, 4×10^{12} , and $3 \times 10^{13} \text{ cm}^{-2}$ obtained from the theoretical optical susceptibility and the experimental sample geometry. Also shown as comparison are experimental transient reflectance spectra at similar density values, see Fig. 1b. The simulations and experimental spectra are in excellent agreement, including main features of intralayer exciton bleaching for all excitation densities, the broad induced absorption feature above the Mott density, and stimulated emission near the renormalized bandgap at $\sim 1.3 \text{ eV}$. This agreement provides strong support for the conclusion on Mott transition from the interlayer exciton to charge-separated e/h plasmas and helps calibrating the carrier density in the CW measurements also reported in publication [1]. Figure 1c shows calculated absorptance spectra at selected n_{eh} values. By determining at which n_{eh} excitonic absorption resonances becomes bleached, we find $n_{Mott} = 3 \times 10^{12} \text{ cm}^{-2}$. More specifically, we follow excitonic absorption where exciton features gradually fade through broadening from a clear peak to transparency and eventually to gain. Below n_{Mott} , the presence of excitons significantly reduces scattering. There is an accelerated scattering-induced broadening after excitons cease to exist above n_{Mott} , which also leaves a signature in increased PL linewidth.

In addition to revealing the Mott threshold from the disappearance of sharp excitonic features, the theoretical absorption spectra show the decrease in oscillator strength with increasing n_{eh} , as expected from Pauli blocking and screening effects. Optical transparency is reached at $n_{eh} \sim 4 \times 10^{14} \text{ cm}^{-2}$, above which stimulated emission dominates.

Dynamical screening effects of substrate phonons on two-dimensional excitons

Atomically thin materials are exceedingly susceptible to their dielectric environment. For TMDs, samples are often encapsulated in hBN to improve the sample quality. Beyond frequently discussed static screening effects, polar substrate materials such as sapphire, SiO₂, and hBN host optical phonons in the infrared spectral range. These are expected to add a significant frequency-dependent dielectric response felt by the encapsulated material.

In publication [2], we provide a description for the coupling of TMD charge carriers to substrate phonons. Our approach uses a mapping of the macroscopic dielectric function of the vdW-HS to an effective Fröhlich Hamiltonian. The Hamiltonian captures the microscopic parameters that characterize both, the heterostructure geometry and the properties of substrate TO phonons as extracted from experiments. Thereby, we transfer the dynamical, frequency-dependent behavior of the substrate dielectric function to a carrier-boson interaction on the level of second quantization. This puts the coupling to substrate phonons on an equal footing with the coupling to intrinsic 2D phonons and introduces additional scattering channels for the 2D excitons. We then use the augmented coupling Hamiltonian in an equation-of-motion (EOM) approach to investigate the impact on 2D excitons.

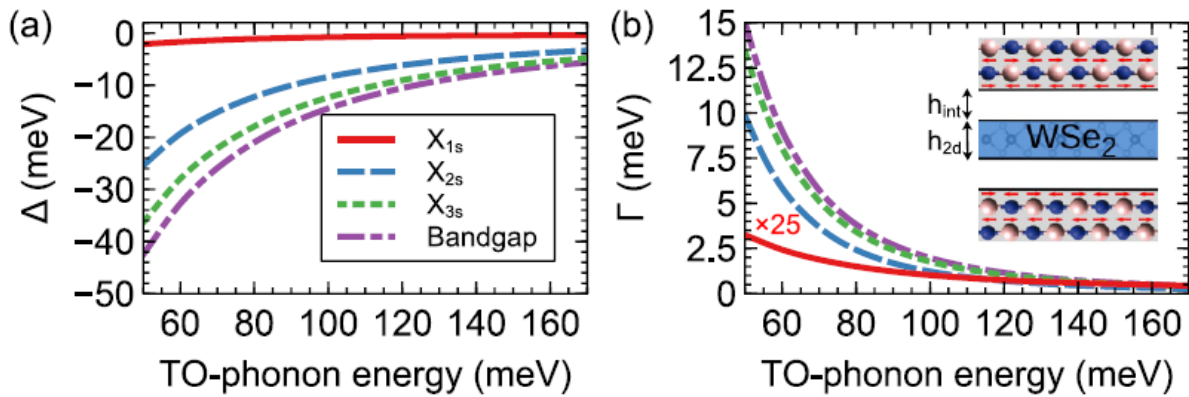


Figure 2: Substrate-phonon-induced renormalization of 2D excitons. Energy renormalizations (a) and linewidth (b) of 1s, 2s, and 3s excitons in WSe₂ as well as the band-gap transition depending on the energy of the substrate TO phonon. Both quantities exhibit a characteristic inverse power-law dependence. Note that the binding energy reduction (difference to band gap) is strongest for the 1s exciton. The inset shows a schematic of a TMD monolayer coupling to in-plane optical phonons in the surrounding dielectric material, which is detached by an interlayer gap. The results are obtained for T = 300 K.

For the coupling between 2D carriers in WSe₂ and environmental phonons, the band structure around the K point is approximated by an effective-mass model. We limit carrier-phonon scattering to intravalley processes neglecting coupling to dark excitons that involve large momentum transfer q . This is justified by the $1/q$ -scaling behavior of the Fröhlich-type coupling considered here. The heterostructure geometry is determined by the 2D layer thickness h_{2d} and the interlayer distance h_{int} , while the dielectric environment enters the calculation via the high-frequency dielectric constant of hBN along with the oscillator strength of the low-energy hBN phonon. Exciton line shifts and broadenings due to the interaction with substrate phonons are shown in Fig. 2, as obtained from real and imaginary parts of the exciton self-energy. The band gap is defined as the lowest unbound (positive-energy) state from the Wannier equation. The substrate phonon energy is varied between 50 and 170 meV to include typical phonon energies of hBN and SiO₂. We find a characteristic inverse power-law dependence of renormalization effects on the substrate-phonon energy. Scattering is dominated by phonon

emission and nonresonant scattering processes. Since for higher exciton states possible final states are energetically more dense, renormalization effects are increasingly efficient. Comparing the energy renormalization for bound exciton states with the bandgap shift, we find an effective reduction of exciton binding energies due to coupling to substrate phonons.

In conclusion, environmental phonons cause polaron effects well known for carrier-phonon interaction intrinsic to the material itself. For the specific situation of hBN-encapsulated WSe₂ we find that the dynamical dielectric response of the environment reduces exciton binding energies by tens of meV depending on the exciton quantum number.

Site-selectively generated photon emitters in monolayer MoS₂ via local helium ion irradiation

Quantum light sources in solid-state systems are of major interest as a basic ingredient for integrated quantum photonic technologies. The ability to tailor quantum emitters via site selective defect engineering is essential for realizing scalable architectures. However, a major difficulty is that defects need to be controllably positioned within the material.

In publication [3], this challenge has been overcome by controllably irradiating monolayer MoS₂ using a sub-nm focused helium ion beam to deterministically create defects. Subsequent encapsulation of the ion exposed MoS₂ flake with high-quality hBN revealed spectrally narrow emission lines that produced photons in the visible spectral range as shown in Fig. 3a. The experimental findings are supported by ab-initio calculations where these emission lines are interpreted as stemming from the recombination of highly localized electron-hole complexes at defect states generated by the local helium ion exposure.

MoS₂ exhibits several defects, most prominently single sulfur vacancies and single molybdenum vacancies. So far, sulphur vacancies have not been demonstrated to be optically active, because they are very likely to be passivated with oxygen, although they are ubiquitous in exfoliated, unexposed MoS₂. Thus, we concentrated on molybdenum vacancies V_{Mo} . Figure 3b–e show the ab-initio calculated density of states (DOS) for a neutral V_{Mo}^0 , as well as a single, double and triple negatively charged molybdenum vacancy (V_{Mo}^{1-} , V_{Mo}^{2-} , and V_{Mo}^{3-}). We found that all presented states are stable and relaxed within our DFT framework.

Since the detuning from the neutral A exciton emission (ΔEL) is significantly smaller than the quasi particle band gap in MoS₂, we assume that the Fermi energy is close to the conduction band minimum (CBM). The experimentally observed sharp emission lines are interpreted as resulting from excitons that also involve particle-hole excitations from the defect state orbitals.

In conclusion, this new approach to deterministically write optically active defect states in a single transition metal dichalcogenide layer provides a platform for realizing exotic many-body systems, including coupled single-photon sources and interacting exciton lattices that may allow the exploration of Hubbard physics.

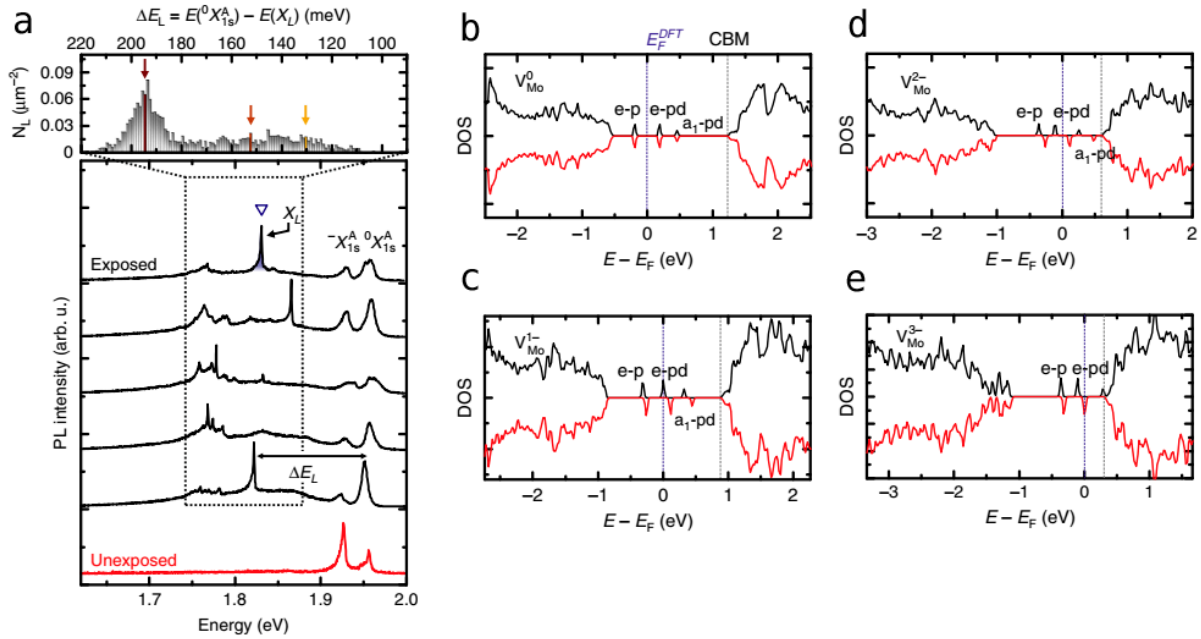


Figure 3: Deterministically induced defect emitters in atomically thin MoS₂ realized by focused helium ions. (a) Bottom panel: typical experimental low-temperature (10 K) μ -PL spectra of the exposed (black) and unexposed (red) hBN/MoS₂/hBN heterostructure. The spectra of exposed MoS₂ feature emission from single emission lines XL (open triangle) at lower energies. Top panel: a histogram of the emission energies detuned by ΔE_L below the neutral A exciton emission. (b-e) DFT calculated spin-up (black) and spin-down (red) density of states (DOS) of the neutral V_{Mo}^0 , single negatively V_{Mo}^{1-} , double negatively V_{Mo}^{2-} , and triple negatively charged V_{Mo}^{3-} molybdenum vacancy. The DOS of V_{Mo}^0 shows doublet (e-p, e-pd) and singlet (a1-pd) defect states inside the band gap. The more electrons are added to the vacancy the closer the defect states and the DFT computed Fermilevel energy E_F^{DFT} shift to the conduction band minimum (CBM) because of the on-site Coulomb repulsion.

Outlook

Ongoing work is concerned with the nonequilibrium dynamics of excitons in TMD heterostructures at high excitation density and the corresponding exciton-exciton interaction effects. We are going to extend our research towards twisted heterobilayers, which attract considerable attention recently due to completely new physics arising from the experimentally controllable twist angle. Examples are spatial superstructures due to moiré-like effects and correlated phenomena in the flat bands of magic-angle bilayer graphene.

Publications

1. J. Wang, J. Ardelean, Y. Bai, A. Steinhoff, M. Florian, F. Jahnke, X. Xu, M. Kira, J. Hone, and X.-Y. Zhu, Optical generation of high carrier densities in 2D semiconductor heterobilayers, *Science Advances* **5**, eaax0145 (2019)
2. A. Steinhoff, M. Florian, and F. Jahnke, Dynamical screening effects of substrate phonons on two-dimensional excitons, *Physical Review B* **101**, 045411 (2020)
3. J. Klein, M. Lorke, M. Florian, F. Sigger, L. Sigl, S. Rey, J. Wierzbowski, J. Cerne, K. Müller, E. Mitterreiter, P. Zimmermann, T. Taniguchi, K. Watanabe, U. Wurstbauer, M. Kaniber, M. Knap, R. Schmidt, J.J. Finley and A.W. Holleitner, Site-selectively generated photon emitters in monolayer MoS₂ via local helium ion irradiation, *Nature Communications* **10**, 275 (2019)

6.24 *hbp0041*: Multi-messenger Signals from Compact Objects

| | |
|--------------------|--|
| HLRNProject ID: | hb00041 |
| Run time: | I/2018 – II/2020 |
| Project Leader: | Prof. Claus Lämmerzahl |
| ProjectScientists: | Prof. Stephan Rosswog |
| Affiliation: | ZARM, University of Bremen, Am Fallturm, 28359 Bremen, Germany |

Overview

The recent detection of a binary black hole merger has heralded the long-awaited era of gravitational wave (GW) astronomy. This watershed event confirmed a 100-year-old prediction of Einstein's General Theory of Relativity; even more importantly, it opened up a completely new channel to observe the Universe. GW astronomy allows to probe how the strongest gravitational fields warp space-time, how ultra-gravity binary stars contribute to the heaviest elements in the cosmos, how such binary systems form and, eventually, how their mergers can be used to probe of the expansion history of the Universe. All these exciting prospects, however, hinge on the additional detection of electromagnetic (EM) counterparts of GW sources. A coincident detection of both GWs and EM waves had been a scientific dream for decades.

This dream came true on August 17, 2017: the LIGO/Virgo detectors recorded for the first time the GWs from a binary neutron star merger and subsequently telescopes around the world detected the event all across the EM spectrum (Abbott et al. 2017). This first GW+EM observation proved that neutron star mergers are indeed strong sources of gravitational waves, that they produce short gamma ray bursts and are a major cosmic factory for the heaviest elements (Rosswog et al. 1999, Freiburghaus et al. 1999). Moreover, the subtle tidal imprint on the GW signal constrained the behaviour of nuclear matter at high densities and the arrival time differences of GWs and photons demonstrated that both propagate at the same speed with a relative precision of 10^{-15} . The combined detection also allowed for an entirely new approach to probe the expansion of the Universe. For all these reasons, this first "multi-messenger" detection of a binary neutron star merger was celebrated by *Science Magazine* as "2017 Breakthrough of the Year".

Theoretically predicting observable signatures of compact objects is the main topic of this HLRN project.

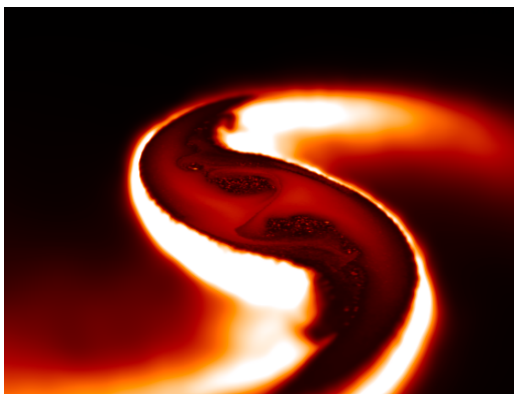


Figure 1: Simulation of two merging neutron stars (only matter below orbital plane is visible). At the interface between the neutron stars a Kelvin-Helmholtz instability is visible.

Results

Our project at the HLRN aims at studying by means of computer simulations various signatures produced by neutron stars and black holes. Some of the recent results are summarized below.

Tidal disruptions of stars by spinning (“Kerr-“) black holes

We have performed the first systematic study of how the black hole spin impacts on the tidal disruption of a star (Gafton and Rosswog 2019). Fig. 2 shows the disruption of a solar-type star by a massive black hole (10^6 solar masses). The disrupted stellar matter for the case of non-spinning (“Schwarzschild”) black holes is shown in the first line, spinning (“Kerr”) black holes both for prograde spins are shown in the second line and retrograde spins in the third line.

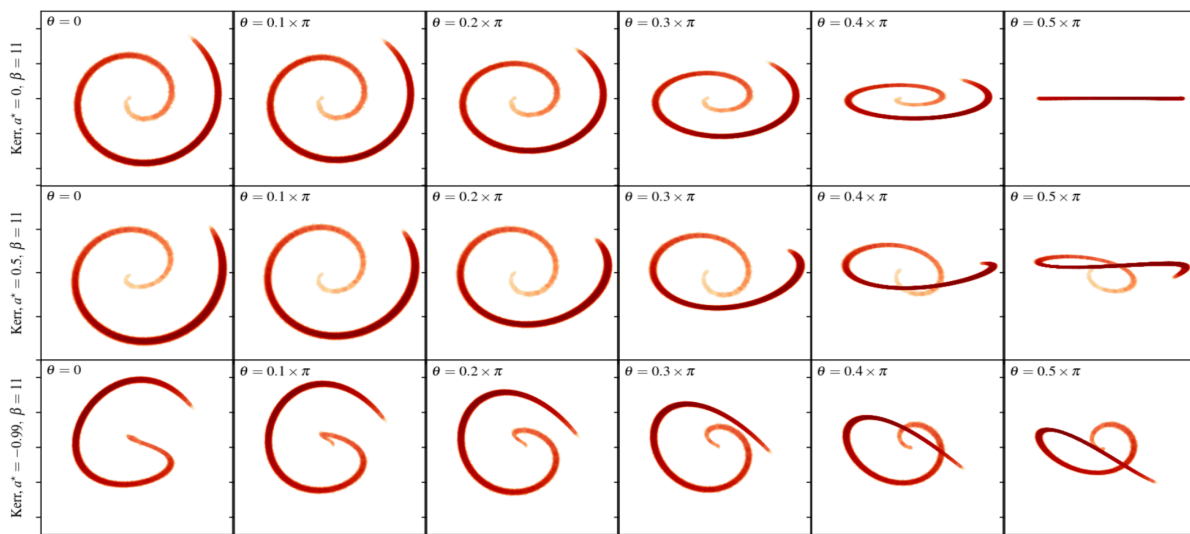


Figure 2: Tidal disruption of a solar-type star by a massive, spinning black hole (Gafton and Rosswog 2019).

The last year was also dedicated to a fair amount of development efforts. In particular, we have developed a novel hydrodynamics code called MAGMA2 (Rosswog 2020a,b) and new neutrino treatment for neutron star mergers (Gizzi et al. 2019) which we will briefly describe below.

MAGMA2

This new code is fully Lagrangian and solves the equations of ideal hydrodynamics by means of freely moving particles. Formally, MAGMA2 is a “Smoothed Particle Hydrodynamics” (SPH) code, but we have developed many non-standard ingredients that strongly enhance the accuracy with respect to standard SPH-approaches. The novel elements include

- the use of high-order kernels for density and gradient calculations
- matrix inversion techniques for accurate gradients
- techniques that are borrowed from Volume Methods such as reconstruction and slope-limiting; rather than in a Riemann solver these techniques are used in calculating the artificial viscosity tensor; these techniques essentially get rid of spurious effects that otherwise often plague artificial viscosity methods.
- A novel scheme to steer where dissipation needs to be applied; in this scheme the entropy evolution of every single particle is monitored and the amount of non-conservation determines how much dissipation is applied.

MAGMA2 has just been developed and will further be extended to special and general relativity. The HLRN resources have been used to perform several hundreds of test and benchmark calculations in which MAGMA2 has delivered excellent results. As an example, we show in Fig. 1, tests of a Rayleigh-Taylor instability which is a challenge for traditional SPH codes. This and many more tests are described in detail in the MAGMA2 paper (Rosswog 2020a).

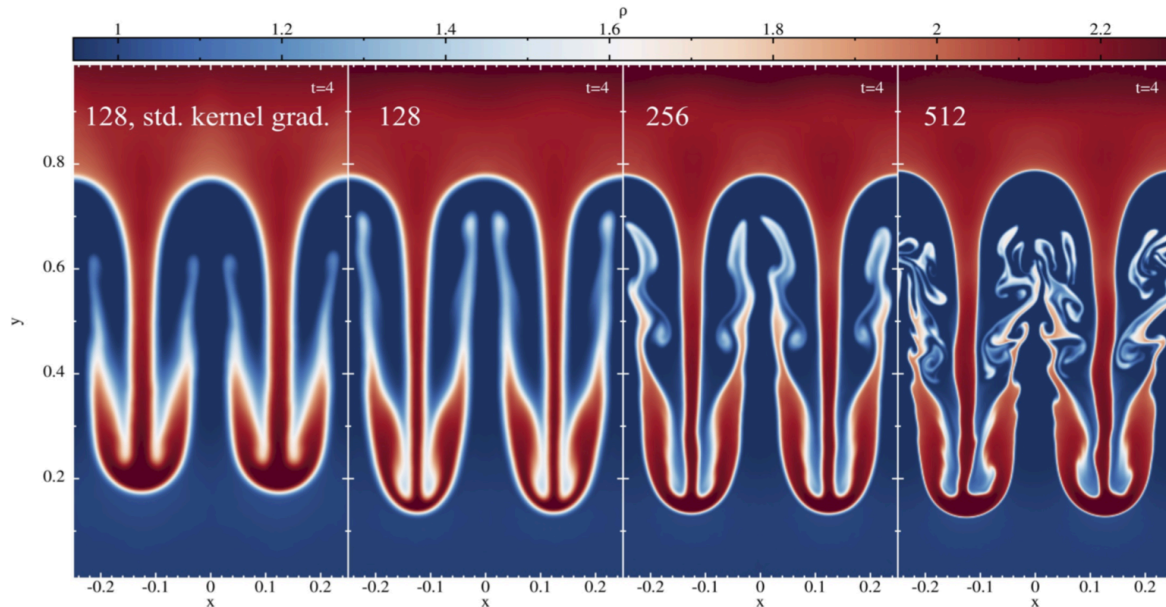


Figure 2: Simulation of a Rayleigh-Taylor instability with the new code MAGMA2 (Rosswog 2020a).

A three-dimensional Advanced Spectral Leakage Scheme for neutron star mergers

Neutrinos play a crucial role in the merger of two neutron stars: they cool the merger remnant and together with electron- and positron captures they can change the neutron-to-proton ratio of the remnant matter. This is a crucial quantity for ejected material, since it determines which heavy elements form and this, in turn, determines the electromagnetic signal from a neutron star merger. This signal is detectable and carries crucial information that is complementary to the one contained in the gravitational wave signal. Treating neutrinos in a merger simulation is very difficult: the inner regions of the remnant are completely opaque, the outer ones completely transparent and in between is a difficult-to-handle semi-transparent regime. Ideally, one should solve the neutrino Boltzmann equation, but this is computationally not feasible.

Therefore, reliable but approximate neutrino transport methods are needed. In our group a novel such approximate neutrino transport method has been developed (Gizzi et al. 2019) that is currently being implemented into MAGMA2 and will be heavily used in future simulations of neutron star mergers

Outlook

Future simulations will make ample use of the newly developed tools. We will in particular enrich the MAGMA2 code with new physics modules, and in particular with the new neutrino treatment scheme. This will in particular allow us to address the of neutrino-driven winds from neutron star mergers and the electromagnetic signatures that they produce.

Publications (selection)

1. S. Ascenzi et al., *A luminosity for kilonovae based on short gamma-ray burst afterglows*, MNRAS 486, 672 (2019)
2. E. Gafton, S. Rosswog, *Tidal disruptions of stars by rotating black holes: effects of spin and impact parameter*, MNRAS, 487, 4790 (2019)
3. D. Gizzi et al., *A multidimensional implementation of the Advanced Spectral neutrino Leakage scheme*, MNRAS, 490, 4211 (2019)
4. S. Rosswog, *The Lagrangian hydrodynamics code MAGMA2*; submitted to MNRAS; arXiv:191113093R (2020a)
5. S. Rosswog, *A simple, entropy-based dissipation trigger for SPH*; submitted to ApJ; arXiv:191201095R (2020b)

Presentations (selection)

1. S. Rosswog, *Neutron star mergers as sources for heavy elements*, Plenary talk, Mendeleev conference, 150 Years of the Periodic Table, St. Petersburg, Russia, Sept. 11, 2019
2. S. Rosswog, *From merger to electromagnetic emission*, Microphysics in computational relativistic Astrophysics, Jena, Germany, August 12, 2019
3. *Multi-messenger astrophysics with neutron star mergers*; Gordon Conference for Nuclear Chemistry, New London, USA, June 20, 2019
4. S. Rosswog, *Heavy Elements and electromagnetic transients from neutron star mergers*, Royal Society Meeting, London, May 11, 2018
5. S. Rosswog, *Neutron star binary simulations*, 10th Sackler Conference in Theoretical Astrophysics, Harvard, Cambridge, USA, May 07, 2018

References

- Abbott et al., ApJL 848, L12 (2017)
Rosswog et al., A&A 341, 499 (1999)
Freiburghaus, Rosswog, Thielemann, ApJ 525, L121 (1999)

6.25 *hbp00045*: Non-local manipulation of correlation effects in 2D Transition Metal Dichalcogenides

| | |
|---------------------|---|
| HLRN Project ID: | hbp00045 |
| Run Time: | II/2017 – II/2019 |
| Project Leader: | Prof. Dr. T. Wehling |
| Project Scientists: | C. Steinke, J. Berges, N. Witt, Dr. E. Kamil |
| Affiliation: | Institut für Theoretische Physik Bremen Center for Computational Materials Science Universität Bremen |

Overview

At about the time when this project was started, theoretical [1] and experimental works [2] had introduced the concept of a novel type of heterojunctions of two-dimensional (2D) materials. It is based on the idea that the Coulomb interaction in a 2D layer can be manipulated via laterally structured substrates as depicted in Fig. 1. These so-called *Coulomb-engineered* heterostructures show spatial property changes, such as different band gaps, within an otherwise homogeneous monolayer.

To predict suitable 2D materials for practical applications, a profound theoretical insight into the electronic processes is necessary. By means of material-realistic models based on *ab initio* calculations, we studied semiconducting transition metal dichalcogenides (TMDCs) placed in different dielectric environments. From this, we wanted to identify candidates for optical Coulomb engineering in this material class. We found significant band-gap reductions with increasing external screening for all investigated materials. Furthermore, we studied the internal limits of the length scale of possible band-gap transitions showing that possible interface regions can be on the order of a few unit cells.

As all real materials contain structural defects that change the material's physical and chemical properties, a profound understanding of their influence is necessary. With this knowledge, the application of defect engineering becomes accessible to specifically control and modify the properties of a material. In 2D materials, especially TMDCs, recent research on defect engineering [3] demonstrates that defects can alter, e.g., electronic structures, magnetic behavior, or optical properties, but also that many parts of this field are still not fully understood and need further investigation.

In this regard, we studied point defects in TMDCs like substitutional atoms or surface adatoms. Using *ab initio* calculations, we derive a multi-scale approach to describe the defect-induced potential with material-realistic models. Moreover, using those models we investigated the change of the defects properties in different dielectric environments to characterize the applicability of defects in the context of Coulomb engineering. We found significant changes

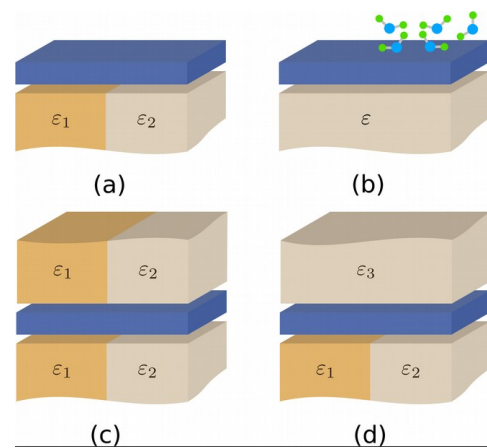


Figure 1: Sketches of a monolayer (blue) in different laterally structured environments

in ionization energies and the spatial extension of bound impurity states depending on external screening.

Besides the work on the semiconducting TMDCs, another part of this project was dedicated to the metallic representatives of this class of materials. Here, we focused on the description of many-body instabilities, particularly the formation of periodic lattice distortions that are driven by interaction processes involving the low-energy electrons. Again, our approach is based on minimal, yet material-realistic lattice models whose parameters are obtained from *ab initio* calculations, not only for the electronic but also for the lattice degrees of freedom. The latter constitute the computationally most expensive step of our scheme, where we greatly benefited from the facilities provided by HLRN.

Results

Material-realistic approach to Coulomb engineering

Substrates can significantly change the band gap of a material due to external screening of the Coulomb interaction. To find suitable materials for the creation of heterostructures, we had to investigate how strongly the band gap in different materials can be manipulated. Therefore we studied semiconducting TMDCs MX_2 with M being Mo or W and X being S or Se on different homogeneous substrates. We performed G0W0 *ab initio* calculations as implemented in VASP [4] of the freestanding monolayer and incorporated the dielectric environment through a G Δ W-like approach [5]. The substrate screening was taken into account via the WFCE [6] method for which we derived the needed Coulomb interaction terms of freestanding monolayers by means of RPA calculations from VASP calculations.

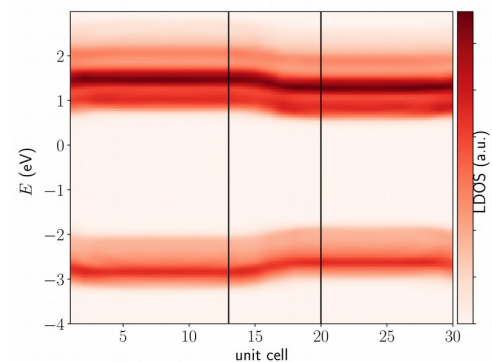


Figure 2: Local density of states of WS₂ on a laterally structured substrate with $\epsilon = 1$ in the left region and $\epsilon = 10$ in the right region.

We found significant band-gap reductions with increasing screening for all TMDCs. All materials show roughly the same reduction. For example, a SiO₂ substrate will reduce the band gap to about 87 % of the native band gap, irrespectively of the chosen 2D material, showing that all semiconducting TMDCs are equally applicable for Coulomb engineering.

Additionally, we investigated Coulomb-engineered heterostructures. The local density of states of WS₂ placed on a spatially structured substrate with $\epsilon = 1$ in the left region and $\epsilon = 10$ in the right region is shown in Fig. 2. The valence- and conduction-band edges are shown as darker red areas. The band-gap region is displayed in light red. We found a clear spatial band-gap modulation of a Type-I heterojunction with a length scale of the interface of around seven unit cells (marked with black lines). Thus, the interface region due to intrinsic limits is rather small, making extrinsic limitations such as the structured substrates more important for the application of Coulomb-engineered heterostructures.

Manipulation of defect potentials in 2D materials

Structural defects in solids can manifest in many different constellations and dimensionalities. As we are interested in electrical properties of TMDCs and their manipulation, we first considered a substitutional atom, which is a zero-dimensional point defect, for 2D materials. The model system we investigated was a MoS₂ monolayer with a Re atom substituting a Mo

atom. We used DFT calculations to extract the defect potentials by evaluating the orbitalprojected density of states. These potentials were fitted with a strictly 2D Keldysh-potential model [7]. To describe external screening, the model potential was modified to include the dielectric properties of the surrounding environment. The application of the effective-mass approximation in a 2D Schrodinger equation was used to calculate bound impurity states and ionization energies for different dielectric substrates.

Moreover, a more material-realistic “quasi 2D” (Q2D) model for the defect potential with a finite slab height was employed by using the already acquired model parameters. Analogous calculations were performed for the impurity levels, and the resulting ionization energies as a function of the substrate permittivity are illustrated for both applied models in Fig. 3. We found that, by introducing external screening, the ionization energies of the impurity can be reduced significantly by about 75 %. Additional calculations were carried out to analyze the defect potentials of Li adatoms on MoS2 monolayers, which are experimentally more easily controllable. The results gave a promising outlook on the application of flat-band engineering in the context of Coulomb engineering.

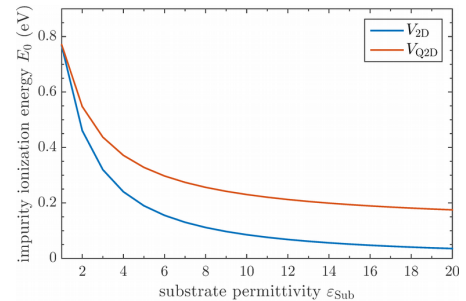


Figure 3: Ionization energy of the rhenium impurity depending on the dielectric environment.

Electronic structure of monolayer 1T – NbSe₂

In 2016, a single layer of 1T – NbSe₂ has been experimentally found to be an insulator [8], despite the fact that band theory predicts a metal. Using *ab initio* calculations we revealed the nature of this insulating state. Structural relaxation of a $\sqrt{13} \times \sqrt{13}$ supercell leads to a Star of David–shaped reconstruction with an energy gain of 60 meV per primitive unit cell. The band structure of this phase exhibits a half-filled flat band which is associated with orbitals that are delocalized over several atoms in each star. By including many-body corrections through a combined GW, hybrid-functional, and DMFT treatment, we found the flat band to split into narrow Hubbard bands.

Phase diagram of lattice instabilities in 1H-TaS₂

Depending on the experimental conditions, a monolayer of 1H-TaS₂ can feature charge-density waves of different periodicities [9] or no charge order at all [10]. To theoretically reproduce this complex phase diagram of lattice instabilities, we developed a scheme for the renormalization of phonons based on the downfolding method “constrained density-functional perturbation theory” (cDFPT) [11] using software such as QUANTUM ESPRESSO, Wannier90 and EPW. The resulting phase diagram is shown in Fig. 4 [9]. It qualitatively reproduces the experimental observations.

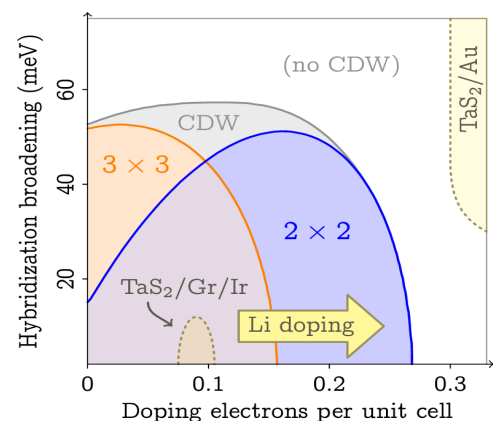


Figure 4: Phase diagram of lattice instabilities in 1H-TaS₂.

Fluctuation diagnostics of phonon anomalies

The origin of the charge-density waves in materials like 1H – TaS₂ has been controversial for more than four decades. The scheme we used to calculate the phase diagram in Fig. 4 can also be used to disentangle the underlying complex interplay of electron and phonons. Introducing the technique of “fluctuation diagnostics” [12] to the field of electron–phonon physics, we could unambiguously identify the relevant electronic degrees of freedom, see Fig.

5, and found that the lattice instabilities in $1H - TaS_2$ and similar metallic TMDCs are driven by the physics of massive Dirac fermions.

Publications

- J. Berges, E. G. C. P. van Loon, A. Schobert, M. Rösner, T. O. Wehling, *Ab-initio phonon self-energies and fluctuation diagnostics of phonon anomalies: lattice instabilities from Dirac pseudospin physics in transition-metal dichalcogenides*, arXiv:1911.02450 (2019)
- C. Steinke, M. Rosner, and T. O. Wehling, *Coulomb-Engineered Heterojunctions and Dynamical Screening in Transition Metal Dichalcogenide Monolayers*, arXiv:1912.10430 (2019)
- J. Hall, N. Ehlen, J. Berges, E. van Loon, C. van Efferen, C. Murray, M. Rosner, J. Li, B. V. Senkovskiy, M. Hell, M. Rolf, T. Heider, M. C. Asensio, J. Avila, L. Plucinski, T. Wehling, A. Gruneis, and T. Michely, *Environmental control of charge density wave order in monolayer $2H - TaS_2$* , ACS Nano **13**, 10210 (2019)
- P. Klement, C. Steinke, S. Chatterjee, T. Wehling, and M. Eickhoff, *Effects of the Fermi level energy on the adsorption of O_2 to monolayer MoS_2* , 2D Mater. **5**, 045025 (2018)
- E. Kamil, J. Berges, G. Schonhoff, M. Rosner, M. Schuler, G. Sangiovanni, and T. Wehling, *Electronic structure of single layer $1T - NbSe_2$: interplay of lattice distortions, non-local exchange and Mott–Hubbard correlations*, J. Phys. Condens. Matter **30**, 325601 (2018)

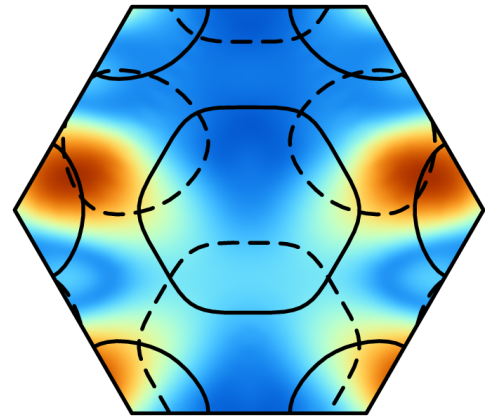


Figure 5: Momentum-dependent electron-phonon coupling and Fermi surface of $1H-TaS_2$ for the wave vector of the leading

References

- [1] M. Rosner *et al.*, Nano Lett. **16**, 2322 (2016)
- [2] A. Raja *et al.*, Nat. Comm. **8**, 15251 (2017)
- [3] Z. Lin *et al.*, 2D Mat. **3**, 022002 (2016)
- [4] G. Kresse and J. Hafner, J. Phys. Condens. Matter **6**, 8245 (1994)
- [5] M. Rohlifing, Phys. Rev. B **82**, 205127 (2010)
- [6] M. Rosner *et al.*, Phys. Rev. B. **92**, 085102 (2015)
- [7] L. V. Keldysh, JETP Lett. **29**, 658 (1979)
- [8] Y. Nakata *et al.*, NPG Asia Materials **8**, e321 (2016)
- [9] J. Hall *et al.*, ACS Nano **13**, 10210 (2019)
- [10] C. E. Sanders *et al.*, Phys. Rev. B **94**, 081404(R) (2016)
- [11] Y. Nomura *et al.*, Phys. Rev. B **92**, 245108 (2015)
- [12] O. Gunnarsson *et al.*, Phys. Rev. Lett. **114**, 236402 (2015)

6.26 *hbp00046*: Modelling strongly correlated electrons in presence of nonlocal interactions

| | |
|-------------------------|--|
| HLRN-Projektkenung: | hbp00046 |
| Laufzeit: | IV/17 – I/19 |
| Projektleiter: | Prof. Dr. Tim O. Wehling |
| Projektbearbeiter: | Edin Kapetanović, Malte Schüler |
| Institut / Einrichtung: | Institut für Theoretische Physik, Universität Bremen |

Overview

The competition of local and non-local Coulomb interactions plays an important role in the electronic structure of strongly correlated materials: Non-local interactions can effectively screen local interactions and weaken Mott Hubbard type electron correlations. They can furthermore push the electronic system into symmetry broken phases with e.g. charge order. While local and non-local Coulomb interactions naturally occur in any real material, low-energy models which describe correlated electron systems (e.g. the Hubbard model) quite often neglect non-local interactions completely. In this project, we currently focus specifically on a Hubbard model extended by the nonlocal exchange interaction which tends to push the system towards a ferromagnetic state. While said interactions are often neglected due to their typically small magnitude, we find that exchange interactions which are much weaker than the hopping are sufficient to change the properties of the system. This makes the widely used Hubbard approximation quite questionable. In order to study the influence of nonlocal exchange interactions, we introduce an effective Hubbard model with a renormalized on-site interaction and an effective magnetic field which accounts for possible ferromagnetic order.

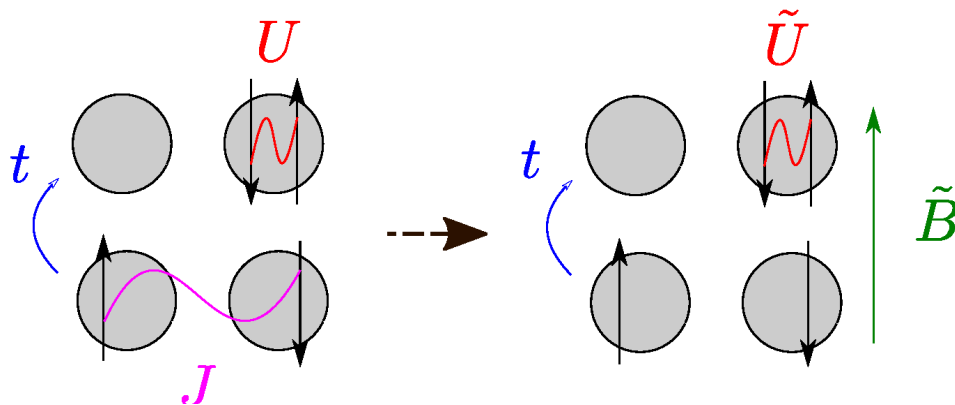


Figure 1: Original model (left) and the effective model (right) which is used as an approximation.

The parameters of the effective model (i.e. the local interaction the the effective, magnetic field) are chosen such that we minimize a free energy functional through the density operator. This involves solving the effective model, which we do with the Determinantal Quantum Monte Carlo (DQMC) method.

Results

We have performed DQMC calculations for a Hubbard model with an external magnetic field at half filling where the sign problem is absent. The geometries are chosen to be square lattices (with periodic boundary conditions) since Hubbard models on such lattices have been extensively studied, especially in the context of superconductivity. From different lattice sizes (i.e. 4x4, 6x6, 8x8, 10x10, 12x12), we extrapolated the relevant data for the $N \rightarrow \infty$ - case. When performing the calculation for each datapoint in the U-B-plane with one CPU, the parallelization becomes trivial. The temperature in the simulations was set to $\beta t = 10$, which corresponds to a regime where correlation effects are expected to be visible.

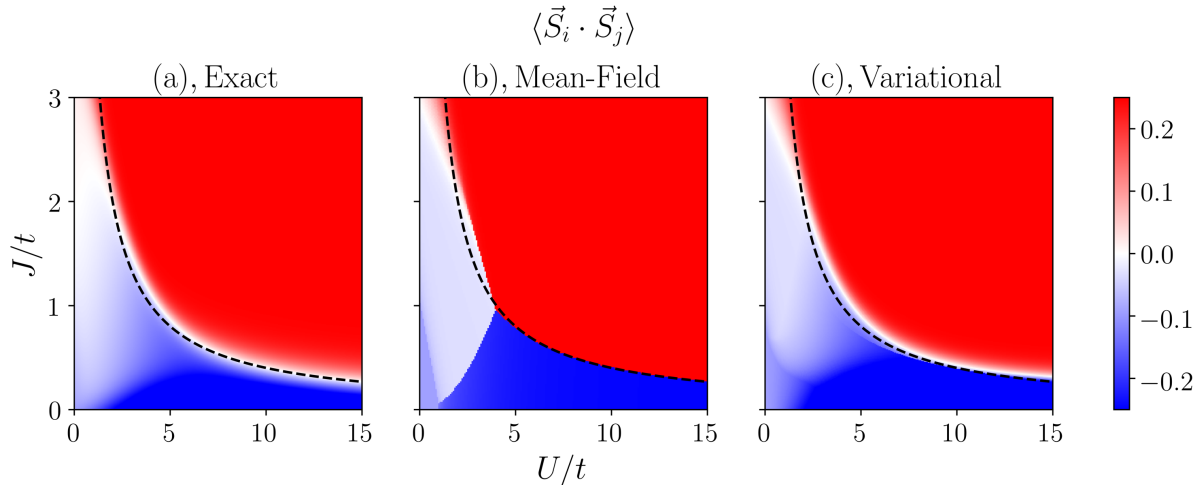


Figure 2: Benchmarking results: Spin-spin correlation between next neighbors on a 4-site model. The black, dashed $4t^2/U$ -line is where the transition is expected analytically for strong U. (a): Exact solution. (b): Static mean-field theory. (c): Our novel variational approach.

Figure 2 shows the spin-spin correlation between next neighbors for our variational method for a four-site cluster which can be solved exactly and thus serves as a benchmarking example. The static mean-field theory predicts discontinuous first-order phase transitions between para-, ferro- and antiferromagnetic phases while the behaviour should be completely smooth. The variational approach provides much better qualitative agreement with the exact solution.

Figure 3 shows the same spin-spin correlations for a half-filled square lattice. Static mean-field theory again predicts artificial first-order transitions while our method displays smooth behaviour. Extensive error analysis revealed that the visible steps in Figure 3b are numerical artifacts, and not weak first-order transitions (i.e. the behaviour is indeed completely smooth). This coincides with older results obtained within the Dynamical Mean Field Theory (DMFT) framework, which, however, is not very well suited for describing 2D-materials. Our results illustrate that the spatial correlations which are neglected within DMFT (and taken into account here) lead to quantitative differences only. In comparison to e.g. DMFT, our method is much better suited for tackling low-dimensional problems as it has no systematic error coupled to the system's dimension.

Our results are available as a preprint on: <https://arxiv.org/abs/1911.05420>. It is currently under consideration for publication in Physical Review B.

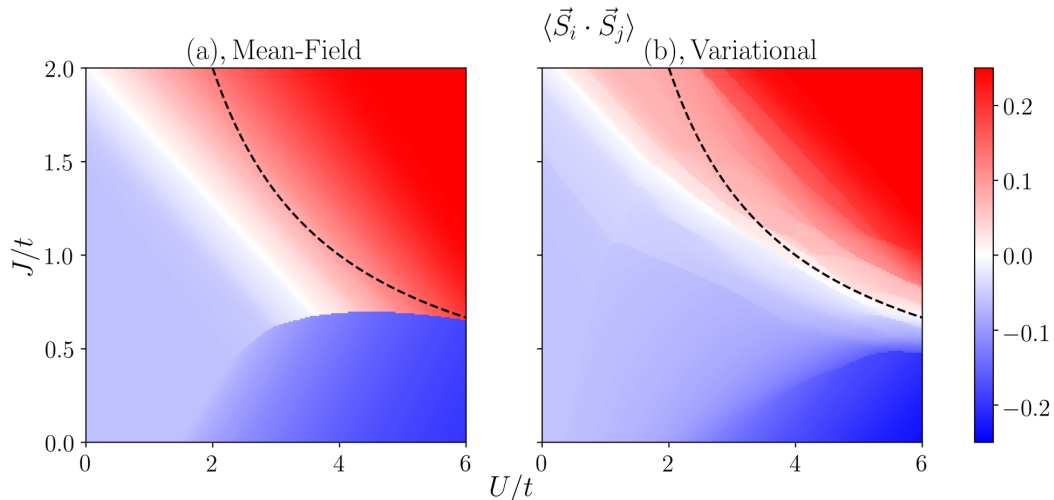


Figure 3: Spin-spin correlation between next neighbors on a half-filled square lattice. The black, dashed $4t^2/U$ -line is where the transition is expected analytically for strong U . (a): Static mean-field theory. (b): Variational approach.

Outlook

We developed a novel, variational method which is well suited for describing low-dimensional correlated systems. However, the numerical sign problem within DQMC effectively restricts us to half filling on bipartite lattices. In our current follow-up project, we intend to study the effects of nonlocal interactions in doped systems (especially in parameter regimes where High-Tc superconductivity occurs) by taking a detour over the Dynamical Cluster Approximation, where the sign problem is not as severe.

Presentations & Posters

- **Poster:** CECAM-Workshop "Correlated Electron Physics beyond the Hubbard Model", Feb 4th-8th 2019, Bremen
- **Poster:** International Summer School 'Nicolas Cabrera', Sep 08th-13th 2019, Madrid
- **Talk:** DPG-Frühjahrstagung der Sektion Kondensierte Materie, Mar 31th – Apr 05th 2019, Dresden
- **Poster:** CORPES19 'International Workshop on Strong Correlations and Angle-Resolved Photoemission Spectroscopy', Jul 12th-21th 2019

6.27 *hbp00047*: Coulomb engineering of Mott insulators

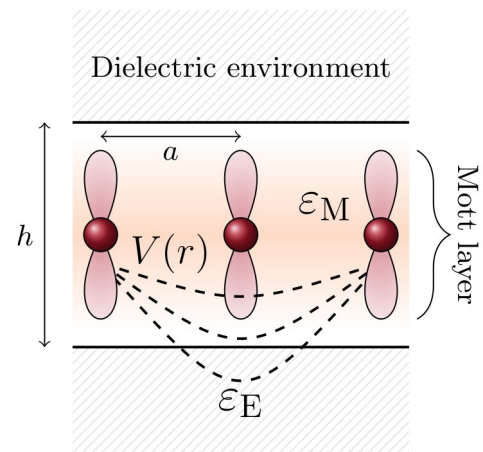
| | |
|--------------------|----------------------|
| HLRNProject ID: | hbp00047 |
| Run time: | I/2019 – IV/2020 |
| Project Leader: | Prof. Dr. Wehling |
| ProjectScientists: | Dr. E. van Loon |
| Affiliation: | University of Bremen |

Overview

Electrons are responsible for the charge transport in solids. A metal possesses free electrons and these allow current to flow. On the other hand, an insulator has a gapped spectrum, which means that there are no free charges and there is no charge transport. In Mott insulators, such a gap is caused by the Coulomb interaction between the (charged) electrons: due to their mutual repulsion, the electrons are no longer free to move through the material. In a vacuum, the strength of the Coulomb interaction depends only on the distance between the electrons in question. However, the electrons in real materials do not live in a vacuum and the Coulomb interaction is *screened* by other electrons in the material and its surroundings. In two-dimensional materials, the environment is especially important, since every part of the material is close to the environment.

This kind of environmental screening promises interesting consequences in Mott insulators. Since the strength of the Coulomb interaction determines if such a system is insulating or metallic and is determined itself by the dielectric environment, this way to manipulate materials is called *Coulomb engineering*. It is a way to change the properties of a material without touching the material itself, in other words, non-invasively.

Figure 1: Impression of a monolayer Mott insulator sandwiched by a dielectric environment. The Coulomb interaction between electrons in the monolayer depends on the screening inside the monolayer and also on the dielectric constant of the environment, since some field lines leave the material. In this way, the environment can be used to control the properties of the Mott insulator.



Results

To study this effect in detail, we looked at a thin layer of a Mott insulating material sandwiched in a dielectric environment, as illustrated in Fig. 1. The field lines that pass through the environment will feel the environmental dielectric constant instead of the one of the material and this changes the overall magnitude of the Coulomb interaction. It also determines how the interaction depends on the distance, since the amount of environmental screening depends on how many field lines go through the environment. Since the Coulomb interaction is responsible for many electronic properties and in particular for the Mott gap, in this situation the sandwich structure can be used to control these properties of the insulating monolayer: Coulomb engineering.

This scenario is hard to investigate theoretically and computationally, since there are two distinct physical length scales. Due to the strong Coulomb interaction, the electrons in Mott

insulators are *strongly correlated*. This means that the electrons cannot be treated as independent particles and makes the electronic system difficult to treat computationally. A common approach is to use a simplified model, the Hubbard model, where only the interaction between electrons on the same site is taken into account (short length scale). That simplified model is already extremely challenging to investigate numerically, but it is also clearly insufficient for this study since the spatial character (long length scale) of the environmental screening is essential. Instead, we use a realistic model of environmental screening in two-dimensional materials [1].

Solving this model requires us to use the Dual Boson method [2], a modern many-body technique that can simultaneously deal with the strong short-ranged correlations that make the system insulating and with the long-ranged, environmentally screened Coulomb interactions. With this method, we have determined how the electronic spectrum of the Mott insulator depends on the environment.

Physicists study correlated electron systems by determining their spectral function. This spectrum shows if there are electronic states in the system with a given energy E and momentum k . Experimentally, the momentum-resolved spectral function can be investigated with two complementary methods: angular resolved photo-emission spectroscopy (ARPES) and scanning tunneling spectroscopy (STS). Both experimental methods have limits, ARPES is restricted to the part of the spectrum below the Fermi energy and STS only shows the average of the spectral function over all momenta. From the theory side, the full spectral function is a natural output of the Dual Boson calculations.

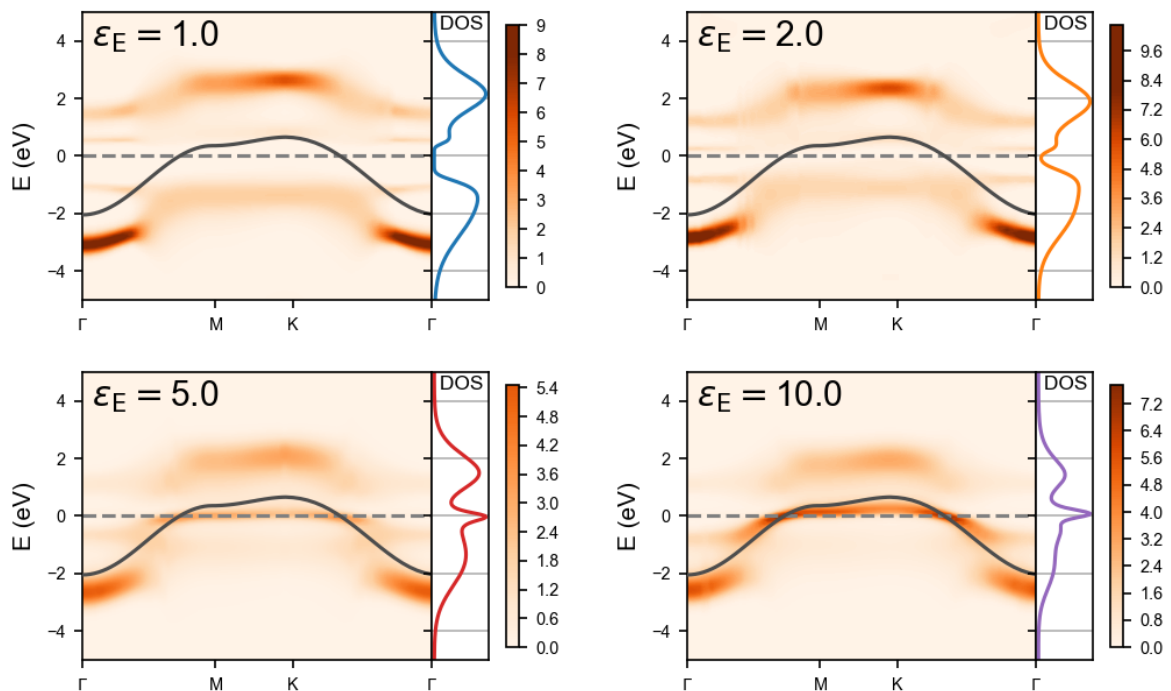


Figure 2: Evolution of the spectral function of a monolayer, as the environment changes from vacuum to an effective dielectric. The black curve is the non-interacting dispersion. To the right of every spectrum is the momentum average, as measurable in STS. The isolated monolayer is an insulator, with a gap in the spectrum around $E=0$. Due to the dielectric environment, it turns into a metal with finite spectral weight at $E=0$.

Fig. 2 shows how the calculated spectral function evolves from a monolayer surrounded by vacuum (dielectric constant=1) to an environmental dielectric constant of 10 (bulk Si corresponds to a dielectric constant of 12). The colored curve on the right of each graph shows the density of states, i.e., the momentum average of the spectral function that would be measured in STS experiments. The screening by the substrate leads to several substantial changes in the spectral function. Most dramatically, the system changes from an insulator to a metal: the gap at the Fermi level ($E=0$) disappears and a quasiparticle band emerges there. These low-energy particles will be able to conduct, so that that system is not insulating anymore. The appearance of the quasiparticle peak is clearly visible both in the spectral function and the local density of states. On top of this dramatic change at Fermi level, the features further away are also clearly changing due to the environmental screening, with spectral intensity moving towards the Fermi level.

Our results demonstrate that the dielectric environment can be used to control Mott insulating layered materials, reducing the size of their Mott gap and even turning them into metals. Changes in the Hubbard bands and the size of the gap on the eV-scale are possible and a sufficiently strong dielectric environment can turn a Mott insulator conducting.

Our work opens a perspective for the fabrication of heterostructures by the application of dielectric covering on parts of a Mott monolayer. In this way, conducting paths or quantum dots can be created in an otherwise insulating layer.

Outlook

So far, we have proven the principle of Coulomb engineering: the environmental dielectric constant can produce an insulator-metal transition. Now, we wish to predict which Mott materials are most suited to Coulomb engineering, investigating the role of the internal screening of the material itself and the thickness of the monolayer material. In addition to these material properties, the temperature is also expected to play an important role. We plan to investigate these aspects of Coulomb engineering in the near future.

References

- [1] M. Rösner, E. Şaşlıoğlu, C. Friedrich, S. Blügel, and T. O. Wehling, *Phys. Rev. B* **92**, 085102 (2015)
- [2] Erik G. C. P. van Loon, Alexander I. Lichtenstein, Mikhail I. Katsnelson, Olivier Parcollet, and Hartmut Hafermann, *Phys. Rev. B* **90**, 235135 (2014)

Presentations and Posters

1. E. van Loon, Talk at DPG (German Physical Society) Spring Meeting, Regensburg, April 4, 2019
2. E. van Loon, Talk at CORPES, International Workshop on Strong Correlations and Angle-Resolved Photoemission Spectroscopy, Oxford, July 18, 2019
3. E. van Loon, Poster presentation at *Korrelationstage*, Dresden, September 16, 2019
4. E. van Loon, Talk at ParisEdge2019, Cutting-edge topics in Quantum Materials, Paris, September 26, 2019
5. E. van Loon, Poster presentation at CECAM OUTBOX workshop, Bremen, October 7, 2019

6.28 *nak00001*: Seamless sea ice prediction with AWI Climate Model

HLRNProject ID: nak00001
 Run time: II/2019 – I/2020
 Project Leader: Dr. Helge Goessling
 Project Scientists: Dr. Longjiang Mu, Dr. Lars Nerger
 Affiliation: Alfred-Wegener-Institut Helmholtz Zentrum für Polar- und Meeresforschung, Bremerhaven

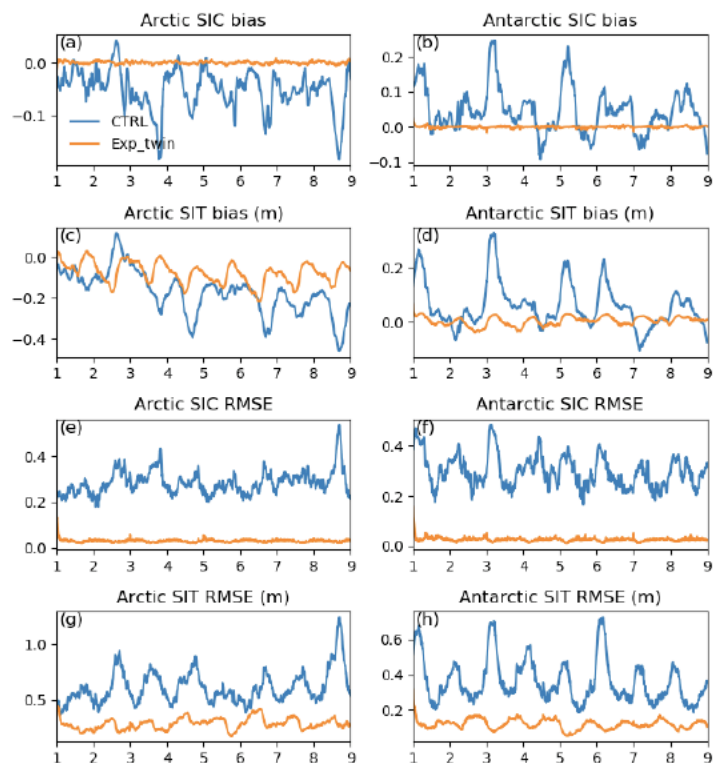
Overview

Advanced sea-ice prediction capacity is urgently needed to meet a growing socio-economic demand, driven in particular by an increasing accessibility of the Arctic in the course of climate change. The first version of the seamless sea ice prediction system is developed with computation resources support from HLRN. We implement sea ice concentration, sea ice thickness, sea ice drift, sea surface temperature and sea surface pressure assimilation in the coupled model. The robustness of this prediction system is confirmed by perfect model experiment. From October 2010 to December 2018, nearly 9 years' analysis is evaluated by independent observations in our paper published on Journal of Advances in Modeling Earth Systems.

Results

The perfect model experiment is conducted firstly by assimilating sea ice concentration data into the system with sea ice thickness also updated in the state vector to test if there are systematic errors during the analysis step or technical bugs hidden behind. The daily synthetic sea ice concentration constructed from model simulations are assimilated back into the system but over a different time period by which a different climate is guaranteed. With such strong

Figure 1: Bias (a,b,c,d) and RMSE (e,f,g,h) of sea ice concentration (SIC) and sea ice thickness (SIT) in the Arctic (left column) and the Antarctic (right column) for CTRL (blue) and the perfect model experiment (orange). The unit for SIT is meter. SIC ranges from 0 to 1. X-axis represents years from the start.



assimilation frequency, the system will exhibit strong drift in the thickness analysis over time if the assimilation concept goes wrong. An 8-year experiment (Fig. 1) shows that such drift in sea ice thickness analysis is not found in our system, which indicates the system works properly.

We then conduct real data assimilation with sea ice (sea ice concentration, sea ice thickness, sea ice drift) and ocean (sea surface temperature) assimilation in the coupled model. The analysis is compared with independent data. Results show that the assimilation has improved the variables with observations as expected. For sea ice thickness, the model has reproduced better estimates than the experiment without any data assimilation. It is worthy to note that the assimilation of sea surface temperature in the climate model brings the surface information deep into around 250m. The ocean mean salinity is also slightly improved. The errors of 2m atmosphere temperature and 10 m wind fields are also significantly reduced particularly in the Arctic ocean, where we found that the improved surface pressure system drives even more realistic ocean circulation in the intermediate layer (Fig. 2).

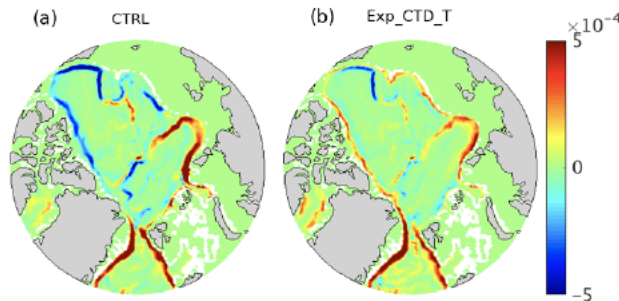


Figure 2: Topography integrated vertically from 230m to 3150m for CTRL (a) and Exp_CTD_T (b) averaged over 2014-2018. A positive topography corresponds to flow that has deep water to the left on the northern hemisphere, thus representing a counterclockwise flow along the boundary in the Arctic Ocean. Note that Exp_CTD_T assimilates sea ice concentration, sea ice thickness, sea ice drift and sea surface temperature.

An experiment with sea ice drift assimilation suggests that the sea ice thickness field in the Antarctic is dramatically improved (Fig. 3). We found that the covariance between sea ice thickness and drift has magnitudes similar to those between sea ice thickness and concentration. But when considering the innovation and observation errors, the weight given to the SID assimilation is about 3 times larger than that given to the SIC assimilation, which thus reduces the systematic errors due to the assimilation of sea ice concentration.

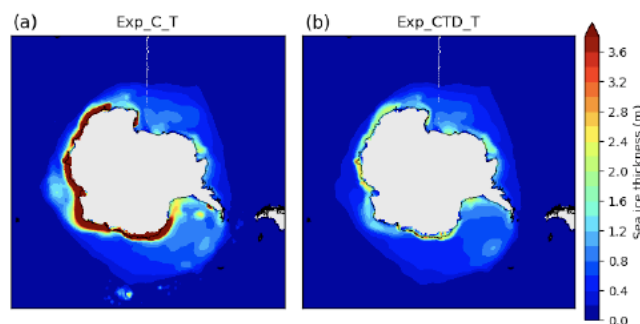


Figure 3: Antarctic sea ice thickness (SIT) averaged over 2007-2012 for Exp_C_T (a) and Exp_CTD_T (b). Note that Exp_CTD_T assimilates sea ice concentration, Arctic sea ice thickness, sea ice drift and sea surface temperature. Exp_C_T assimilates only sea ice concentration and sea surface temperature. Also note that sea ice thickness observations are now not available in the Antarctic.

Currently we have not implemented the assimilation with PDAF also in the atmosphere model, but use a simple nudging method, it is still possible for us to test possible impacts when taking atmosphere observations into account. To explore this, we conducted a one-year experiment with sea surface pressure data from the ERA Interim reanalysis nudged into the system. The atmosphere is constrained as expected. However, the reduce ensemble spread in the system has deteriorated the performance of other variables. It thus calls for further delicate tuning when getting atmosphere data also into the system.

Outlook

Recently, a new coupled model AWI-CM3.0 was developed at AWI. This model consists of ocean component FESOM2.0 and atmosphere component OpenIFS. A published paper documented that FESOM2.0 has nearly 5 times faster than FESOM1.4. OpenIFS is also well known for its faster integration than ECHAM at the same resolution due to its semi-Lagrangian advection scheme. A general test with AWI-3.0 with the same resolution both for ocean and atmosphere suggests that it costs even less computation resources, and at the same time, 2 times faster than AWI-CM1.0. We will further implement all our codes into the AWI-CM3.0 in the next step, and conduct data assimilation with even higher ensemble size and tackle the real seasonal predictions.

Publications

1. Mu, L., Nerger, L., Tang, Q., Losa, S.N., Sidorenko, D., Wang, Q., Semmler, T., Zampieri, L., Losch, M. and Goessling, H.F., *Towards a data assimilation system for seamless sea ice prediction based on the AWI Climate Model*. Journal of Advances in Modeling Earth Systems, p.e2019MS001937, <https://doi.org/10.1029/2019MS001937>
2. Nerger, L., Tang, Q., and Mu, L.: *Efficient ensemble data assimilation for coupled models with the Parallel Data Assimilation Framework: Example of AWI-CM*, Geosci. Model Dev. Discuss., <https://doi.org/10.5194/gmd-2019-167>, in review, 2019.

Presentations

1. Mu, L., Nerger, L., Tang, Q., Losa, S.N., Sidorenko, D., Wang, Q., Semmler, T., Zampieri, L., Losch, M. and Goessling, H.F., *Sea ice data assimilation in a seamless global coupled sea-ice prediction system*, *9th International Workshop on Sea Ice Modelling, Data Assimilation and Verification*, June 18, 2019, Bremen, Germany. (Oral)